An Adaptive Well-Balanced Positivity Preserving Central-Upwind Scheme for the Shallow Water Equations over Quadtree Grids

by

Seyed Mohammad Ali Ghazizadeh Fard

Thesis submitted to the University of Ottawa
in partial Fulfillment of the requirements for the
Doctorate of Philosophy in
Civil Engineering

Department of Civil Engineering
Faculty of Engineering
University of Ottawa

Abstract

Shallow water equations are widely used to model water flows in the field of hydrodynamics and civil engineering. They are complex, and except for some simplified cases, no analytical solution exists for them. Therefore, the partial differential equations of the shallow water system have been the subject of various numerical analyses and studies in past decades. In this study, we construct a stable and robust finite volume scheme for the shallow water equations over quadtree grids. Quadtree grids are two-dimensional semi-structured Cartesian grids that have different applications in several fields of engineering, such as computational fluid dynamics. Quadtree grids refine or coarsen where it is required in the computational domain, which gives the advantage of reducing the computational cost in some problems.

Numerical schemes on quadtree grids have different properties. An accurate and robust numerical scheme is able to provide a balance between the flux and source terms, preserve the positivity of the water height and water surface, and is capable of regenerating the grid with respect to different conditions of the problem and computed solution. The proposed scheme uses a piecewise constant approximation and employs a high-order Runge-Kutta method to be able to make the solution high-order in space and time. Hence, in this thesis, we develop an adaptive well-balanced positivity preserving scheme for the shallow water system over quadtree grids utilizing different techniques. We demonstrate the formulations of the proposed scheme over one of the different configurations of quadtree cells. Six numerical benchmark tests confirm the ability of the scheme to accurately solve the problems and to capture small perturbations.

Furthermore, we extend the proposed scheme to the coupled variable density shallow water flows and establish an extended method where we focus on eliminating nonphysical oscillations, as well as well-balanced, positivity preserving, and adaptivity properties of the scheme. Four different numerical benchmark tests show that the proposed extension of the scheme is accurate, stable, and robust.

Acknowledgements

I would first like to express my deepest gratitude to Professor Abdolmajid Mohammadian for the opportunities that he provided and his supervision during the course of the program.

I would like to thank Professor Alexander Kurganov for assisting me during my studies and his contribution towards this work.

I would like to thank Professor Philippe LeFloch for giving me the opportunity to work under his supervision; and the Marie Skłodowska-Curie Fellowship grant at the Laboratoire Jacques Louis Lions of Sorbonne University. I am also grateful to have worked with Dr. Yangyang Cao during this opportunity which extended my understanding of numerical analysis of PDEs and well-balanced schemes.

I would like to thank my family (Mom, Dad, Marzieh, and Marjan) who have always supported me throughout my PhD. And finally, I would like to thank my friends (John L., Sean, Liz, Gayle, John M., Yosha, Amin, Saeedeh, Yarzar, Ludovic, Matthew, Vincent, Pierre, Larry, Ata, Mostafa, and Tom) for their support and help to keep me motivated and sane during difficult and challenging times. Thank you for being there for me; I love you all.

Contents

List of figures

List of tables

List of acronyms

1-D One-Dimensional viii, 8, 9
2-D Two-Dimensional 7, 16, 18, 53, 103

CFD Computational Fluid Dynamic 11, 16
CFL Courant-Friedrichs-Lewy 34, 71

FVEG Finite Volume Evolution Galerkin 9

HLLC Harten-Lax-van Leer Contact wave 54

ID Identification Number 12

ODE Ordinary Differential Equations 9, 10, 21, 22, 35, 57, 71

PDE Partial Differential Equations 1, 7

RHS Right Hand Side 30–33, 64, 66

SSP Strong Stability Preserving 10, 35, 71
SWE Shallow Water Equations 1–3, 7–9, 11, 14, 15, 17, 18, 21, 53, 54

List of symbols

Greek Letter Symbols

$\Delta x_{j,k}$	Cell length in the x-direction
$\Delta y_{j,k}$	Cell length in the y-direction
ρ	Density of the mixture
$\rho_\circ$	Reference density

Roman Numerals

$\left(\overline{\boldsymbol{U}}_{j,k}^{n+1}\right)_{\text{new}}$	New conservative variables values at t^{n+1}
$\left(\overline{\boldsymbol{U}}_{j,k}^{n+1}\right)_{\text{old}}$	Old conservative variables values at t^{n+1}
$\boldsymbol{F}$	Flux vector in the x-direction
$\boldsymbol{G}$	Flux vector in the y-direction
$\boldsymbol{H}^x$	Numerical flux in the x-direction
$\boldsymbol{H}^y$	Numerical flux in the y-direction
$\boldsymbol{S}$	Source term vector
$\boldsymbol{U}$	Conservative variables vector
$\boldsymbol{U}$	New vector to solve variable density SWEs
$\boldsymbol{U}_{\alpha,\beta}^{\pm}$	right/left point values
$\boldsymbol{U}_{\gamma,\delta}^{\pm}$	top/bottom point values

$\boldsymbol{U}_x$	Slope of conservative variables vector in the x-direction
$\boldsymbol{U}_y$	Slope of conservative variables vector in the y-direction
ℓ	Level of quadtree grid
$\widetilde{B}$	Piecewise bilinear reconstruction of bottom topography
$\widetilde{\boldsymbol{U}}$	Piecewise polynomial interpolation of conservative variables vector
$\overline{\boldsymbol{S}}$	Average of the source term over a cell vector
$\overline{\boldsymbol{U}}$	Average of conservative variables over a cell vector
$\{C_{j,k}^{\text{new}}\}$	Set of seeding points for t^{n+2}
$\{C_{j,k}^{\text{old}}\}$	Set of points at t^{n+1}
$a_{\alpha,\beta}^{\pm}$	Speed of propagation in the x-directions
B	Bottom topogrophy
$b_{\gamma,\delta}^{\pm}$	Speed of propagation in the y-directions
C	Quadtree cell
$C_{\rho,\,\text{seed}}$	Minimum density slope for seeding points
C_{seed}	Minimum slope for seeding points
$C_{w,\,\text{seed}}$	Minimum water surface slope for seeding points
g	Gravitational constant
h	Water depth
$h\rho$	Conservative variable
hu	Unit discharge
hv	Unit discharge
m	Level of refinment
t	Time
u	Velocity in the x-direction
v	Velocity in the y-direction

w	Water surface
x	x-direction in the 2-D Cartesian system
y	y-direction in the 2-D Cartesian system
$\mathscr{C}^{(\ell)}$	Set of cells of different sizes in quadtree

Chapter 1

Introduction

Modelling and simulation are major areas of interest in the field of hydrodynamics, oceanography, and atmospheric sciences. Mathematical models can represent different phenomena in hydrodynamics. The Saint Venant system or the *shallow water equations* (SWE) are one of the most important classical models that describe and predict water flows in lakes, rivers, coastal areas, reservoirs, and also hazardous phenomena such as tsunamis (see Chapter 3). The SWE are utilized in flood prediction as well as hydraulic and civil engineering to be able to design, develop, and protect harbour, urban, and coastal areas.

The shallow water equations are *partial differential equations* (PDE) and form a nonlinear hyperbolic system of conservation laws. This system admits complex and non-smooth solutions that may contain shocks and rarefaction waves. The system can also admit contact discontinuity when the bottom topography is discontinuous. The SWE have to be solved numerically since there is no analytical solution available (except for very simple initial data, boundary conditions, and geometries) [42]. Therefore, designing a proper method is an important task to achieve an accurate and stable solution.

Many research works have been conducted on efficient solutions of homogeneous and non-homogeneous systems of conservation laws. The main focus of these works are developing schemes to capture shock waves in gases (e.g., the Burgers, and Euler equations) or hydraulic jumps in shallow flows (e.g., the shallow water equations). One of the most popular schemes are called Godunov-type *upwind* finite volume schemes in which Riemann problems are solved at cell interfaces [89]. Exact and

approximate Riemann solvers for shallow water flows are given in [23]. Note that the exact solutions of the Riemann problem are more expensive than the approximate ones. For more complex shallow water flows, the use of nonlinear Riemann solvers is recommended; e.g., Roe's Riemann solver in [76]

The upwind schemes are able to address propagation information along the characteristic surfaces. The original Godunov scheme is the first upwind scheme which approximates the solution using a piecewise constant function [29]. One of the drawbacks of the Godunov-type schemes is that they are complicated and can be computationally expensive. To address these issues, Riemann-problem-solver-free *central* schemes such as Lax–Friedrichs scheme can be utilized [25, 51]. A disadvantage of central schemes is their numerical dissipation that can be lessened by considering the local speeds of propagation, which results in another class of numerical schemes called *central-upwind* [45, 48].

Since the shallow water system is a system of conservation laws, the balance between the flux and source terms must be considered (i.e., the numerical method should be able to exactly preserve the initial data for steady state solutions). Such numerical methods are called *well-balanced*. The difference between well-balanced and non-well-balanced schemes can be seen for constant initial data with a nonflat bottom topography for a steady state solution; nonphysical oscillations come up which do not represent this steady state solution. Another example is in small perturbations of steady state solutions. The truncation error magnitude of the non-well-balanced scheme may become larger than the magnitude of perturbations waves [42, 46].

Another important property of stable and accurate numerical schemes is called *positivity preserving*, meaning that the scheme guarantees the positivity of computed primitive scalar variables, such as the water depth in the shallow water flows, or the density in the Euler's equations.

Numerous finite volume methods have been developed to solve the Saint Venant system. In Chapter 2, we present a review of schemes with different properties on the SWE such as well-balanced and positivity preserving properties as well as accuracy and adaptivity of numerical schemes.

1.1 Objectives

The primary objective of this thesis is to construct a central-upwind scheme to solve the shallow water equations. The proposed method is adaptive based on quadtree grids, well-balanced, capable of preserving positivity of the water depth and water surface, and is able to solve the system on irregular bottom topography. To achieve this goal the following procedure applies to construct the scheme:

- Generating a non-regularized quadtree grid with regards to the initial data and boundary conditions of the problem.
- Regularizing the non-regularized quadtree grid.
- Constructing the point values of the bottom topography and conservative quantities using piecewise polynomial reconstructions.
- Constructing the local speeds of propagation and central-upwind numerical fluxes in different cell configuration in quadtree grids.
- Constructing the conditions that preserve positivity of the water depth and the water surface.
- Constructing the well-balanced discretization of the source terms.
- Constructing the local gradients to be able to generate the quadtree for the next timestep.
- Constructing the velocities and water surface values that will be used in a new quadtree grid for the next timestep.

The above-mentioned numerical analysis steps are implemented on `C++` programming language to be able to analyse the scheme. It should be mentioned that the current source code of the scheme contains more than 6000 lines. Pursuing the main objective of this thesis, the proposed scheme is extended to the coupled variable density SWE. Furthermore, in the main objectives, we study the scheme:

- To validate the numerical model and investigate the accuracy, performance, and robustness using benchmark tests for shallow water flows.

– To verify the numerical scheme for the variable density shallow water flows to analyse the scheme using benchmark tests under constant-density and variable density conditions.

1.2 Contributions and novelty

We would like to first emphasize that the proposed scheme is the first of its kind to use a central-upwind method over quadtree grids. This thesis focuses on the performance of the proposed scheme by testing it on different benchmarks based on the objectives of this study. The proposed scheme is able to reduce computational cost in some problems (i.e, quadtree grids have fewer computational cells in comparison to ones in corresponding Cartesian or unstructured grids). In addition, the well-balanced property eliminates nonphysical oscillations; thus it is more accurate and efficient in comparison to non-well-balanced ones as well. Furthermore, the scheme is capable of eliminating the nonphysical oscillations caused by the density equation as well as reconstruction of the bottom topography over quadtree grids. The reconstruction of the bottom topography makes the scheme capable of solving problems with discontinuous bottom topography. Finally, we emphasize that the proposed scheme is positivity preserving where the scalar variables always remain positive.

The shallow water and variable density models offers a way to perceive the physical behavior of shallow water flows. The proposed scheme could eventually be used in different areas of hydrodynamics to be able to help engineers to study, model, and simulate various problems such as debris flows.

1.3 Thesis organization

The thesis is based on two technical papers and is divided into a literature review chapter and two paper-based chapters:

Chapter 3. An adaptive well-balanced positivity preserving central-upwind scheme on quadtree grids for shallow water equations

We present an adaptive well-balanced positivity preserving central-upwind scheme on quadtree grids for shallow water equations. The use of quadtree grids results in a robust, efficient and highly accurate numerical method. The quadtree model is developed based on the well-balanced positivity preserving central-upwind scheme proposed in [A. Kurganov and G. Petrova, *Commun. Math. Sci.*, 5 (2007), pp. 133–160, 46]. The designed scheme is well-balanced in the sense that it is capable of exactly preserving "lake-at-rest" steady states. In order to achieve this as well as to preserve positivity of water depth, a continuous piecewise bilinear interpolation of the bottom topography function is utilized. This makes the proposed scheme capable of modelling flows over discontinuous bottom topography. Local gradients are examined to determine new seeding points in grid refinement for the next timestep. Numerical examples demonstrate the promising performance of the central-upwind quadtree scheme.

Chapter 4. An adaptive well-balanced positivity preserving central-upwind scheme on quadtree grids for variable density shallow water equations

Minimizing computational cost is one of the major challenges in the modelling and numerical analysis of hydrodynamics. The use of quadtree grids results in a robust, efficient and highly accurate numerical method as well as lower computational cost. In this paper, we present an adaptive well-balanced positivity preserving scheme on quadtree grids for variable density shallow water equations. The scheme for the coupled system is developed based on the well-balanced positivity preserving central-upwind scheme proposed in [28]. The scheme is capable of exactly preserving "lake-at-rest" steady states; this is called the "well-balanced" property. A continuous piecewise bi-linear interpolation of the bottom topography function is utilized to achieve higher-orders in space and to preserve the positivity of water depth. Necessary conditions are checked to be able to preserve positivity of water

depth and density, and to ensure the achievement of a stable numerical scheme. At each timestep, local gradients are examined to find new seeding points in quadtree grid generation. Numerical examples demonstrate the promising performance of the proposed quadtree scheme.

1.4 Publications

1. **M. A. Ghazizadeh**, A. Mohammadian, and A. Kurganov. An adaptive well-balanced positivity preserving central-upwind scheme on quadtree grids for shallow water equations, *Computers & Fluids*, under revision, 2020.

2. **M. A. Ghazizadeh** and A. Mohammadian. An adaptive well-balanced positivity preserving central-upwind scheme on quadtree grids for variable density shallow water equations. *Numerische Mathematik*, under review, 2020.

Chapter 2

Literature review

2.1 The shallow water equations

The shallow water equations are derived from the *Navier-Stokes* equations with the assumption that the ratio of the vertical length to the horizontal length is small. The shallow water system describes the evolution of a hydrostatic homogeneous (with constant density), incompressible, and inviscid flow. The SWE are widely used in different scientific fields such as oceanography, hydrodynamics, civil engineering, risk assessment, etc.

The shallow water equations are PDE of conservation laws. The 2-D shallow water equations with the bottom topography source terms in the matrix form, read [43]

$$\boldsymbol{U}_t + \boldsymbol{F}(\boldsymbol{U}, B)_x + \boldsymbol{G}(\boldsymbol{U}, B)_y = \boldsymbol{S}(\boldsymbol{U}, B), \tag{2.1.1}$$

where conservative quantities, water surface (w) and the unit discharges (hu and hv) are

$$\boldsymbol{U} := (w, hu, hv)^\top,$$

and the fluxes and source term are:

$$\boldsymbol{F}(\boldsymbol{U}, B) = \left(hu, \frac{(hu)^2}{w-B} + \frac{g}{2}(w-B)^2, \frac{(hu)(hv)}{w-B}\right)^\top, \tag{2.1.2}$$

$$\boldsymbol{G}(\boldsymbol{U}, B) = \left(hv, \frac{(hu)(hv)}{w-B}, \frac{(hv)^2}{w-B} + \frac{g}{2}(w-B)^2\right)^\top, \tag{2.1.3}$$

$$\boldsymbol{S}(\boldsymbol{U}, B) = (0, -g(w-B)B_x, -g(w-B)B_y)^\top, \tag{2.1.4}$$

where t is time, g is the gravitational constant $u(x, y, t)$ and $v(x, y, t)$ are the water velocities in the x- and y-directions, respectively, $B(x, y)$ is the bottom topography, and $h(x, y, t)$ is the water depth. In Figure 2.1, an example of one-dimensional (1-D) shallow water flows is shown.

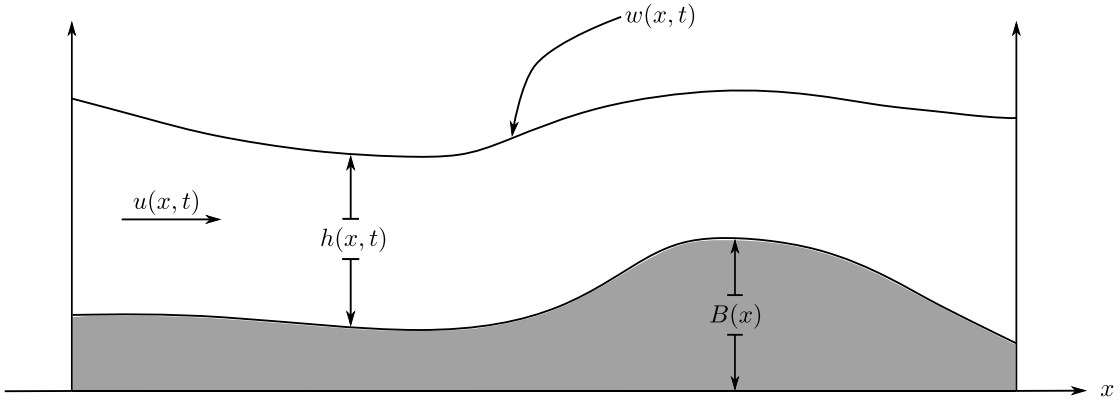

Figure 2.1: Example of 1-D shallow water flows over irregular bottom topography.

The proposed scheme has different properties such as, well-balanced, positivity preserving, adaptivity, and is implemented on quadtree grids. In what follows, a review of these properties is presented.

2.2 Well-balanced property

In well-balanced schemes on conservation laws, the flux gradients are exactly balanced by source terms. Different techniques have been introduced in order to add the well-balanced property. In [55], as one of the first well-balanced schemes for the SWE, a well-balanced wave propagation method over an arbitrary bottom topography is conducted by the use of a Riemann problem. In [39], a well-balanced numerical method to solve the steady state solution was presented, where the cell interface values were used. The scheme applies to Godunov or Roe-type upwind methods but no change is needed on the Riemann solver. In addition, [43] presents one- and two-dimensional well-balanced central-upwind methods for the shallow water equations with the source terms. This scheme is robust, capable of capturing

small perturbations, and a *black-box* solver for systems of nonlinear hyperbolic *ordinary differential equations* (ODE).

A generalization of the hydrostatic reconstruction technique in [3] for the shallow water system was introduced in [18]. The main goal of this study was to compare the well-balanced scheme to the scheme in [68]. Furthermore, an approximate Riemann problem solver SWE scheme in a one-dimensional framework using topography approximation by a piecewise function based on [34], which is an exact Riemann problem scheme, was constructed in [27]. In [56], the generalized Riemann problem (see [6]) of the SWE with bottom topography was extended. The use of the midpoint values at each cell interface helps the bottom topography effect to be included in numerical fluxes. The source term is discretized with an interface method, which makes the scheme well-balanced. More well-balanced schemes have been constructed recently, such as the schemes in [67, 78].

2.3 Positivity preserving property

Positivity preserving is the ability of the scheme to maintain positivity (or non-negativity) of scalar variables in different solutions of systems of conservation laws. In the case of the shallow water flows, a positivity preserving scheme should be able to compute and maintain the solution in the computational domain where water depth is zero (dry) or very small (almost dry). In addition, for the coupled variable density SWE, the scheme has to be capable of preserving positivity of the density.

Several positivity preserving methods for the SWE have been proposed. For example, in [3] a general well-balanced technique for any homogeneous problem solver based on a local primitive variables reconstruction is considered. This scheme is first- and second-order and satisfies the positivity condition of the water depth, and maintain a semi-discrete entropy inequality. A 1-D well-balanced and positivity preserving scheme for the SWE with a special reconstruction of the flow variables in wet–dry location was constructed [11]. In addition, in [12], a well-balanced Finite Volume Evolution Galerkin (FVEG) scheme based on [64] was presented, which is positivity preserving by limiting fluxes, where non-negativity happens, and able to manage dry boundaries.

Central-upwind methods have been popular in the past couple of decades. A

second-order well-balanced positivity preserving central-upwind method was conducted in [15]. A similar positivity preserving scheme with a new piecewise linear approximation of the bottom topography and a reconstruction with no oscillations was introduced in [5]. For further studies, we refer the reader to [26, 62, 85].

2.4 Accuracy

In order to increase the accuracy of the scheme, one can use a very fine computational grid; however, this increases the computational cost, which is a disadvantage for both the Godunov and Lax–Friedrichs schemes. These schemes are first-order accurate. Sharp approximated solutions can be achieved using high-order finite volume schemes [42]. One of the most popular high-order schemes are second-order schemes. The piecewise constant approximation requires replacement with a piecewise polynomial one to be able to develop a spatially second-order scheme. This makes the solution more accurate but also more complex and sometimes adds nonphysical oscillations [91]. In order to eliminate the nonphysical oscillations one should utilize *nonlinear limiters* (see e.g. [7, 9, 21, 36, 50, 60, 88] for the limiters that can be used in the second-order spatial reconstructions).

The shallow water system is an ODE system. The proposed scheme needs an appropriate ODE solver. *Runge-Kutta* methods are one of the best ODE solvers. We specifically focus on a three-stage third-order SSP Runge–Kutta method in our proposed scheme as follows [86, 87]:

$$\begin{aligned}
\boldsymbol{U}^{(1)} &= \boldsymbol{U}^n + \Delta t \boldsymbol{F}\left(\boldsymbol{U}^n, B\right) + \Delta t \boldsymbol{G}\left(\boldsymbol{U}^n, B\right), \\
\boldsymbol{U}^{(2)} &= \frac{3}{4}\boldsymbol{U}^n + \frac{1}{4}\Big[\boldsymbol{U}^{(1)} + \Delta t \boldsymbol{F}\left(\boldsymbol{U}^{(1)}, B\right) + \Delta t \boldsymbol{G}\left(\boldsymbol{U}^{(1)}, B\right)\Big], \\
\boldsymbol{U}^{n+1} &= \frac{1}{3}\boldsymbol{U}^n + \frac{2}{3}\Big[\boldsymbol{U}^{(2)} + \Delta t \boldsymbol{F}\left(\boldsymbol{U}^{(2)}, B\right) + \Delta t \boldsymbol{G}\left(\boldsymbol{U}^{(2)}, B\right)\Big],
\end{aligned} \tag{2.4.1}$$

where Δt is the timestep, and n is the timestep indicator. The proposed scheme is explicit. Note that, a potentially inefficient way of increasing the accuracy of any numerical scheme is refining its computational grid. This technique, however, exponentially increases the computational cost. Thus, quadtree grids become important.

2.5 Quadtree grids and adaptivity

Different types of computational grids are utilized in numerical analysis and modelling. The most common grids are structured, specifically Cartesian grids (see [61] for an example of SWE schemes on structured non-Cartesian grids). Cartesian grids are structured and simple. In finite volume, Cartesian grids keep equations and numerical models simple. Several studies have been conducted on the SWE on Cartesian grids such as, [19, 43, 46, 38, 50, 55]. Cartesian grids are not able to adequately capture complex boundaries in finite volume methods. This may lead to inaccurate and oscillatory schemes. This is where unstructured grids (especially triangular girds) show their advantage compared to Cartesian grids.

Unstructured grids are extensively used in hydrodynamics and civil engineering. Unstructured grids make formulation of numerical schemes more complicated; however, they sufficiently represent boundaries of complex geometries. Some examples of SWE methods on unstructured grids are given in [3, 4, 15, 16, 37, 63].

Hierarchical data structures such as quadtree are extensively utilized techniques in the fields of computer science, e.g., image processing, computer graphics, computational geometry, robotics, video games, and *computational fluid dynamics* (CFD). In quadtree, each *node* has exactly four *children*. The tree starts with the first *level* on the *root* as a *parent* with four children. Each child can have four children as a parent on the next level. This algorithm *recurses* until the tree reaches the maximum level of quadtree. Nodes that have no children are called *leaf* nodes. Figure 2.2 demonstrates an example of quadtree data structure.

Quadtree grids imply recursive spatial decomposition on the domain of the problem. In many CFD problems, a square quadtree can be used instead of unstructured mesh generation technique; as its characteristics make the solution easier. Figure 2.2 also shows the maximum number of cells that each node in that level can have. Note that we choose the maximum level of quadtree refinement (m) based on the accuracy that we are looking for. Increasing m leads to higher accuracy but it increases the computational cost. In addition, we recommend using higher values of m where the problem leads to higher values of propagation speed. This helps to properly capture hydraulic jumps. Furthermore, we recommend a grid refinement where the boundaries are complex.

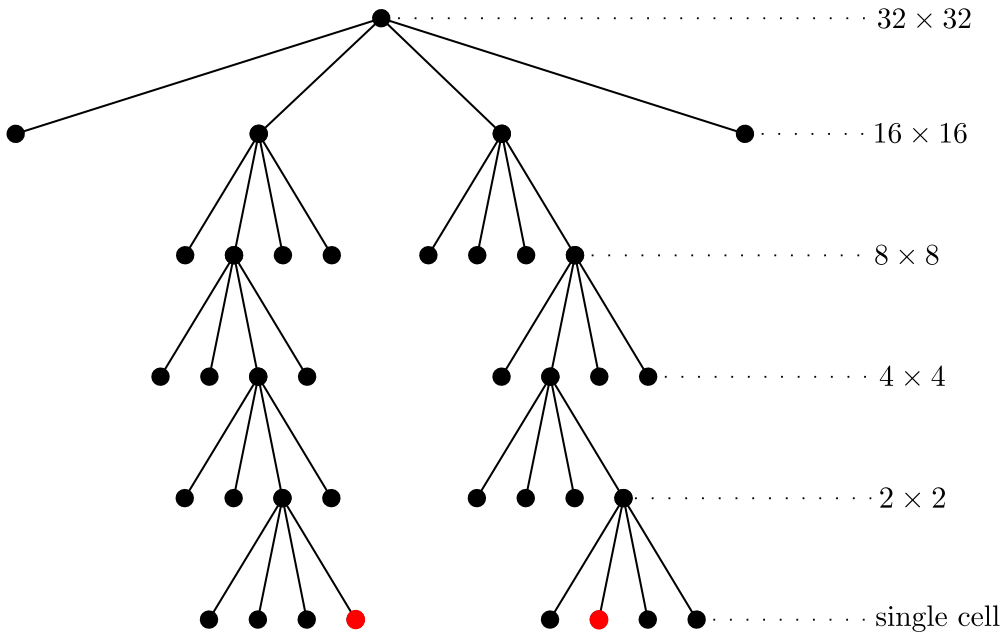

Figure 2.2: Example of quadtree data structure.

In what follows, a number of quadtree grids features are described. We also refer the reader to Chapter 3 for more information regarding quadtree generation.

2.5.1 Boundaries in quadtree grids

To be able to define boundaries in quadtree grids, a set of (seeding) points are defined. If the quadtree cells are within the boundaries of the set of boundary points, the scheme keeps those cell for the required computations. Otherwise, that cell is not required. It is also possible to refine the grid near boundaries. This depends on the problem and accuracy. We recommend refining the quadtree grid where boundaries are complex. This helps to capture and represent the actual boundaries of the domain in the computational grid.

2.5.2 Numbering system in quadtree grids

In quadtree grids, each cell gets a unique *identification number* (ID) based on its position in the tree as the tree proceeds. The ID has $2 \times m$ digits. At any level, the corresponding ID generates from the corresponding quadrants of its parent cell as

follows:

- north-west = 11
- north-east = 21
- south-west = 12
- south-east = 22

Pursuing zeroes are added to the ID to make sure each ID has the same length of $2 \times m$. The center coordinates of each cell can be computed from

$$\begin{cases} x = 0.5 + \sum_{i=1}^{l} \frac{1}{2^{m+1}}(2i_m - 3), & i_m \in O, \\ y = 0.5 - \sum_{i=1}^{l} \frac{1}{2^{m+1}}(2i_m - 3), & i_m \in E, \end{cases}$$

where l is the current cell level and i_m are the successive odd (O) or even (E) digits of the cell ID. Note that the origin of this system locates at the south-west corner of the root square [14].

2.5.3 Regularized quadtree grids

A quadtree grid that is generated only by its *seeding points* is called a *non-regularized* grid. To enhance the stability, reduce oscillations, and to have a less complicated formulation in the proposed numerical method, no cell can have both an adjacent neighbouring cell and a diagonally neighbouring cell with a refinement level difference greater than one [14, 33, 70, 71]. The quadtree grid becomes *regularized* with this condition. Figure 2.3 (left) represents a quadtree grid based on the quadtree data structure in Figure 2.2 (with two seeding points), as well as the regularized grid on the right.

2.5.4 Adaptivity

Quadtree grids employ adaptivity to numerical methods. An *adaptive* scheme is able to refine or coarsen the computational grid where it is needed. Several studies

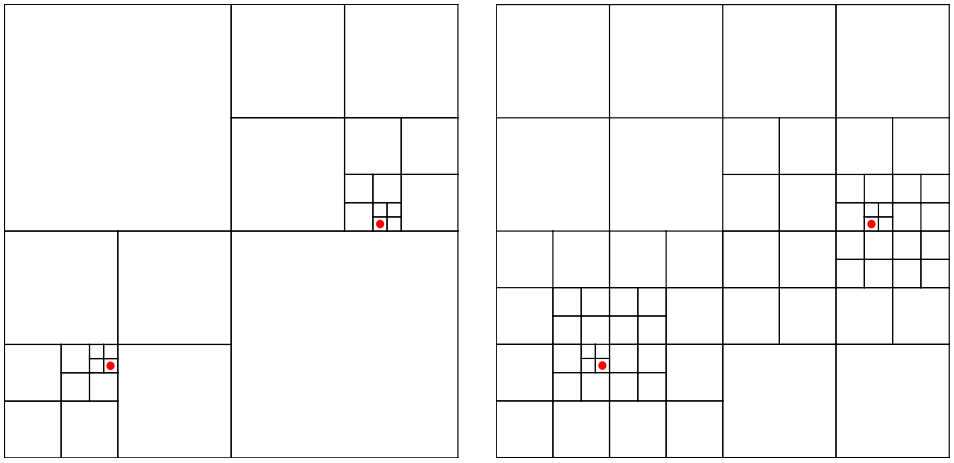

Figure 2.3: Examples of non-regularized (left) and regularized (right) quadtree grids.

have been conducted on quadtree grids. For example, an adaptive quadtree method for simulating fluid flows with moving interfaces [33], adaptive quadtree methods for the shallow water flows [13, 77], an adaptive model for the incompressible Euler equations in complex geometries [70], an adaptive spectral wave model [71], adaptive tsunami and ocean models [72, 73], an adaptive model of water-borne pollutant dispersion [14], an adaptive quadtree model of SWE with wet–dry fronts over complex topography [58], an adaptive scheme for the two-layer SWE [52], and SWE model over quadtree cut cell grids [2] have been introduced in the recent years. These mentioned studies show the importance of quadtree and adaptive schemes.

In this thesis, the scheme refines or coarsens the grid based on the gradient of scalar variables water surface (w) and density (ρ); wherever the absolute values of the these gradients are higher than a constant, the scheme adds a seeding point to refine the grid in that specific coordinate. In cases of having no seeding point, the scheme refines the grid with respect to minimum level of quadtree. The minimum level in a quadtree grid defines the maximum cell size. We choose the minimum level of the tree through trial and error. Increasing the minimum level of the tree increases the computational cost. In the following section, we briefly address the computational cost of the proposed scheme.

2.6 Computational cost

The focus of this work is to implement the central-upwind scheme that was introduced in [46] on quadtree grids. In the following chapters, it will be shown that the well-balanced scheme is more efficient compared to the non-well-balanced one due to having fewer computational cells in its computational grids. This work can also be extended to static grids. Static grids are very popular in computational hydrodynamics where the computational domains are often very large. Note that the adaptive quadtree scheme can be computationally expensive in oscillatory problems; the quadtree becomes close to a Cartesian grid. Therefore, adaptivity becomes redundant. The computational cost is also exponentially related to the level of refinement. One can reduce the computational cost by using smaller m. The drawback of this is dissipation and, therefore, accuracy is decreased.

In this work, the criteria that is chosen to apply seeding points to quadtree grids is investigating the local gradients. We use the local gradient of the water surface and the density for both the shallow water and variable density systems. The chosen constant to compare the local gradients with is different in each problem. The constant can be chosen with trial and error. Note that using the ratio of wave heights (can be guessed approximately) and the smallest cell length in the grid helps to find a good place to start finding the constant for the case of SWE.

Chapter 3

An adaptive well-balanced positivity preserving central-upwind scheme on quadtree grids for shallow water equations

[1]

3.1 Introduction

Quadtree grids (Figure 3.1), which are two-dimensional (2-D) semi-structured Cartesian grids, are based on hierarchical data structures, which are widely used in the fields of computer science (e.g., image processing and computer graphics), computational geometry, robotics, video games, and computational fluid dynamics; see, e.g., [81, 92]. Several studies have been conducted on how to generate quadtree grids; see, e.g., [1, 14, 32, 69, 71, 80, 82].

Cartesian grids are common in CFD problems because of their efficiency and ability to maintain the simplicity of discretized equations, which reduces computational cost in comparison to unstructured grids. One of the benefits of quadtree grids over structured grids is grid coarsening: while the accuracy is maintained, the grid can be coarsened wherever no refinement is needed and thus, the computational cost is reduced. Note that a disadvantage of Cartesian grids is their inability to ad-

[1] M. A. Ghazizadeh, A.Mohammadian, and A. Kurganov. An adaptive well-balanced positivity preserving central-upwind scheme on quadtree grids for shallow water equations, *Computers & Fluids*, under revision, 2020.

equately represent complex shapes. In such situations, cut-cell grids become useful; see, e.g., [2]. This paper will only focus on quadtree grids.

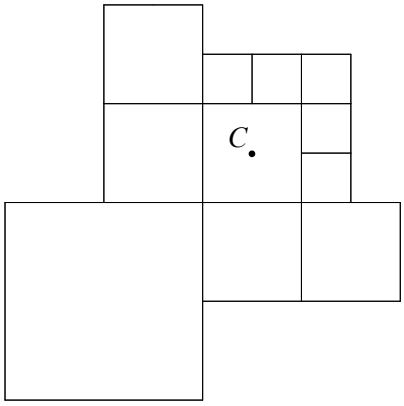

Figure 3.1: Example of quadtree cells with different level neighbouring cell sizes.

The main goal of this paper is to develop an adaptive well-balanced positivity preserving scheme on quadtree grids for the Saint-Venant system of shallow water equations. This system was first proposed in [20], but is still extensively used to model flows in rivers, lakes, coastal areas and estuaries [20]. In the 2-D case, the SWE can be written in terms of the water surface (w) and the unit discharges (hu and hv) as follows [16]:

$$\begin{cases} w_t + (hu)_x + (hv)_y = 0, \\ (hu)_t + \left[\dfrac{(hu)^2}{w-B} + \dfrac{g}{2}(w-B)^2\right]_x + \left[\dfrac{(hu)(hv)}{w-B}\right]_y = -g\,(w-B)B_x, \\ (hv)_t + \left[\dfrac{(hu)(hv)}{w-B}\right]_x + \left[\dfrac{(hv)^2}{w-B} + \dfrac{g}{2}(w-B)^2\right]_y = -g\,(w-B)B_y, \end{cases} \tag{3.1.1}$$

where t is time, g is the gravitational constant, x and y are the directions in the 2-D Cartesian coordinate system, $u(x,y,t)$ and $v(x,y,t)$ are the water velocities in the x- and y-directions, respectively, $B(x,y)$ is the bottom topography, and $h(x,y,t) = w(x,y,t) - B(x,y)$ is the water depth.

The system (3.1.1) admits "lake-at-rest" steady state solutions,

$$w \equiv \text{Const}, \quad u = v \equiv 0, \tag{3.1.2}$$

which are of great practical importance as many waves to be captured are, in fact, small perturbations of these steady states. We would like to stress that good numerical methods should be able of exactly preserving "lake-at-rest" steady states—such methods are called *well-balanced*. Another important property a good numerical method should possess is its ability to preserve non-negativity of water depth h—such methods are called *positivity preserving*. We refer the reader to, e.g., a recent review paper [42] for an extensive discussion on these matters.

Several numerical methods on quadtree grids for SWE have been developed during the past two decades. For example, an adaptive well-balanced second-order Godunov-type scheme was proposed in [77]. This scheme is able to solve the shallow water system with discontinuous bottom topography. A well-balanced scheme on quadtree-cut-cell grids was proposed in [2]. This scheme is based on the hydrostatic reconstruction from [4]. In addition, an adaptive quadtree Roe-type scheme for the 2-D two-layer SWE was introduced in [52]. Furthermore, an adaptive quadtree scheme with wet-dry fronts was studied [58, 57]. For further studies on SWE over quadtree grids, we refer the reader to [13, 14, 40, 59, 65]. Besides the aforementioned numerical methods, several well-balanced positivity preserving schemes have been proposed in the past years; see, e.g., [3, 4, 5, 10, 11, 12, 15, 26, 43, 46, 62, 74, 85], but none of them has been extended to quadtree grids.

In this paper, we present a quadtree scheme which is based on the central-upwind scheme from [46]. Central-upwind schemes are Godunov-type Riemann-problem-solver-free finite-volume methods, which were proposed in [44, 45, 47, 48] as a "black-box" solvers for general multidimensional systems of hyperbolic systems of conservation laws. Central-upwind schemes were extended to shallow water models in [43] and many subsequent works; see, e.g., the recent review paper [42] and references therein. The scheme from [46] is the first well-balanced and at the same time positivity preserving central-upwind scheme, which is simple, efficient and robust: this is the reason why it was taken as the main building block of the proposed quadtree scheme.

The paper is organized as follows. In §3.2, we briefly describe a quadtree grid generation algorithm. In §3.3, we develop a well-balanced positivity preserving central-upwind quadtree scheme. The developed scheme is tested on three numerical example in §3.4.

3.2 Quadtree grids

Quadtree grids imply recursive spatial decomposition of the computational domain; see Figure 3.1 for an example of a quadtree cell C with different level neighbouring cells. Quadtree grids can be generated according to the following algorithm (see [14, 32]):

Step 1. Choose a domain and generate a set of seeding points considering features of the problem, boundary conditions, flow characteristics, local gradients and governing equations.

Step 2. Fit the domain within a unit square (root square) by adjusting the size of the square.

Step 3. Determine the level of refinement (m) of the quadtree (the size of the smallest cell of the grid is inversely proportional to m).

Step 4. Divide the domain square into four sub-squares. Each sub-square is called a cell (that is, the first level of the quadtree).

Step 5. Continue dividing each cell into four sub-cells if it contains a seeding point until the maximum refinement level is reached. If a cell does not include any seeding points, move to the next cell and again implement Step 5.

We note that in order to prevent complicated formulations and enhance the stability of the overall method, no cell can have both an adjacent neighbouring cell and a diagonally neighbouring cell with a refinement level difference greater than one; see [14, 32, 70]. This condition is satisfied provided the quadtree is regularized; several regularization algorithms can be found in [8, 66, 79, 83, 84, 90]. Examples of non-regularized and regularized quadtree grids are shown in Figure 3.2.

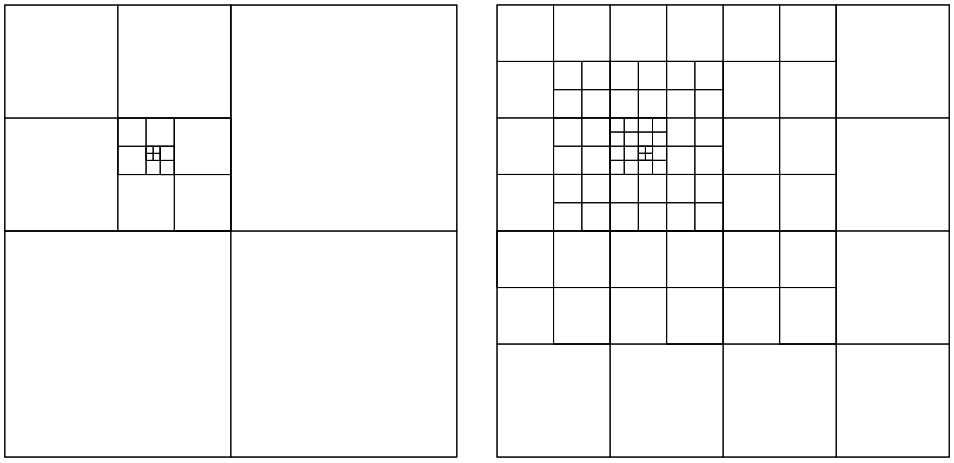

Figure 3.2: Examples of non-regularized (left) and regularized (right) quadtree grids.

3.3 Adaptive well-balanced semi-discrete central-upwind scheme

In this section, we present an adaptive well-balanced semi-discrete central-upwind scheme for the system (3.1.1), which can be written in the following vector form:

$$\boldsymbol{U}_t + \boldsymbol{F}(\boldsymbol{U}, B)_x + \boldsymbol{G}(\boldsymbol{U}, B)_y = \boldsymbol{S}(\boldsymbol{U}, B), \tag{3.3.1}$$

where

$$\boldsymbol{U} := (w, hu, hv)^\top,$$

and the fluxes and source term are:

$$\boldsymbol{F}(\boldsymbol{U}, B) = \left(hu, \frac{(hu)^2}{w-B} + \frac{g}{2}(w-B)^2, \frac{(hu)(hv)}{w-B}\right)^\top, \tag{3.3.2}$$

$$\boldsymbol{G}(\boldsymbol{U}, B) = \left(hv, \frac{(hu)(hv)}{w-B}, \frac{(hv)^2}{w-B} + \frac{g}{2}(w-B)^2\right)^\top, \tag{3.3.3}$$

$$\boldsymbol{S}(\boldsymbol{U}, B) = (0, -g(w-B)B_x, -g(w-B)B_y)^\top. \tag{3.3.4}$$

The central-upwind quadtree scheme will be designed according to the following algorithm:

Step 1. Generate a non-regularized grid with the seeding points (§3.2).

Step 2. Regularize the non-regularized grid (§3.2).

Step 3. Perform piecewise polynomial reconstructions and obtain the required point values of the bottom topography B (§3.3.2) and conservative quantities $\boldsymbol{U}$ (§3.3.3).

Step 4. Calculate the local speeds (§3.3.4) and central-upwind numerical fluxes (§3.3.5).

Step 5. Calculate the well-balanced discrete source term (§3.3.6).

Step 6. Calculate the size of timestep, which can guarantee the positivity and stability (§3.3.7).

Step 7. Calculate local gradients in each cell, which are needed to determine the seeding points at the next timestep (§3.3.8).

Step 8. Calculate current conservative quantities, which are going to be used as previous timestep data in the construction of the new quadtree grid (§3.3.8).

Step 9. Evolve the solution by solving the time-dependent system of ODE, obtained after the semi-discretization of the studied SWE over the quadtree grid.

3.3.1 Finite-volume semi-discretization over quadtree grids

Let us consider a typical finite-volume Cartesian cell $C_{j,k}$ of size $\Delta x_{j,k} \times \Delta y_{j,k}$ centered at $(x_{j,k}, y_{j,k})$. We assume that at a certain time level t, the computed solution is available and represented in terms of its cell averages:

$$\overline{\boldsymbol{U}}_{j,k}(t) \approx \frac{1}{\Delta x_{j,k}\Delta y_{j,k}} \int\limits_{x_{j-\frac{1}{2}}}^{x_{j+\frac{1}{2}}} \int\limits_{y_{k-\frac{1}{2}}}^{y_{k+\frac{1}{2}}} \boldsymbol{U}(x,y,t)\,\mathrm{d}y\,\mathrm{d}x, \tag{3.3.5}$$

where $x_{j\pm\frac{1}{2}} := x_{j,k} \pm \Delta x_{j,k}/2$ and $y_{k\pm\frac{1}{2}} := y_{j,k} \pm \Delta y_{j,k}/2$.

Considering the right and left neighbours of cell $C_{j,k}$, there exist nine different permutations of those neighbouring cells; see Figure 3.3. We note, however, that only eight of them (configurations (a)–(h) in Figure 3.3) are possible in the proposed regularized quadtree grid. Similar cases are to be considered with respect to the neighbouring cells on the top and bottom.

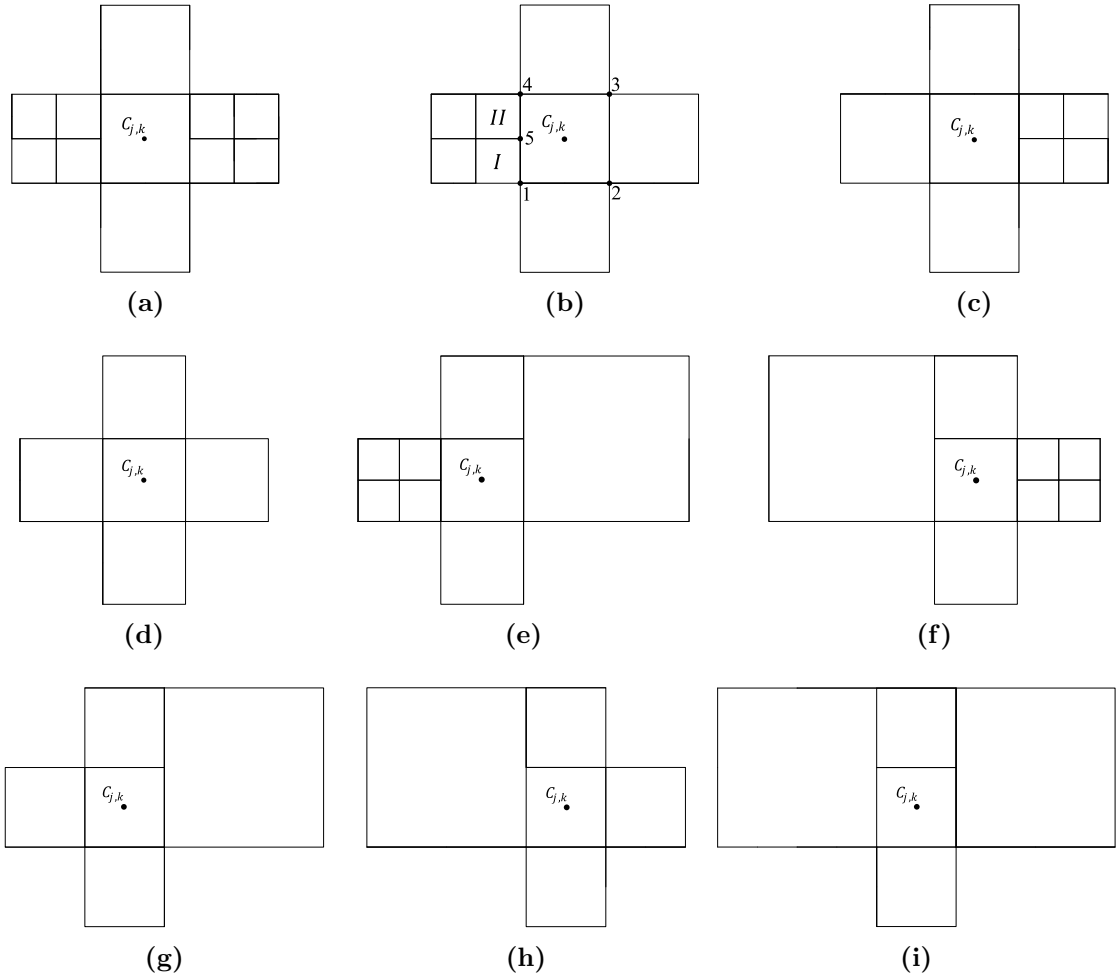

Figure 3.3: Permutations of neighbouring cells of $C_{j,k}$ in the x-direction: (a)–(h) Possible configurations in regularized quadtree grids; (i) An impossible configuration in regularized quadtree grids.

For the sake of brevity, we only present the quadtree scheme for configuration (b) in Figure 3.3 as an example of a quadtree cell (other configurations can be treated in a similar manner). We denote left-neighbouring cells of $C_{j,k}$ by I and II. These two cells centered at $(x_{j,k} - 3\Delta x_{j,k}/4, y_{j,k} \pm \Delta y_{j,k}/4)$ are of size $\Delta x_{j,k}/2 \times \Delta y_{j,k}/2$.

The cell averages $\overline{\boldsymbol{U}}_{j,k}$ are evolved in time by solving the following system of time-dependent ODE:

$$\frac{\mathrm{d}}{\mathrm{d}t}\overline{\boldsymbol{U}}_{j,k} = -\frac{\boldsymbol{H}^x_{j+\frac{1}{2},k} - \dfrac{\boldsymbol{H}^x_{j-\frac{1}{2},k-\frac{1}{4}} + \boldsymbol{H}^x_{j-\frac{1}{2},k+\frac{1}{4}}}{2}}{\Delta x_{j,k}} - \frac{\boldsymbol{H}^y_{j,k+\frac{1}{2}} - \boldsymbol{H}^y_{j,k-\frac{1}{2}}}{\Delta y_{j,k}} + \overline{\boldsymbol{S}}_{j,k}, \quad (3.3.6)$$

obtained after the semi-discretization of the system (3.3.1)–(3.3.4). In (3.3.6), $\boldsymbol{H}^x_{j+\frac{1}{2},k}$, $\boldsymbol{H}^x_{j-\frac{1}{2},k\pm\frac{1}{4}}$, $\boldsymbol{H}^y_{j,k+\frac{1}{2}}$ and $\boldsymbol{H}^y_{j,k-\frac{1}{2}}$ are the numerical fluxes, which, in general, are

$$\boldsymbol{H}^x_{\alpha,\beta}=\boldsymbol{H}^x(\boldsymbol{U}^-_{\alpha,\beta},\boldsymbol{U}^+_{\alpha,\beta};B_{\alpha,\beta})\quad\text{and}\quad\boldsymbol{H}^y_{\gamma,\delta}=\boldsymbol{H}^y(\boldsymbol{U}^-_{\gamma,\delta},\boldsymbol{U}^+_{\gamma,\delta};B_{\gamma,\delta}) \tag{3.3.7}$$

where

$$\boldsymbol{U}^\pm_{\alpha,\beta}=\lim_{x\to x_\alpha\pm0}\widetilde{\boldsymbol{U}}(x,y_\beta)\quad\text{and}\quad\boldsymbol{U}^\pm_{\gamma,\delta}=\lim_{y\to y_\delta\pm0}\widetilde{\boldsymbol{U}}(x_\gamma,y), \tag{3.3.8}$$

and $\widetilde{\boldsymbol{U}}$ is a piecewise polynomial interpolation. Second-order schemes employ piecewise linear interpolations,

$$\widetilde{\boldsymbol{U}}(x,y)=(\boldsymbol{U}_x)_{j,k}[x-x_j]+(\boldsymbol{U}_y)_{j,k}[y-y_k],\quad(x,y)\in C_{j,k}, \tag{3.3.9}$$

where the slopes $(\boldsymbol{U}_x)_{j,k}$ and $(\boldsymbol{U}_y)_{j,k}$ are yet to be determined; see §3.3.3 below. Finally, $\overline{\boldsymbol{S}}_{j,k}$ is a cell average of the source term:

$$\overline{\boldsymbol{S}}_{j,k}\approx\frac{1}{\Delta x_{j,k}\Delta y_{j,k}}\int\limits_{x_{j-\frac{1}{2}}}^{x_{j+\frac{1}{2}}}\int\limits_{y_{k-\frac{1}{2}}}^{y_{k+\frac{1}{2}}}\boldsymbol{S}(\boldsymbol{U},B)\,\mathrm{d}y\,\mathrm{d}x. \tag{3.3.10}$$

We note that all of the indexed quantities in (3.3.6)–(3.3.10) are time-dependent, but from now on we omit this dependence for the sake of brevity.

3.3.2 Piecewise bilinear reconstruction of B

The quadtree grid consist of cells of different sizes: $\Delta x\times\Delta y$, $\frac{\Delta x}{2}\times\frac{\Delta y}{2}$, …, $\frac{\Delta x}{2^{m-1}}\times\frac{\Delta y}{2^{m-1}}$. We denote the set of cells of the corresponding size by $\mathscr{C}^{(\ell)}$, that is, $\mathscr{C}^{(\ell)}=\{C_{j,k}:|C_{j,k}|=\frac{\Delta x}{2^{\ell-1}}\times\frac{\Delta y}{2^{\ell-1}}\}$.

We follow the lines of [46] and use a continuous piecewise bilinear reconstruction of the bottom topography $\widetilde{B}(x,y)$. We note that on a quadtree grid, the approach from [46] does not directly apply to a quadtree grid since it contains cells, whose vertex is a midpoint of the edge of the neighbouring cell as point 5 in the configuration considered in Figure 3.3 (b). We therefore propose the following algorithm for constructing $\widetilde{B}$.

Step 1. Set $\ell := 1$.

Step 2. Reconstruct bilinear pieces $\widetilde{B}$ for all (j,k) such that $C_{j,k} \in \mathscr{C}^{(\ell)}$. This is done as follows.

We first obtain the point values of B at the vertices of $C_{j,k}$. If one of them lies on the edge of a larger neighbouring cell (which belongs to the set $\mathscr{C}^{(\ell-1)}$ where the bilinear piece has already been constructed), then there are two possibilities:

(i) either this vertex coincides with a vertex of the neighbouring cell and then the point value of B has been already computed there;

(ii) or this vertex is a midpoint of the edge of the neighbouring cell and then the point value of B at this vertex is an average of the point values of B at those two vertices of the neighbouring cell that lie on the same edge (for example, in the configuration considered in Figure 3.3 (b), the value of B at point 5 will be equal to the average of the values of B at points 1 and 4).

Otherwise, we proceed as in [46] and set

$$B_{j\pm\frac{1}{2},k\pm\frac{1}{2}} := \frac{1}{2}\Big(\max_{\xi^2+\eta^2=1}\lim_{\ell_x,\ell_y\to 0} B(x_{j\pm\frac{1}{2}}+\ell_x\xi, y_{k\pm\frac{1}{2}}+\ell_y\eta) + \min_{\xi^2+\eta^2=1}\lim_{\ell_x,\ell_y\to 0} B(x_{j\pm\frac{1}{2}}+\ell_x\xi, y_{k\pm\frac{1}{2}}+\ell_y\eta)\Big),$$

which reduces to $B_{j\pm\frac{1}{2},k\pm\frac{1}{2}} = B(x_{j\pm\frac{1}{2}}, y_{k\pm\frac{1}{2}})$ if the function B is continuous at $(x_{j\pm\frac{1}{2}}, y_{k\pm\frac{1}{2}})$.

Equipped with the point values $B_{j\pm\frac{1}{2},k\pm\frac{1}{2}}$, we construct the following bilinear piece in cell $C_{j,k} \in \mathscr{C}^{(\ell)}$:

$$\begin{aligned}\widetilde{B}(x,y) = {} & B_{j-\frac{1}{2},k-\frac{1}{2}} + (B_{j+\frac{1}{2},k-\frac{1}{2}} - B_{j-\frac{1}{2},k-\frac{1}{2}})\,\frac{x-x_{j-\frac{1}{2}}}{\Delta x/2^{\ell-1}} \\ & + (B_{j-\frac{1}{2},k+\frac{1}{2}} - B_{j-\frac{1}{2},k-\frac{1}{2}})\,\frac{y-y_{k-\frac{1}{2}}}{\Delta y/2^{\ell-1}} \\ & + (B_{j+\frac{1}{2},k+\frac{1}{2}} - B_{j+\frac{1}{2},k-\frac{1}{2}} - B_{j-\frac{1}{2},k+\frac{1}{2}} + B_{j-\frac{1}{2},k-\frac{1}{2}})\,\frac{x-x_{j-\frac{1}{2}}}{\Delta x/2^{\ell-1}}\cdot\frac{y-y_{k-\frac{1}{2}}}{\Delta y/2^{\ell-1}}, \\ & (x,y) \in C_{j,k}.\end{aligned}$$

Step 3. Set $\ell := \ell + 1$.

Step 4. If $\ell \le m$, then go to Step 2.

Note that the restriction of the interpolant $\widetilde{B}$ along each of the cell is a linear function and the cell average of $\widetilde{B}$ over the cell $C_{j,k}$ is equal to its value at the center of the cell and is also equal to the average of the values of $\widetilde{B}$ at the midpoints of the edges of $C_{j,k}$, namely, we have

$$\begin{aligned} B_{j,k} := \widetilde{B}(x_j, y_k) &= \frac{1}{\Delta x_{j,k}\Delta y_{j,k}} \iint\limits_{C_{j,k}} \widetilde{B}(x,y)\,\mathrm{d}x\,\mathrm{d}y \\ &= \frac{B_{j+\frac{1}{2},k} + B_{j-\frac{1}{2},k} + B_{j,k+\frac{1}{2}} + B_{j,k-\frac{1}{2}}}{4}, \end{aligned} \tag{3.3.11}$$

where

$$B_{j\pm\frac{1}{2},k} := \widetilde{B}(x_{j\pm\frac{1}{2}}, y_k) = \frac{1}{2}\left(B_{j\pm\frac{1}{2},k+\frac{1}{2}} + B_{j\pm\frac{1}{2},k-\frac{1}{2}}\right), \tag{3.3.12}$$

and

$$B_{j,k\pm\frac{1}{2}} := \widetilde{B}(x_j, y_{k\pm\frac{1}{2}}) = \frac{1}{2}\left(B_{j+\frac{1}{2},k\pm\frac{1}{2}} + B_{j-\frac{1}{2},k\pm\frac{1}{2}}\right). \tag{3.3.13}$$

We also note that the values of B at the midpoints of the right edges of cells I and II in configuration considered in Figure 3.3 (b) can be obtained in a similar way:

$$B_{j-\frac{1}{2},k\pm\frac{1}{4}} := \widetilde{B}(x_{j-\frac{1}{2}}, y_{k\pm\frac{1}{4}}) = \frac{1}{2}\left(B_{j-\frac{1}{2},k} + B_{j-\frac{1}{2},k\pm\frac{1}{2}}\right). \tag{3.3.14}$$

Formulae (3.3.11)–(3.3.14) are crucial for the proof of the positivity preserving property of our well-balanced quadtree central-upwind scheme; see §3.3.7.

Remark. We note that the proposed piecewise bilinear reconstruction can be applied to discontinuous bottom functions $B(x,y)$.

3.3.3 Piecewise linear reconstruction of $\boldsymbol{U}$

In this paper, we design a second-order scheme, which employs a piecewise linear reconstruction $\widetilde{\boldsymbol{U}}$ in each cell. We then obtain the point values of $\boldsymbol{U}$ (required in (3.3.7)) using (3.3.8), (3.3.9), which for cell $C_{j,k}$ from Figure 3.3 (b) results in

$$\begin{aligned} \boldsymbol{U}^{+}_{j+\frac{1}{2},k} &= \overline{\boldsymbol{U}}_{j+1,k} - \frac{\Delta x_{j+1,k}}{2}(\boldsymbol{U}_x)_{j+1,k} \\ \boldsymbol{U}^{-}_{j+\frac{1}{2},k} &= \overline{\boldsymbol{U}}_{j,k} + \frac{\Delta x_{j,k}}{2}(\boldsymbol{U}_x)_{j,k}\,, \end{aligned}$$

$$\begin{aligned}\boldsymbol{U}^{+}_{j-\frac{1}{2},k\pm\frac{1}{4}} &= \overline{\boldsymbol{U}}_{j,k} - \frac{\Delta x_{j,k}}{2}(\boldsymbol{U}_x)_{j,k} \pm \frac{\Delta y_{j,k}}{2}(\boldsymbol{U}_y)_{j,k}\,,\\ \boldsymbol{U}^{-}_{j-\frac{1}{2},k\pm\frac{1}{4}} &= \overline{\boldsymbol{U}}_{j-\frac{1}{4},k\pm\frac{1}{4}} + \frac{\Delta x_{j,k}}{4}(\boldsymbol{U}_x)_{j-\frac{1}{4},k\pm\frac{1}{4}}\end{aligned} \tag{3.3.15}$$

where $\overline{\boldsymbol{U}}_{j-\frac{1}{4},k-\frac{1}{4}}$ and $\overline{\boldsymbol{U}}_{j-\frac{1}{4},k+\frac{1}{4}}$ denote the cell averages of $\boldsymbol{U}$ over the cells I and II, respectively.

In order to achieve the formal second order of accuracy, the slopes $(\boldsymbol{U}_x)$ and $(\boldsymbol{U}_y)$ in (3.3.15) are to be at least first-order approximations of the corresponding derivatives. In order to minimize oscillations, we compute the slopes using the minmod limiter (see, e.g., [7, 50, 88]), which is implemented in the following way:

$$\begin{aligned}(\boldsymbol{U}_x)_{j,k} &= \text{minmod}\left(\frac{\overline{\boldsymbol{U}}_{j,k} - \overline{\boldsymbol{U}}_{j-\frac{1}{4},k-\frac{1}{4}}}{3\Delta x_{j,k}/4}, \frac{\overline{\boldsymbol{U}}_{j,k} - \overline{\boldsymbol{U}}_{j-\frac{1}{4},k+\frac{1}{4}}}{3\Delta x_{j,k}/4}, \frac{\overline{\boldsymbol{U}}_{j+1,k} - \overline{\boldsymbol{U}}_{j,k}}{\Delta x_{j,k}}\right),\\ (\boldsymbol{U}_y)_{j,k} &= \text{minmod}\left(\frac{\overline{\boldsymbol{U}}_{j,k} - \overline{\boldsymbol{U}}_{j,k-1}}{\Delta y_{j,k}}, \frac{\overline{\boldsymbol{U}}_{j,k+1} - \overline{\boldsymbol{U}}_{j,k}}{\Delta y_{j,k}}\right)\end{aligned} \tag{3.3.16}$$

where the minmod function is defined by

$$min\{z_1, z_2, ...\} := \begin{cases} min_j\{z_j\}, & \text{if } z_j > 0 \quad \forall j,\\ max_j\{z_j\}, & \text{if } z_j < 0 \quad \forall j,\\ 0, & \text{otherwise.}\end{cases}$$

3.3.3.1 Positivity preserving correction of w

The piecewise linear reconstruction (3.3.16) cannot guarantee the non-negativity of

$$\widetilde{h}(x,y) := \widetilde{w}(x,y) - \widetilde{B}(x,y).$$

In fact, for the configuration considered in Figure 3.3 (b), we only need the following five inequalities to be satisfied:

$$\begin{aligned}&h^{+}_{j-\frac{1}{2},k\pm\frac{1}{4}} = w^{+}_{j-\frac{1}{2},k\pm\frac{1}{4}} - B_{j-\frac{1}{2},k\pm\frac{1}{4}} \geq 0, \quad h^{-}_{j+\frac{1}{2},k} = w^{-}_{j+\frac{1}{2},k} - B_{j+\frac{1}{2},k} \geq 0,\\ &h^{+}_{j,k-\frac{1}{2}} = w^{+}_{j,k-\frac{1}{2}} - B_{j,k-\frac{1}{2}} \geq 0, \quad \text{and} \quad h^{-}_{j,k+\frac{1}{2}} = w^{-}_{j,k+\frac{1}{2}} - B_{j,k+\frac{1}{2}} \geq 0.\end{aligned}$$

If at least one of these inequalities is not satisfied, we need to correct $\widetilde{w}$ in the cell $C_{j,k}$. We note that the correction used in [46] will not in general work on quadtree grids. We therefore propose an alternative correction procedure and replace the linear pieces in the problematic cells with the bilinear one denoted by $\mathring{w}(x,y)$ and constructed as follows. Let us denote by

$$\begin{aligned} w^{\rm NE}_{j,k} &:= \widetilde{w}(x_{j+\frac12}-0, y_{k+\frac12}-0), \quad w^{\rm SE}_{j,k} := \widetilde{w}(x_{j+\frac12}-0, y_{k-\frac12}+0),\\ w^{\rm NW}_{j,k} &:= \widetilde{w}(x_{j-\frac12}+0, y_{k+\frac12}-0), \quad w^{\rm SW}_{j,k} := \widetilde{w}(x_{j-\frac12}+0, y_{k-\frac12}+0) \end{aligned}$$

the four corner point values of the linear piece of $\widetilde{w}$ over the cell $C_{j,k}$. If

$$\begin{aligned} &w^{\rm NE}_{j,k} \ge B_{j+\frac12,k+\frac12}, \quad w^{\rm SE}_{j,k} \ge B_{j+\frac12,k-\frac12},\\ &w^{\rm NW}_{j,k} \ge B_{j-\frac12,k+\frac12} \quad \text{and} \quad w^{\rm SW}_{j,k} \ge B_{j-\frac12,k-\frac12}, \end{aligned} \tag{3.3.17}$$

then we set

$$\begin{aligned} \mathring{w}(x,y) =& w^{\rm SW}_{j,k} + (w^{\rm SE}_{j,k} - w^{\rm SW}_{j,k})\,\frac{x-x_{j-\frac12}}{\Delta x_{j,k}} + (w^{\rm NW}_{j,k} - w^{\rm SW}_{j,k})\,\frac{y-y_{k-\frac12}}{\Delta y_{j,k}}\\ &+ (w^{\rm NE}_{j,k} - w^{\rm SE}_{j,k} - w^{\rm NW}_{j,k} + w^{\rm SW}_{j,k})\,\frac{x-x_{j-\frac12}}{\Delta x_{j,k}}\cdot\frac{y-y_{k-\frac12}}{\Delta y_{j,k}}, \quad (x,y)\in C_{j,k}. \end{aligned} \tag{3.3.18}$$

If at least one of the inequalities in (3.3.17) is not satisfied, we would first need to correct the point values of w at the vertices of $C_{j,k}$. There are three different cases to be considered.

Case 1: only one of the inequalities in (3.3.17) *is not satisfied.* Without loss of generality, we assume that $w^{\rm NE}_{j,k} < B_{j+\frac12,k+\frac12}$. We then replace the point values of w at the vertices of $C_{j,k}$ with

$$\begin{aligned} &\mathring{w}^{\rm NE}_{j,k} = B_{j+\frac12,k+\frac12}, \quad \mathring{w}^{\rm SE}_{j,k} = B_{j+\frac12,k-\frac12} + \frac43(\overline{w}_{j,k} - B_{j,k}),\\ &\mathring{w}^{\rm NW}_{j,k} = B_{j-\frac12,k+\frac12} + \frac43(\overline{w}_{j,k} - B_{j,k}), \quad \mathring{w}^{\rm SW}_{j,k} = B_{j-\frac12,k-\frac12} + \frac43(\overline{w}_{j,k} - B_{j,k}). \end{aligned}$$

Case 2: only two of the inequalities in (3.3.17) *are not satisfied.* Without loss of generality, we assume that $w^{\rm NE}_{j,k} < B_{j+\frac12,k+\frac12}$ and $w^{\rm SE}_{j,k} < B_{j+\frac12,k-\frac12}$. We then replace

the point values of w at the vertices of $C_{j,k}$ with

$$\mathring{w}^{\mathrm{NE}}_{j,k} = B_{j+\frac{1}{2},k+\frac{1}{2}}, \quad \mathring{w}^{\mathrm{SE}}_{j,k} = B_{j+\frac{1}{2},k-\frac{1}{2}},$$
$$\mathring{w}^{\mathrm{NW}}_{j,k} = B_{j-\frac{1}{2},k+\frac{1}{2}} + 2(\overline{w}_{j,k} - B_{j,k}), \quad \mathring{w}^{\mathrm{SW}}_{j,k} = B_{j-\frac{1}{2},k-\frac{1}{2}} + 2(\overline{w}_{j,k} - B_{j,k}).$$

Case 3: only three of the inequalities in (3.3.17) *are not satisfied.* Without loss of generality, we assume that $w^{\mathrm{NE}}_{j,k} < B_{j+\frac{1}{2},k+\frac{1}{2}}$, $w^{\mathrm{SE}}_{j,k} < B_{j+\frac{1}{2},k-\frac{1}{2}}$ and $w^{\mathrm{NW}}_{j,k} < B_{j-\frac{1}{2},k+\frac{1}{2}}$. We then replace the point values of w at the vertices of $C_{j,k}$ with

$$\mathring{w}^{\mathrm{NE}}_{j,k} = B_{j+\frac{1}{2},k+\frac{1}{2}}, \quad \mathring{w}^{\mathrm{SE}}_{j,k} = B_{j+\frac{1}{2},k-\frac{1}{2}}, \quad \mathring{w}^{\mathrm{NW}}_{j,k} = B_{j-\frac{1}{2},k+\frac{1}{2}},$$
$$\mathring{w}^{\mathrm{SW}}_{j,k} = 4\,\overline{w}_{j,k} - B_{j+\frac{1}{2},k+\frac{1}{2}} - B_{j+\frac{1}{2},k-\frac{1}{2}} - B_{j-\frac{1}{2},k+\frac{1}{2}}.$$

In all of the above three cases, we use the corrected point values $\mathring{w}^{\mathrm{NE}}_{j,k}$, $\mathring{w}^{\mathrm{SE}}_{j,k}$, $\mathring{w}^{\mathrm{NW}}_{j,k}$ and $\mathring{w}^{\mathrm{SW}}_{j,k}$ to construct the corrected bilinear approximant (compare with (3.3.18))

$$\begin{aligned}\mathring{w}(x,y) = {} & \mathring{w}^{\mathrm{SW}}_{j,k} + (\mathring{w}^{\mathrm{SE}}_{j,k} - \mathring{w}^{\mathrm{SW}}_{j,k})\,\frac{x - x_{j-\frac{1}{2}}}{\Delta x_{j,k}} + (\mathring{w}^{\mathrm{NW}}_{j,k} - \mathring{w}^{\mathrm{SW}}_{j,k})\,\frac{y - y_{k-\frac{1}{2}}}{\Delta y_{j,k}} \\ & + (\mathring{w}^{\mathrm{NE}}_{j,k} - \mathring{w}^{\mathrm{SE}}_{j,k} - \mathring{w}^{\mathrm{NW}}_{j,k} + \mathring{w}^{\mathrm{SW}}_{j,k})\,\frac{x - x_{j-\frac{1}{2}}}{\Delta x_{j,k}} \cdot \frac{y - y_{k-\frac{1}{2}}}{\Delta y_{j,k}}, \quad (x,y) \in C_{j,k}.\end{aligned}$$

It is easy to show that the constructed bilinear piece $\mathring{w}(x,y)$ is conservative, that is,

$$\frac{1}{\Delta x_{j,k}\Delta y_{j,k}} \int\limits_{C_{j,k}} \mathring{w}(x,y)\,\mathrm{d}y\,\mathrm{d}x = \overline{w}_{j,k},$$

and positivity preserving, that is,

$$\mathring{w}(x,y) \geq \widetilde{B}(x,y), \quad (x,y) \in C_{j,k}.$$

We also notice that the point values of w (required in (3.3.7)) at the cell $C_{j,k}$ from Figure 3.3 (b) are

$$w^{+}_{j-\frac{1}{2},k\pm\frac{1}{4}} = \mathring{w}(x_{j-\frac{1}{2}} + 0, y_{k\pm\frac{1}{4}}), \qquad w^{-}_{j+\frac{1}{2},k} = \mathring{w}(x_{j+\frac{1}{2}} - 0, y_k),$$
$$w^{+}_{j,k-\frac{1}{2}} = \mathring{w}(x_j, y_{k-\frac{1}{2}} + 0), \qquad w^{-}_{j,k+\frac{1}{2}} = \mathring{w}(x_j, y_{k+\frac{1}{2}} - 0)$$

and thus the corresponding corrected values of h,

$$h^+_{j-\frac{1}{2},k\pm\frac{1}{4}} = w^+_{j-\frac{1}{2},k\pm\frac{1}{4}} - B_{j-\frac{1}{2},k\pm\frac{1}{4}}, \qquad h^-_{j+\frac{1}{2},k} = w^-_{j+\frac{1}{2},k} - B_{j+\frac{1}{2},k},$$
$$h^+_{j,k-\frac{1}{2}} = w^+_{j,k-\frac{1}{2}} - B_{j,k-\frac{1}{2}}, \qquad h^-_{j,k+\frac{1}{2}} = w^-_{j,k+\frac{1}{2}} - B_{j,k+\frac{1}{2}},$$

are nonnegative.

Finally, we would like to point out that the values of h at the boundaries of cell $C_{j,k}$ may be very small or even zero. This will require the computation of the corresponding point values of u and v to be desingularized. We use the desingularization approach from [46]:

$$u := \frac{\sqrt{2}h(hu)}{\sqrt{h^4 + \max\{h^4, \varepsilon\}}}, \qquad v := \frac{\sqrt{2}h(hv)}{\sqrt{h^4 + \max\{h^4, \varepsilon\}}},$$

where we take $\varepsilon = \max\{\min_{j,k}\{(\Delta x_{j,k})^4\}, \min_{j,k}\{(\Delta y_{j,k})^4\}\}$. After recomputing the point values of h, u and v, the x- and y-discharges are also recalculated by setting:

$$(hu) := h \cdot u, \qquad (hv) := h \cdot v.$$

Note that in the above two equations, we have omitted all of the indices for the sake of brevity.

3.3.4 Local speeds

The one-sided local speeds of propagation, denoted at the corresponding cell interfaces by $a^\pm_{\alpha,\beta}$ and $b^\pm_{\gamma,\delta}$, are calculated using the largest and smallest eigenvalues of the Jacobian matrices $\frac{\partial \boldsymbol{F}}{\partial \boldsymbol{U}}$ and $\frac{\partial \boldsymbol{G}}{\partial \boldsymbol{U}}$ and can be estimated by

$$\begin{aligned}
a^+_{\alpha,\beta} &= \max\left\{u^+_{\alpha,\beta} + \sqrt{gh^+_{\alpha,\beta}},\ u^-_{\alpha,\beta} + \sqrt{gh^-_{\alpha,\beta}},\ 0\right\},\\
a^-_{\alpha,\beta} &= \min\left\{u^+_{\alpha,\beta} - \sqrt{gh^+_{\alpha,\beta}},\ u^-_{\alpha,\beta} - \sqrt{gh^-_{\alpha,\beta}},\ 0\right\},\\
b^+_{\gamma,\delta} &= \max\left\{v^+_{\gamma,\delta} + \sqrt{gh^+_{\gamma,\delta}},\ v^-_{\gamma,\delta} + \sqrt{gh^-_{\gamma,\delta}},\ 0\right\},\\
b^-_{\gamma,\delta} &= \min\left\{v^+_{\gamma,\delta} - \sqrt{gh^+_{\gamma,\delta}},\ v^-_{\gamma,\delta} - \sqrt{gh^-_{\gamma,\delta}},\ 0\right\}.
\end{aligned} \tag{3.3.19}$$

3.3.5 Central-upwind numerical fluxes

We use the central-upwind fluxes from [46], originally derived in [49]:

$$\begin{aligned}\boldsymbol{H}^x_{\alpha,\beta} =& \frac{a^+_{\alpha,\beta}\boldsymbol{F}(\boldsymbol{U}^-_{\alpha,\beta}, B_{\alpha,\beta}) - a^-_{\alpha,\beta}\boldsymbol{F}(\boldsymbol{U}^+_{\alpha,\beta}, B_{\alpha,\beta})}{a^+_{\alpha,\beta} - a^-_{\alpha,\beta}} \\ &+ \frac{a^+_{\alpha,\beta}a^-_{\alpha,\beta}}{a^+_{\alpha,\beta} - a^-_{\alpha,\beta}}\left[\boldsymbol{U}^+_{\alpha,\beta} - \boldsymbol{U}^-_{\alpha,\beta}\right],\end{aligned}$$

$$\begin{aligned}\boldsymbol{H}^y_{\gamma,\delta} =& \frac{b^+_{\gamma,\delta}\boldsymbol{G}(\boldsymbol{U}^-_{\gamma,\delta}, B_{\gamma,\delta}) - b^-_{\gamma,\delta}\boldsymbol{G}(\boldsymbol{U}^+_{\gamma,\delta}, B_{\gamma,\delta})}{b^+_{\gamma,\delta} - b^-_{\gamma,\delta}} \\ &+ \frac{b^+_{\gamma,\delta}b^-_{\gamma,\delta}}{b^+_{\gamma,\delta} - b^-_{\gamma,\delta}}\left[\boldsymbol{U}^+_{\gamma,\delta} - \boldsymbol{U}^-_{\gamma,\delta}\right],\end{aligned} \tag{3.3.20}$$

where

$$(\alpha,\beta) \in \left\{(j-\frac{1}{2}, k-\frac{1}{4}), (j-\frac{1}{2}, k+\frac{1}{4}), (j+\frac{1}{2}, k)\right\}$$

and

$$(\gamma,\delta) \in \left\{(j, k-\frac{1}{2}), (j, k+\frac{1}{2})\right\}$$

in the configuration considered in Figure 3.3 (b).

3.3.6 Well-balanced discretization of the source term

A numerical scheme is well-balanced when the discretized cell average of the source term, $\overline{\boldsymbol{S}}_{j,k} = \left(0, \overline{S}^{(2)}_{j,k}, \overline{S}^{(3)}_{j,k}\right)^\top$, exactly balances the numerical fluxes in equation (3.3.6) at the "lake-at-rest" steady state (3.1.2), that is, when the right-hand side (RHS) of (3.3.6) vanishes as long as $\overline{\boldsymbol{U}}_{j,k} \equiv (\widehat{w}, 0, 0)^\top$ for all (j,k), where $\widehat{w}$ is a constant.

We note that at the "lake-at-rest data", all of the reconstructed point values are $w^\pm = \widetilde{w}$ and $u^\pm = v^\pm = 0$ and thus, $a^+_{\alpha,\beta} = -a^-_{\alpha,\beta}$, $\forall(\alpha,\beta)$, $b^+_{\gamma,\delta} = -b^-_{\gamma,\delta}\,\forall(\gamma,\delta)$, and the numerical fluxes (3.3.20) reduce to

$$\boldsymbol{H}^x_{\alpha,\beta} = \left(0, \frac{g}{2}\left(\widehat{w} - B_{\alpha,\beta}\right)^2, 0\right)^\top, \quad \boldsymbol{H}^y_{\gamma,\delta} = \left(0, 0, \frac{g}{2}\left(\widehat{w} - B_{\gamma,\delta}\right)^2\right)^\top,$$

and the flux terms on the RHS of (3.3.6) then become

$$-\frac{\boldsymbol{H}^x_{j+\frac12,k}-\dfrac{\boldsymbol{H}^x_{j-\frac12,k-\frac14}+\boldsymbol{H}^x_{j-\frac12,k+\frac14}}{2}}{\Delta x_{j,k}}-\frac{\boldsymbol{H}^y_{j,k+\frac12}-\boldsymbol{H}^y_{j,k-\frac12}}{\Delta y_{j,k}}$$
$$=-\frac{g}{2}\begin{pmatrix}0\\ \dfrac{\left(\widehat{w}-B_{j+\frac12,k}\right)^2}{\Delta x_{j,k}}-\dfrac{\left(\widehat{w}-B_{j-\frac12,k-\frac14}\right)^2}{2\Delta x_{j,k}}-\dfrac{\left(\widehat{w}-B_{j-\frac12,k+\frac14}\right)^2}{2\Delta x_{j,k}}\\ \dfrac{\left(\widehat{w}-B_{j,k+\frac12}\right)^2}{\Delta y_{j,k}}-\dfrac{\left(\widehat{w}-B_{j,k-\frac12}\right)^2}{\Delta y_{j,k}}\end{pmatrix}. \tag{3.3.21}$$

We now need to approximate the source term in (3.3.6) in such a way that $\overline{\boldsymbol{S}}_{j,k}$ would cancel (3.3.21) at the "lake-at-rest" steady states. To this end, we first notice that (at least for smooth solutions)

$$\begin{aligned}-g(w-B)B_x&=g(w-B)(w-B)_x-g(w-B)w_x\\&=\frac{g}{2}\left[(w-B)^2\right]_x-g(w-B)w_x,\\-g(w-B)B_y&=g(w-B)(w-B)_y-g(w-B)w_y\\&=\frac{g}{2}\left[(w-B)^2\right]_y-g(w-B)w_y,\end{aligned}$$

and rewrite the cell averages of the second and third components of the integral in (3.3.10) as

$$\frac{g}{2}\int\limits_{y_{k-\frac12}}^{y_{k+\frac12}}\left[(w-B)^2\Big|_{x=x_{j+\frac12}}-(w-B)^2\Big|_{x=x_{j-\frac12}}\right]\mathrm{d}y-$$
$$g\int\limits_{x_{j-\frac12}}^{x_{j+\frac12}}\int\limits_{y_{k-\frac12}}^{y_{k+\frac12}}(w-B)w_x\,\mathrm{d}y\,\mathrm{d}x \tag{3.3.22}$$

and

$$\frac{g}{2}\int\limits_{x_{j-\frac{1}{2}}}^{x_{j+\frac{1}{2}}}\left[(w-B)^2\Big|_{y=y_{k+\frac{1}{2}}}-(w-B)^2\Big|_{y=y_{k-\frac{1}{2}}}\right]\mathrm{d}x-$$
$$g\int\limits_{x_{j-\frac{1}{2}}}^{x_{j+\frac{1}{2}}}\int\limits_{y_{k-\frac{1}{2}}}^{y_{k+\frac{1}{2}}}(w-B)w_y\,\mathrm{d}y\,\mathrm{d}x, \tag{3.3.23}$$

respectively. We then approximate the integrals in (3.3.22) and (3.3.23) using the second-order midpoint rule (for the configuration in Figure 3.3 (b), the integral along the left edge of $C_{j,k}$ is approximated using the composite midpoint rule as $C_{j,k}$ has two neighbouring cells on the left), which results in the following quadrature for the second and third components of the source term:

$$\overline{S}^{(2)}_{j,k}\approx\frac{g}{2\Delta x_{j,k}}\left[\left(w^-_{j+\frac{1}{2},k}-B_{j+\frac{1}{2},k}\right)^2-\frac{\left(w^+_{j-\frac{1}{2},k-\frac{1}{4}}-B_{j-\frac{1}{2},k-\frac{1}{4}}\right)^2}{2}\right.$$
$$\left.-\frac{\left(w^+_{j-\frac{1}{2},k+\frac{1}{4}}-B_{j-\frac{1}{2},k+\frac{1}{4}}\right)^2}{2}\right]-g(w_x)_{j,k}\left(\overline{w}_{j,k}-B_{j,k}\right),$$

$$\overline{S}^{(3)}_{j,k}\approx\frac{g}{2\Delta y_{j,k}}\left[\left(w^-_{j,k+\frac{1}{2}}-B_{j,k+\frac{1}{2}}\right)^2-\left(w^+_{j,k-\frac{1}{2}}-B_{j,k-\frac{1}{2}}\right)^2\right]$$
$$-g(w_y)_{j,k}\left(\overline{w}_{j,k}-B_{j,k}\right). \tag{3.3.24}$$

We finally note that at the "lake-at-rest" data, $(w_x)_{j,k}=(w_y)_{j,k}\equiv 0$, $\forall(j,k)$ and thus (3.3.21) and (3.3.24) imply that the RHS of (3.3.6) vanishes and the resulting scheme is well-balanced.

3.3.7 Positivity preserving property and time discretization

One of the main advantages of the central-upwind scheme is its ability to preserve the positivity of h; see [42, 46]. In this section, we extend the positivity proof from [46] to the proposed quadtree scheme. To this end, we integrate equation (3.3.6) in

time using a forward Euler method. For the first component, this results in

$$\overline{w}_{j,k}^{n+1} = \overline{w}_{j,k}^{n} - \lambda_{j,k}^{n}\left(H^{x,(1)}_{j+\frac{1}{2},k} - \frac{H^{x,(1)}_{j-\frac{1}{2},k-\frac{1}{4}} + H^{x,(1)}_{j-\frac{1}{2},k+\frac{1}{4}}}{2}\right) - \mu_{j,k}^{n}\left(H^{y,(1)}_{j,k+\frac{1}{2}} - H^{y,(1)}_{j,k-\frac{1}{2}}\right), \tag{3.3.25}$$

where $\overline{w}_{j,k}^{n} := \overline{w}_{j,k}(t^n)$ and $\overline{w}_{j,k}^{n+1} := \overline{w}_{j,k}(t^{n+1})$ with $t^{n+1} = t^n + \Delta t^n$, $\lambda_{j,k}^{n} := \Delta t^n/\Delta x_{j,k}$, $\mu_{j,k}^{n} := \Delta t^n/\Delta y_{j,k}$, and the numerical fluxes on the RHS are evaluated at time level $t = t^n$ using (3.3.20):

$$\begin{aligned} H^{x,(1)}_{\alpha,\beta} =& \frac{a^+_{\alpha,\beta}(hu)^-_{\alpha,\beta} - a^-_{\alpha,\beta}(hu)^+_{\alpha,\beta}}{a^+_{\alpha,\beta} - a^-_{\alpha,\beta}} + \frac{a^+_{\alpha,\beta}a^-_{\alpha,\beta}}{a^+_{\alpha,\beta} - a^-_{\alpha,\beta}}\left[w^+_{\alpha,\beta} - w^-_{\alpha,\beta}\right], \\ H^{y,(1)}_{\gamma,\delta} =& \frac{b^+_{\gamma,\delta}(hv)^-_{\gamma,\delta} - b^-_{\gamma,\delta}(hv)^+_{\gamma,\delta}}{b^+_{\gamma,\delta} - b^-_{\gamma,\delta}} + \frac{b^+_{\gamma,\delta}b^-_{\gamma,\delta}}{b^+_{\gamma,\delta} - b^-_{\gamma,\delta}}\left[w^+_{\gamma,\delta} - w^-_{\gamma,\delta}\right], \end{aligned} \tag{3.3.26}$$

where, as before,

$$(\alpha,\beta) \in \left\{(j-\frac{1}{2},k-\frac{1}{4}),(j-\frac{1}{2},k+\frac{1}{4}),(j+\frac{1}{2},k)\right\}$$

and

$$(\gamma,\delta) \in \left\{(j,k-\frac{1}{2}),(j,k+\frac{1}{2})\right\}$$

in the configuration considered in Figure 3.3 (b).

If $\overline{h}_{j,k}^{n} \geq 0$ for all (j,k), then the point values of h computed using piecewise linear/bilinear reconstructions of w and B presented in §3.3.2 and §3.3.3, are non-negative. Moreover, using (3.3.11)–(3.3.14) and the similar relationships for the reconstructed point values of w, we have

$$\overline{h}_{j,k}^{n} = \frac{1}{4}\left(\frac{h^+_{j-\frac{1}{2},k-\frac{1}{4}} + h^+_{j-\frac{1}{2},k+\frac{1}{4}}}{2} + h^-_{j+\frac{1}{2},k} + h^+_{j,k-\frac{1}{2}} + h^-_{j,k+\frac{1}{2}}\right) \tag{3.3.27}$$

for the configuration considered in Figure 3.3 (b).

We now subtract $B_{j,k}$ from both sides of (3.3.25) and use (3.3.26) and (3.3.27)

to rewrite (3.3.25) as follows:

$$
\begin{aligned}
\overline{h}_{j,k}^{n+1} = &-\lambda_{j,k}^n a_{j+\frac{1}{2},k}^- \cdot \frac{a_{j+\frac{1}{2},k}^+ - u_{j+\frac{1}{2},k}^+}{a_{j+\frac{1}{2},k}^+ - a_{j+\frac{1}{2},k}^-} \cdot h_{j+\frac{1}{2},k}^+ \\
&+ \left[\frac{1}{4} - \lambda_{j,k}^n a_{j+\frac{1}{2},k}^+ \cdot \frac{u_{j+\frac{1}{2},k}^- - a_{j+\frac{1}{2},k}^-}{a_{j+\frac{1}{2},k}^+ - a_{j+\frac{1}{2},k}^-}\right] h_{j+\frac{1}{2},k}^- \\
&+ \frac{\lambda_{j,k}^n a_{j-\frac{1}{2},k-\frac{1}{4}}^+}{2} \cdot \frac{u_{j-\frac{1}{2},k-\frac{1}{4}}^- - a_{j-\frac{1}{2},k-\frac{1}{4}}^-}{a_{j-\frac{1}{2},k-\frac{1}{4}}^+ - a_{j-\frac{1}{2},k-\frac{1}{4}}^-} \cdot h_{j-\frac{1}{2},k-\frac{1}{4}}^+ \\
&+ \frac{1}{2}\left[\frac{1}{4} - \lambda_{j,k}^n a_{j-\frac{1}{2},k-\frac{1}{4}}^- \cdot \frac{a_{j-\frac{1}{2},k-\frac{1}{4}}^+ - u_{j-\frac{1}{2},k-\frac{1}{4}}^+}{a_{j-\frac{1}{2},k-\frac{1}{4}}^+ - a_{j-\frac{1}{2},k-\frac{1}{4}}^-}\right] h_{j-\frac{1}{2},k-\frac{1}{4}}^+ \\
&+ \frac{\lambda_{j,k}^n a_{j-\frac{1}{2},k+\frac{1}{4}}^+}{2} \cdot \frac{u_{j-\frac{1}{2},k+\frac{1}{4}}^- - a_{j-\frac{1}{2},k+\frac{1}{4}}^-}{a_{j-\frac{1}{2},k+\frac{1}{4}}^+ - a_{j-\frac{1}{2},k+\frac{1}{4}}^-} \cdot h_{j-\frac{1}{2},k+\frac{1}{4}}^+ \\
&+ \frac{1}{2}\left[\frac{1}{4} - \lambda_{j,k}^n a_{j-\frac{1}{2},k+\frac{1}{4}}^- \cdot \frac{a_{j-\frac{1}{2},k+\frac{1}{4}}^+ - u_{j-\frac{1}{2},k+\frac{1}{4}}^+}{a_{j-\frac{1}{2},k+\frac{1}{4}}^+ - a_{j-\frac{1}{2},k+\frac{1}{4}}^-}\right] h_{j-\frac{1}{2},k+\frac{1}{4}}^+ \\
&- \mu_{j,k}^n b_{j,k+\frac{1}{2}}^- \cdot \frac{b_{j,k+\frac{1}{2}}^+ - v_{j,k+\frac{1}{2}}^+}{b_{j,k+\frac{1}{2}}^+ - b_{j,k+\frac{1}{2}}^-} \cdot h_{j,k+\frac{1}{2}}^+ \\
&+ \left[\frac{1}{4} - \mu_{j,k}^n b_{j,k+\frac{1}{2}}^+ \cdot \frac{v_{j,k+\frac{1}{2}}^- - b_{j,k+\frac{1}{2}}^-}{b_{j,k+\frac{1}{2}}^+ - b_{j,k+\frac{1}{2}}^-}\right] h_{j,k+\frac{1}{2}}^- \\
&+ \mu_{j,k}^n b_{j,k-\frac{1}{2}}^+ \cdot \frac{v_{j,k-\frac{1}{2}}^- - b_{j,k-\frac{1}{2}}^-}{b_{j,k-\frac{1}{2}}^+ - b_{j,k-\frac{1}{2}}^-} \cdot h_{j,k-\frac{1}{2}}^- \\
&+ \left[\frac{1}{4} + \mu_{j,k}^n b_{j,k-\frac{1}{2}}^- \cdot \frac{b_{j,k-\frac{1}{2}}^+ - v_{j,k-\frac{1}{2}}^+}{b_{j,k-\frac{1}{2}}^+ - b_{j,k-\frac{1}{2}}^-}\right] h_{j,k-\frac{1}{2}}^+ .
\end{aligned}
$$

This shows that the cell averages of h at the new time level can be written as a linear combination of the reconstructed nonnegative point values of h. Therefore, $\overline{h}_{j,k}^{n+1} \geq 0$ provided all of the coefficients in this linear combination are nonnegative, which is, using the definition of the local speeds of propagation in (3.3.19), true provided the following CFL-type condition are satisfied:

$\Delta t \leq$

$$\frac{1}{4}\min\left[\min_{j,k}\left\{\frac{\Delta x_{j,k}}{\max\limits_{(\alpha,\beta)}\left[\max\left\{a^+_{\alpha,\beta},-a^-_{\alpha,\beta}\right\}\right]}\right\},\ \min_{j,k}\left\{\frac{\Delta y_{j,k}}{\max\limits_{(\gamma,\delta)}\left[\max\left\{b^+_{\gamma,\delta},-b^-_{\gamma,\delta}\right\}\right]}\right\}\right].$$

where, as before,

$$(\alpha,\beta)\in\left\{(j-\frac{1}{2},k-\frac{1}{4}),(j-\frac{1}{2},k+\frac{1}{4}),(j+\frac{1}{2},k)\right\}$$

and

$$(\gamma,\delta)\in\left\{(j,k-\frac{1}{2}),(j,k+\frac{1}{2})\right\}$$

in the configuration considered in Figure 3.3 (b).

It should be observed that the above positivity preserving proof is valid not only for the forward Euler time discretization, but for any strong stability preserving (SSP) ODE solver (see, e.g., [30, 31]) as well. In all of our numerical experiments, we have used the three-stage third-order SSP Runge-Kutta solver.

3.3.8 Quadtree grid adaptivity

After evolving the solution to the new time level $t=t^{n+1}$ the quadtree grid should be adapted (locally either refined or coarsened) to the new solution structure. To this end, we first compute the slopes $\{(w_x)^{n+1}_{j,k}\}$ and $\{(w_y)^{n+1}_{j,k}\}$ on the old grid (which we denote by $\{C^{\rm old}_{j,k}\}$) according to §3.3.3 and then select the centers of those cells $C^{\rm old}_{j,k}$, at which either

$$(w_x)^{n+1}_{j,k}\ge C_{\rm seed}\quad\text{or}\quad(w_y)^{n+1}_{j,k}\ge C_{\rm seed},\tag{3.3.28}$$

to be the seeding points needed to generate the new grid, which we denote by $\{C^{\rm new}_{j,k}\}$. In (3.3.28), $C_{\rm seed}$ is a constant that depends on the problem at hand, that is, on such factors as the Froude number, bottom topography function and/or boundary conditions.

When the mesh is locally refined or coarsened, the solution realized at the end of the evolution step in terms of the computed cell averages $\left\{\left(\overline{\boldsymbol{U}}^{n+1}_{j,k}\right)_{\rm old}\right\}$ over the grid $\{C^{\rm old}_{j,k}\}$, should be projected onto the new grid $\{C^{\rm new}_{j,k}\}$ in a conservative manner according to the following three possible cases.

Case 1: If $C^{\text{new}}_{j,k} = C^{\text{old}}_{j',k'}$ for some (j',k'), that is, if the cell $C^{\text{old}}_{j',k'}$ does not need to be refined/coarsened, then

$$\big(\overline{\boldsymbol{U}}^{n+1}_{j,k}\big)_{\text{new}} = \big(\overline{\boldsymbol{U}}^{n+1}_{j',k'}\big)_{\text{old}}.$$

Case 2: If $C^{\text{new}}_{j,k} \in \mathscr{C}^{\ell+p}$ is a "child" cell of $C^{\text{old}}_{j',k'} \in \mathscr{C}^{\ell}$ for some j', k' and $p>0$ (that is, if the cell $C^{\text{old}}_{j',k'}$ was refined and $C^{\text{new}}_{j,k} \subset C^{\text{old}}_{j',k'}$), then

$$\big(\overline{\boldsymbol{U}}^{n+1}_{j,k}\big)_{\text{new}} = \big(\overline{\boldsymbol{U}}^{n+1}_{j',k'}\big)_{\text{old}} + \big((\boldsymbol{U}_x)^{n+1}_{j',k'}\big)_{\text{old}}\left[x^{\text{new}}_j - x^{\text{old}}_{j'}\right] + \big((\boldsymbol{U}_y)^{n+1}_{j',k'}\big)_{\text{old}}\left[y^{\text{new}}_k - y^{\text{old}}_{k'}\right].$$

Case 3: If $C^{\text{new}}_{j,k} \in \mathscr{C}^{\ell-p}$ is a "parent" cell of $C^{\text{old}}_{j',k'} \in \mathscr{C}^{\ell}$ for some j', k' and $p>0$ (that is, if the cell $C^{\text{old}}_{j',k'}$ was coarsened and $C^{\text{new}}_{j,k} \supset C^{\text{old}}_{j',k'}$), then

$$\big(\overline{\boldsymbol{U}}^{n+1}_{j,k}\big)_{\text{new}} = \frac{1}{4^p}\sum_{j'',k'':\,C^{\text{old}}_{j'',k''}\subset C^{\text{new}}_{j,k}}\sum \big(\overline{\boldsymbol{U}}^{n+1}_{j'',k''}\big)_{\text{old}}.$$

3.4 Numerical experiments

In this section, we present six numerical examples in which the central-upwind quadtree scheme is tested. In all of the examples (except for Example 5), we take $g=1$ and obtain the point values of B at the vertices of $C_{j,k}$ using the bottom topography function with $\ell := 5$ (§3.3.2).

3.4.1 Example 1. Accuracy test

In this benchmark, the accuracy of the proposed scheme is tested. We set the computational domain $[0,2]\times[0,1]$ with a zero-order extrapolation at all of the boundaries. The following initial data and the bottom topography function are imposed:

$$w(x,y,0)\equiv 1, \qquad u(x,y,0)\equiv 0.3, \qquad v(x,y,0)\equiv 0,$$

$$B(x,y) = 0.5e^{-25(x-1)^2-50(y-0.5)^2}.$$

We generate a structured Cartesian grid $[512\times 256]$ for the reference solution. The solution converges to a steady state solution by $t=0.07$. The L^1- and L^∞-errors for

$m = 5, 6, 7$, and 8 for $C_{\text{seed}} = 0.0005$ are presented in Table 3.1. The obtained errors are similar to the ones reported in [15, 46, 85]. The steady state solution computed with $m = 7$ and the corresponding quadtree grid are shown in Figure 3.4.

Table 3.1: Example 1: L^1- and L^∞- errors and numerical orders of accuracy.

Quadtree level	L^1-error	Order	L^∞-error	Order
$m = 5$	$8.97e-04$	–	$5.14e-03$	–
$m = 6$	$4.35e-04$	1.05	$3.22e-03$	0.67
$m = 7$	$2.80e-04$	1.68	$2.90e-03$	0.83
$m = 8$	$2.32e-04$	1.95	$2.18e-03$	1.24

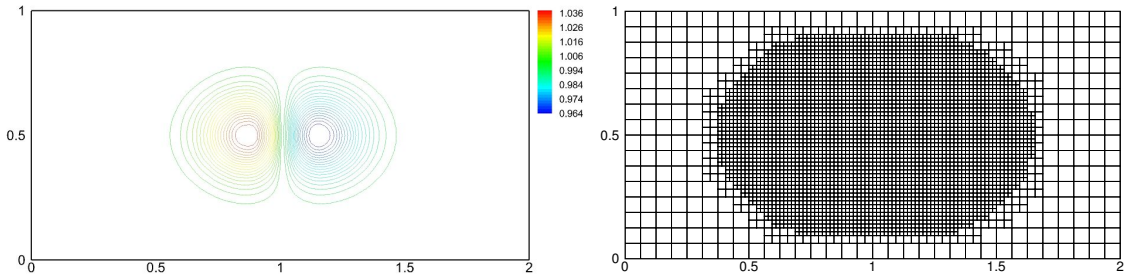

Figure 3.4: Example 1: Computed water surface $w(x, y, 0.07)$ for $m = 7$ (left) and its corresponding quadtree grid (right).

3.4.2 Example 2. Circular dam break

In this example, we demonstrate the ability of the proposed central-upwind quadtree scheme to preserve the positivity of the water surface and to maintain symmetry. A circular water column, where $w = 1$, collapses on a horizontal plane (similar examples were considered in [4, 61, 77, 75]), namely,

$$w(x, y, 0) = \begin{cases} 1, & (x-1)^2 + (y-1)^2 < 0.25, \\ 10^{-16}, & \text{otherwise}, \end{cases} \qquad u(x, y, 0) = v(x, y, 0) \equiv 0.$$

We take the computational domain $[0, 2] \times [0, 2]$ and impose zero-order extrapolated boundary conditions at its boundary. In this example, we take $m = 8$ and $m = 9$ refinement levels of the quadtree grid and set $C_{\text{seed}} = 0.1$ in (3.3.28). The initial quadtree grids are shown in Figure 3.5.

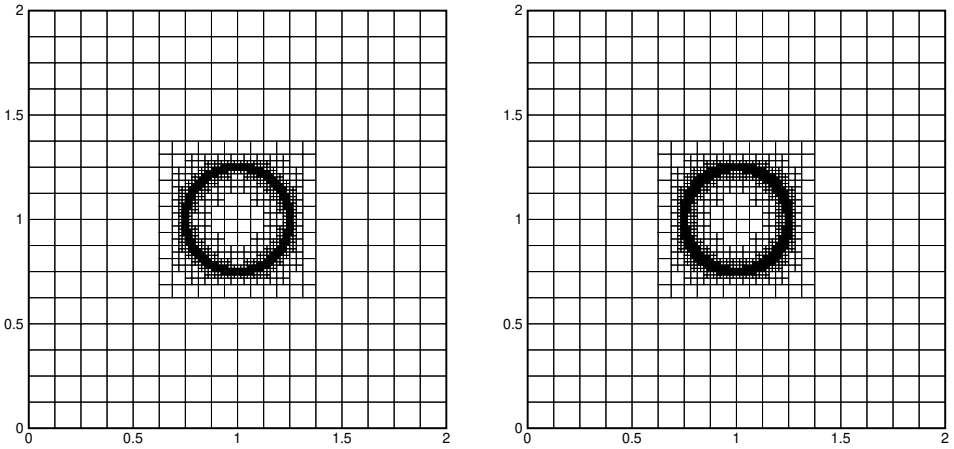

Figure 3.5: Example 2: Initial quadtree grids for $m = 8$ (left) and $m = 9$ (right).

We compute the solution until the final time $t = 0.2$ and plot the obtained water surface contours in Figure 3.6. As one can see, the central-upwind quadtree scheme maintains symmetry and preserves positivity. By changing the refinement level from $m = 8$ to $m = 9$, the computational cost increases (for $m = 8$, the quadtree grid starts with 1852 cells and ends with 12556 cells, whereas for $m = 9$, the grid starts with 3616 cells and ends with 56272 cells), but the results obtained with $m = 9$ are clearly sharper and more accurate.

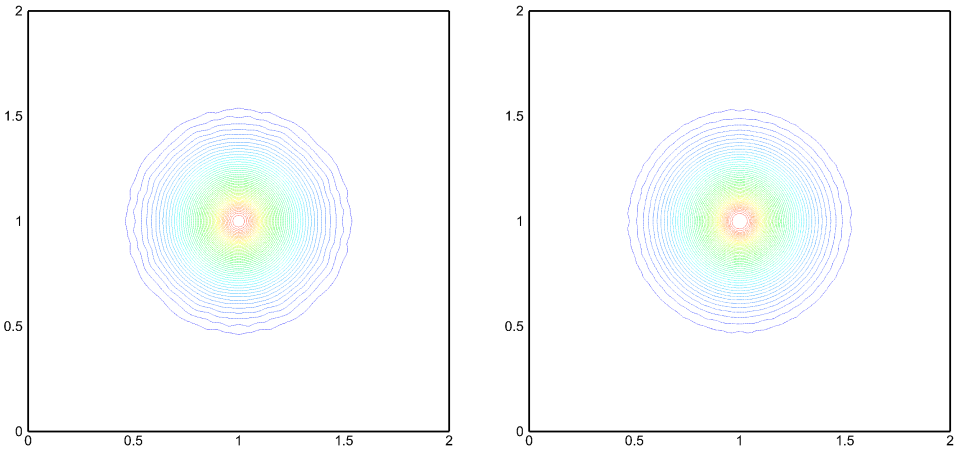

Figure 3.6: Example 2: Computed water surface $w(x, y, 0.2)$ for $m = 8$ (left) and $m = 9$ (right).

3.4.3 Example 3. Small perturbations of a stationary steady state solution

This numerical example is based on the benchmark, which was proposed in [55] to test the ability of studied schemes to accurately capture small perturbations of a steady state solution (similar examples were considered in, e.g., [15, 16, 43, 63]). The computational domain is $[0,2]\times[0,1]$, the initial conditions are

$$w(x,y,0)=\begin{cases}1.01, & 0.05<x<0.15,\\ 1, & \text{otherwise},\end{cases}\qquad u(x,y,0)=v(x,y,0)\equiv 0,$$

and the bottom topography is given by

$$B(x,y)=0.8e^{-5(x-0.9)^2-50(y-0.5)^2}.$$

A solid wall boundary condition is used at the top and bottom boundaries and zero-order extrapolation is implemented at the left and right ones. We first consider a very small value $\varepsilon=10^{-14}$ to verify the well-balanced property of the proposed quadtree scheme. The solution is solved with a coarse quadtree grid for $m=5$. In Figure 3.7, we plot $\max\limits_{x,y}(w-1)$ as a function of time until $t=0.6$. As one can see, the proposed scheme is stable and the fluxes and source terms balance each other.

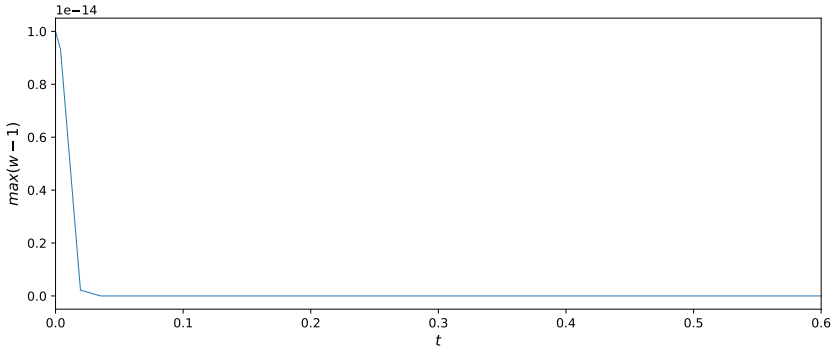

Figure 3.7: Example 3: Computed $\max\limits_{x,y} w(x,y,t)$ as a function of t for $m=5$.

We then take $\varepsilon=0.01$ and $m=8$ refinement levels of the quadtree grid and set small $C_{\text{seed}}=0.02$ in (3.3.28) in order to accurately resolve small features of the

computed solution.

We compute the solution until the final time $t = 1.8$ and plot the snapshots of w at times $t = 0.6$, 0.9, 1.2, 1.5 and 1.8 in Figure 3.8 (left). The quadtree grid starts with 1970 cells and reaches a maximum number of 7268 cells during the time evolution. Figure 3.8 (left) clearly demonstrate that the proposed well-balanced central-upwind quadtree scheme accurately captures a small perturbation of the "lake-at-rest" steady state and that the symmetry of the solution is preserved. The ability of the scheme to refine grids where local gradients are sharp can be seen in Figure 3.8 (right), where the quadtree grids at the same times $t = 0.6$, 0.9, 1.2, 1.5 and 1.8 are presented.

We also solve this initial-boundary value problem using a non-well-balanced central-upwind quadtree scheme to stress the importance of the well-balanced property. In order to design a non-well-balanced scheme, we replace the well-balanced numerical source terms $\overline{S}^{(2)}_{j,k}$ and $\overline{S}^{(3)}_{j,k}$ given by (3.3.24) with the source terms obtained by a straightforward midpoint rule quadrature. For the configuration considered in Figure 3.3 (b), the non-well-balanced source term approximations read as

$$\overline{S}^{(2)}_{j,k} = -\frac{g(\overline{w}_{j,k} - B_{j,k})}{\Delta x_{j,k}} \left[\frac{B_{j+\frac{1}{2},k+\frac{1}{2}} + B_{j+\frac{1}{2},k-\frac{1}{2}}}{2} - \frac{B_{j-\frac{1}{2},k+\frac{1}{2}} + B_{j-\frac{1}{2},k-\frac{1}{2}}}{2} \right],$$

$$\overline{S}^{(3)}_{j,k} = -\frac{g(\overline{w}_{j,k} - B_{j,k})}{\Delta x_{j,k}} \left[\frac{B_{j+\frac{1}{2},k+\frac{1}{2}} + B_{j+\frac{1}{2},k-\frac{1}{2}}}{2} - \frac{B_{j-\frac{1}{2},k+\frac{1}{2}} + B_{j-\frac{1}{2},k-\frac{1}{2}}}{2} \right].$$

Figure 3.9 shows the the snapshots of w at times $t = 0.6$, 0.9, 1.2, 1.5 and 1.8 and the corresponding quadtree grids obtained using the non-well-balanced computations. As one can see, the use of non-well-balanced numerical source term leads to the appearance of not small "parasitic" waves. Even though these waves are not as large as in the non-well-balanced results presented in, e.g., [15] or [63], the unphysical oscillations caused by the non-well-balanced discretization of the source term are attenuated by adding more seeding points as the quadtree grid reaches a maximum number of 8900 cells during the time evolution. This demonstrates the importance of the well-balanced property, which eventually reduces the computational cost.

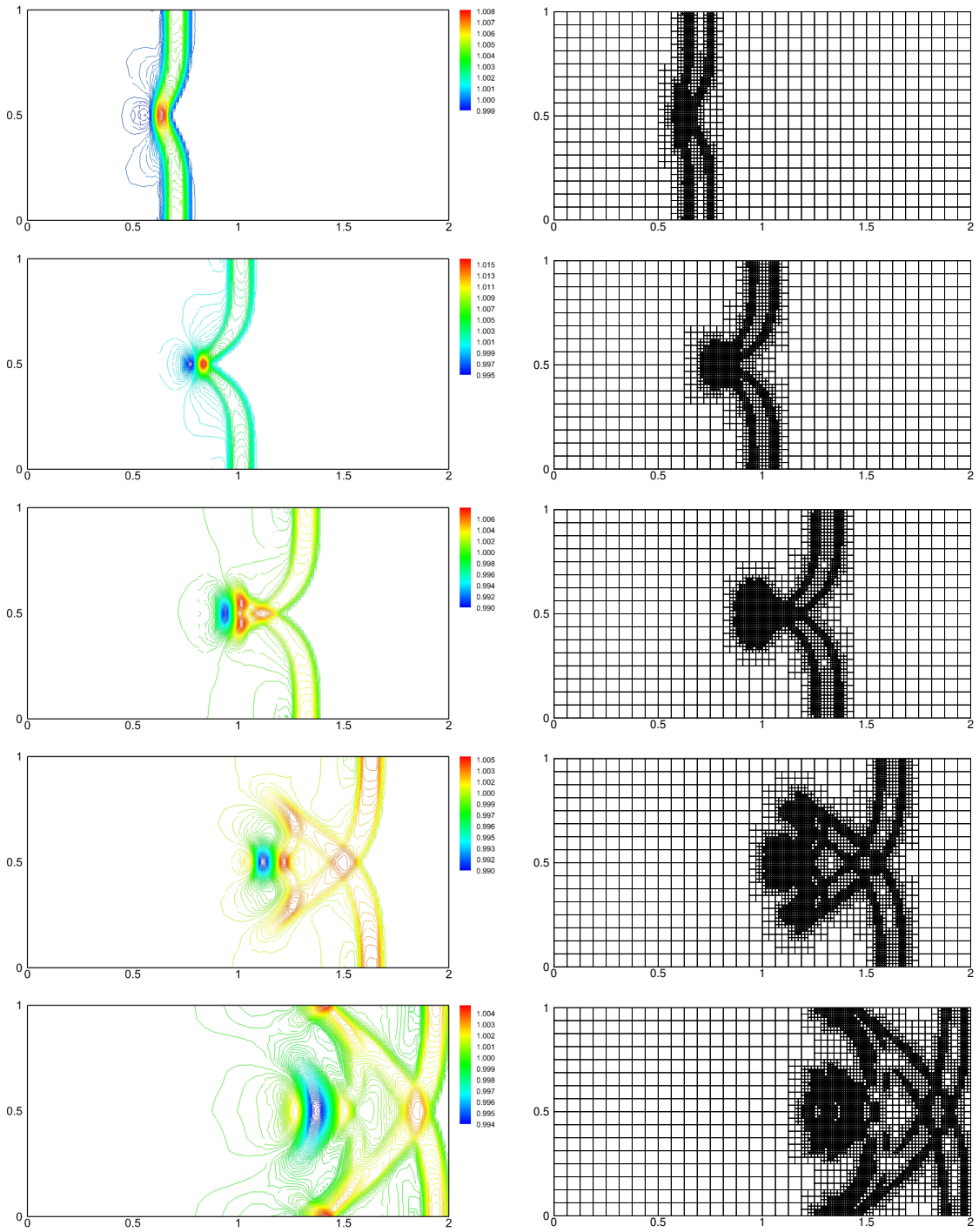

Figure 3.8: Example 3: Computed water surface $w(x, y, t)$ (left column) and the corresponding quadtree grids (right column) for $t = 0.6$, 0.9, 1.2, 1.5 and 1.8 (from top to down) obtained using the well-balanced central-upwind quadtree scheme.

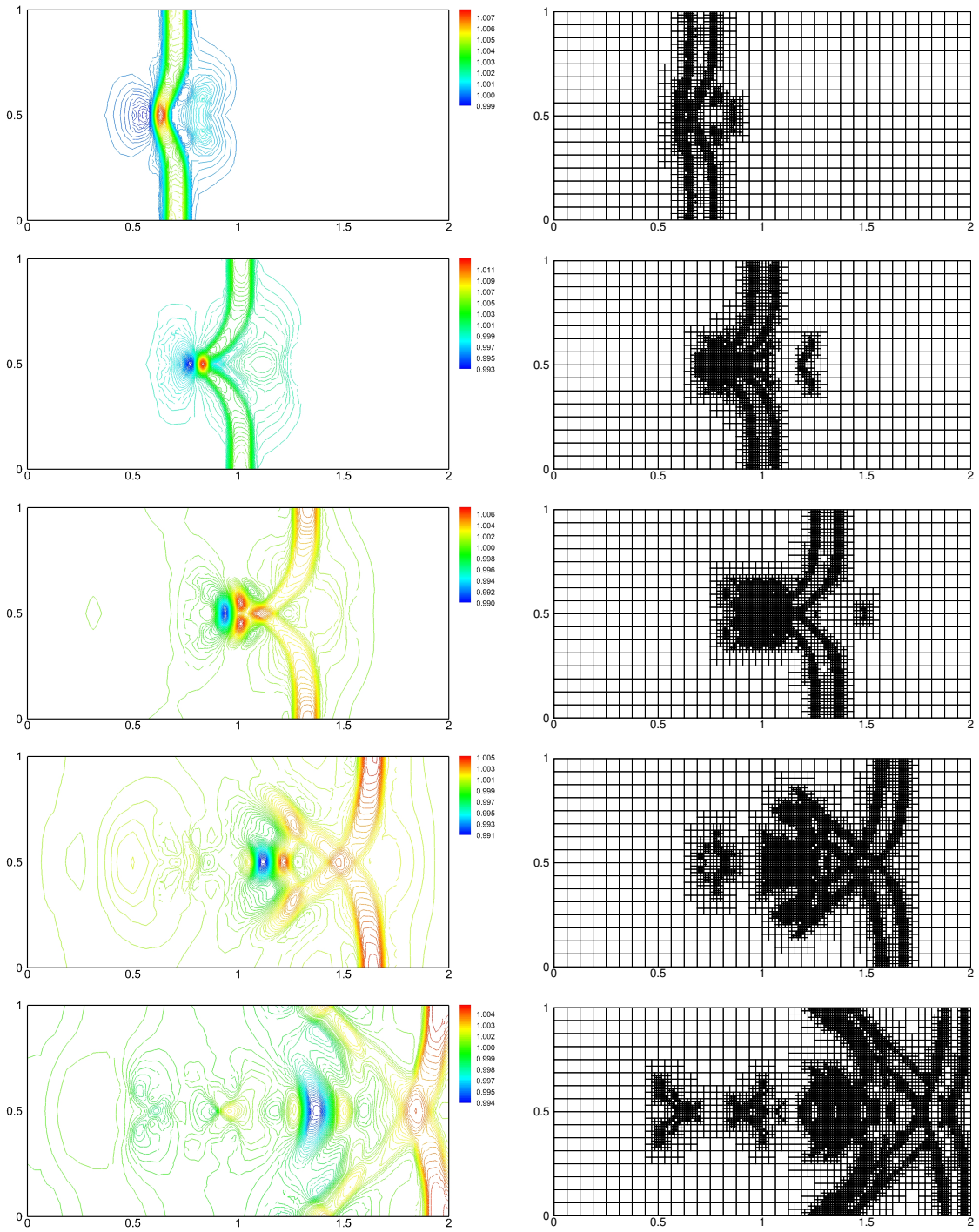

Figure 3.9: Example 3: Computed water surface $w(x, y, t)$ (left column) and the corresponding quadtree grids (right column) for $t = 0.6$, 0.9, 1.2, 1.5 and 1.8 (from top to down) obtained using the non-well-balanced central-upwind quadtree scheme.

3.4.4 Example 4. Small perturbations over a flat plateau

In this example, which is similar to the examples considered in [15, 85], we study small perturbations over a submerged flat plateau. The computational domain is $[0,1]\times[0,1]$. A solid wall boundary condition is used at the top and bottom boundaries and zero-order extrapolation is implemented at the left and right ones. The bottom topography function is given by

$$B(x,y)=\begin{cases}1-2\varepsilon, & r\le 0.1,\\ 10(1-2\varepsilon)(0.2-r), & 0.1\le r\le 0.2,\\ 0, & \text{otherwise},\end{cases}$$

where $\varepsilon=10^{-4}$ and $r=\sqrt{(x-0.5)^2+(y-0.5)^2}$. The following initial data are imposed:

$$w(x,y,0)=\begin{cases}1+\varepsilon, & 0.1\le x\le 0.2,\\ 1, & \text{otherwise},\end{cases}\qquad u(x,y,0)=v(x,y,0)\equiv 0.$$

We compute both well-balanced and non-well-balanced solutions with $m=8$ and $C_{\text{seed}}=0.0002$. The obtained w (left column) and the corresponding quadtree grids (right column) at $t=0.2, 0.35, 0.5$, and 0.65 are shown in Figures 3.10 and 3.11. We note that the number of cells in the well-balanced computation varies from 3712 to 13384, while in the non-well-balanced one it goes up to a much larger maximum of 34126 cells. However, this level of refinement is apparently not enough to suppress the non-physical parasitic waves, which propagate all over the computational domain; see Figure 3.11. On the contrary, the well-balanced solution is oscillation-free as one can clearly see in Figure 3.10.

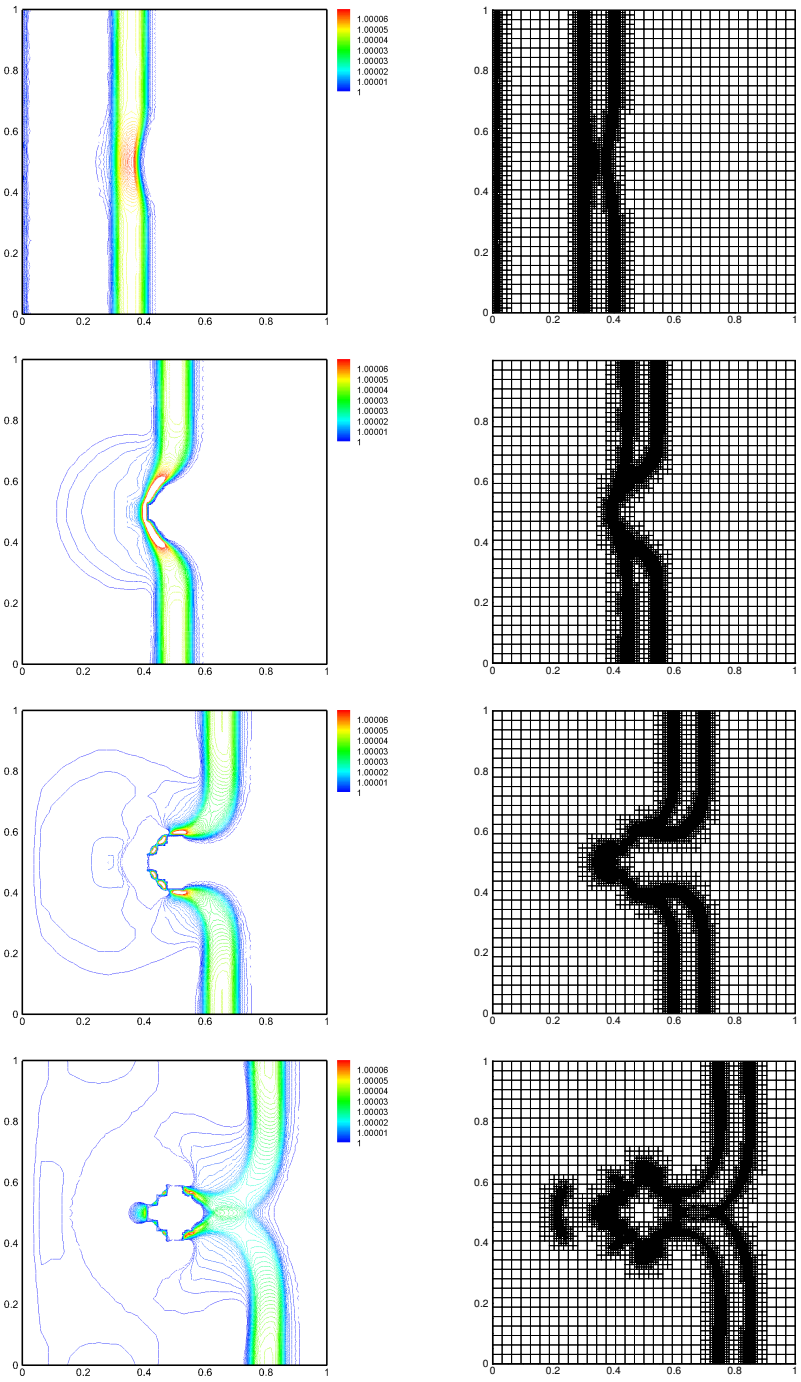

Figure 3.10: Example 4: Computed water surface $w(x, y, t)$ (left column) and the corresponding quadtree grids (right column) for $t = 0.2$, 0.35, 0.5, and 0.65 (from top to down) obtained using the well-balanced central-upwind quadtree scheme.

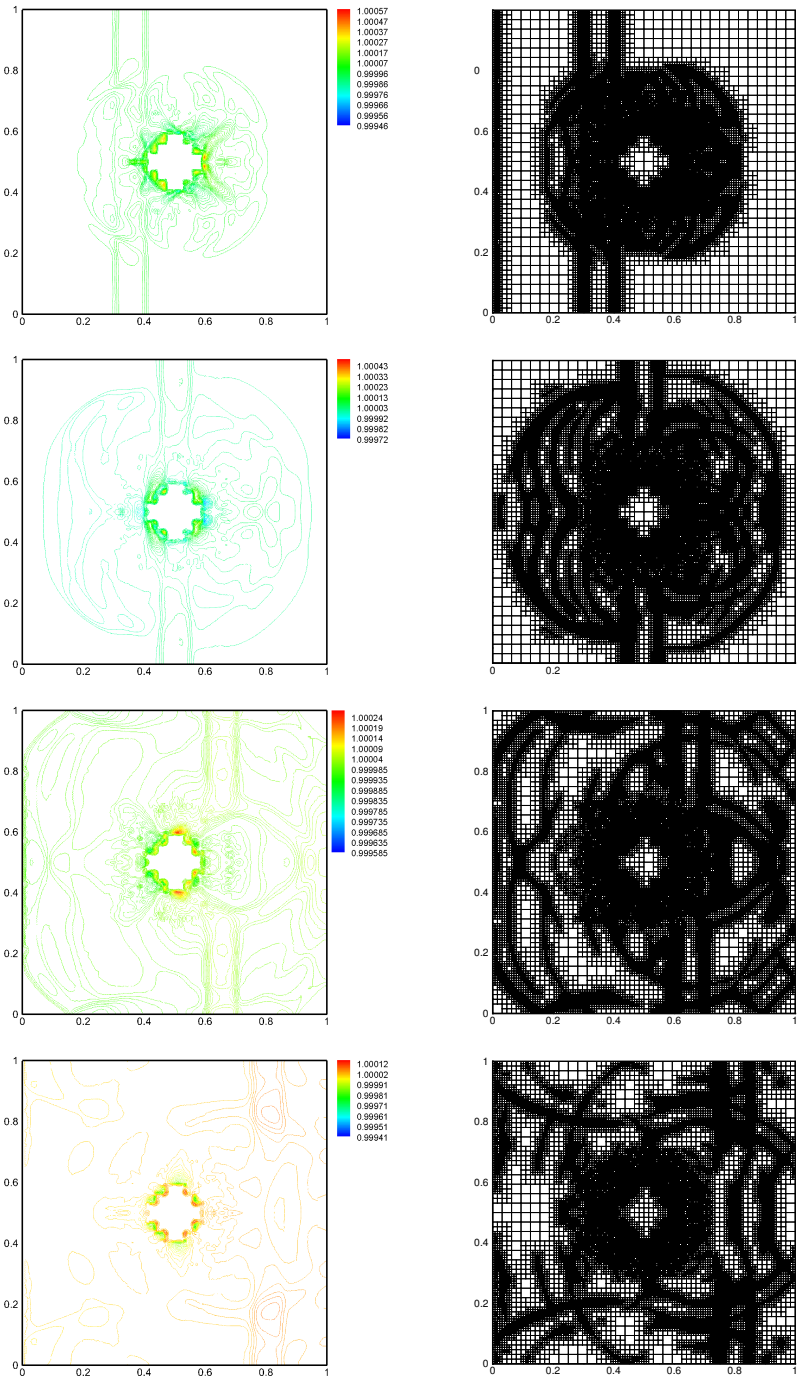

Figure 3.11: Example 4: Computed water surface $w(x, y, t)$ (left column) and the corresponding quadtree grids (right column) for $t = 0.2$, 0.35, 0.5, and 0.65 (from top to down) obtained using the non-well-balanced central-upwind quadtree scheme.

3.4.5 Example 5. Cylindrical dam break over a step

In this example, we demonstrate the capability of the proposed scheme to solve problems with discontinuous bottom topography. From [22], we consider the following initial condition

$$\boldsymbol{Q}(x,y,0) = \begin{cases} \boldsymbol{Q}_i, & r \le 1, \\ \boldsymbol{Q}_o, & r > 1, \end{cases}$$

where $r^2 = (x-2)^2 + (y-2)^2$ and $\boldsymbol{Q} = (u, v, h, B)$. The computational domain is $[0,4] \times [0,4]$. We choose the inner and the outer states to be $\boldsymbol{Q}_i = (0, 0, 1, -0.2)$ and $\boldsymbol{Q}_o = (0, 0, 0.5, 0)$ respectively. We first, take $g = 9.8$ and obtain the point values of B at the vertices of $C_{j,k}$ using the bottom topography function with $\ell = 6$ (§3.3.2). The problem is solved with $C_{seed} = 0.1$ and $m = 8$ until $t = 0.2$. Figure 3.12 shows the computed solution of w at $t = 0.05$, 0.1, 0.15, and 0.2 and their corresponding quadtree grids. The solution starts with a minimum of 6172 cells and reaches a maximum of 12508 cells. As one can see, the proposed scheme is able to solve such a problem with discontinuous bottom topography.

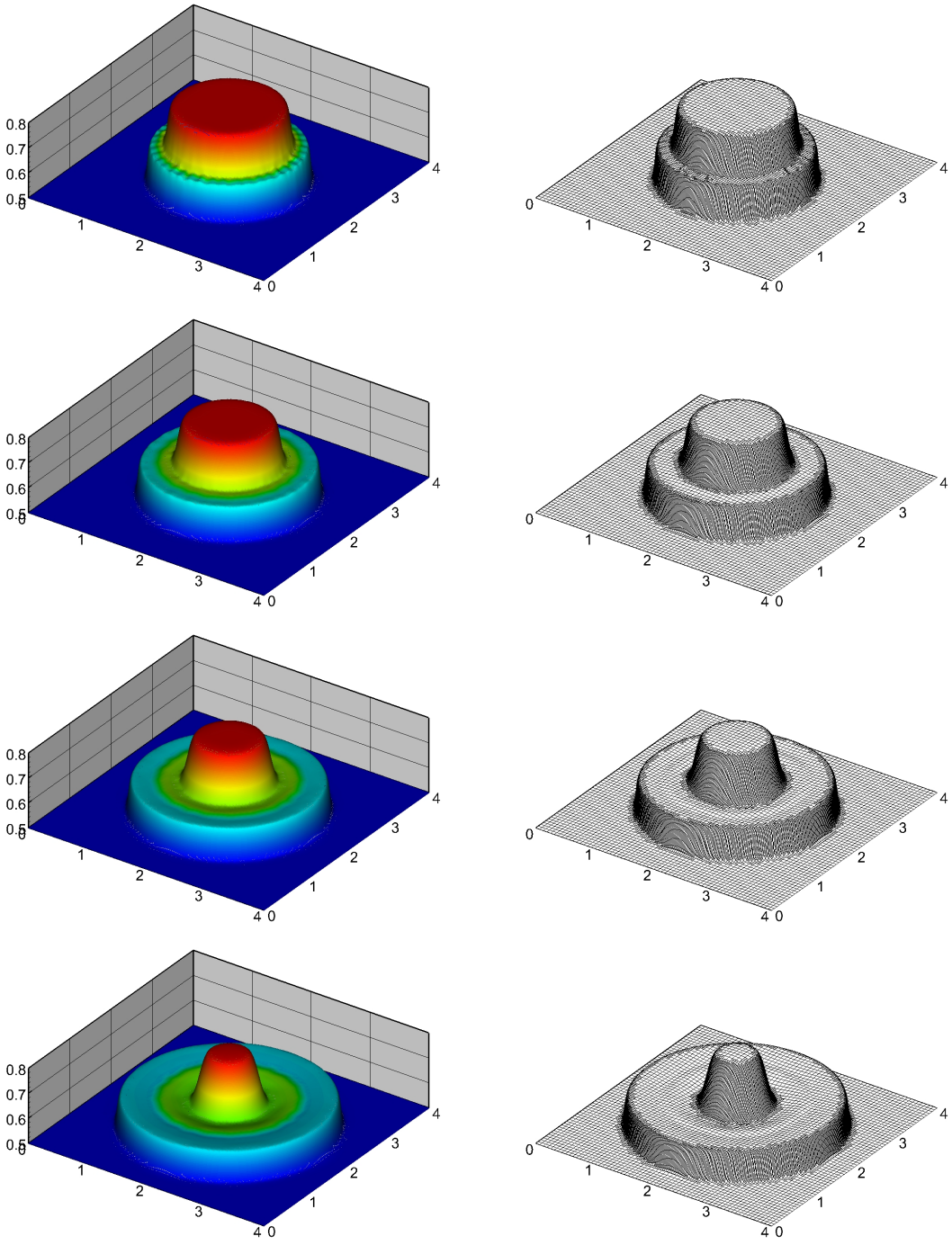

Figure 3.12: Example 5: Computed water surface $w(x, y, t)$ (left column) and the corresponding quadtree grids (right column) for $t = 0.05$, 0.1, 0.15, and 0.2 (from top to down) obtained using the well-balanced central-upwind quadtree scheme for $m = 8$.

3.4.6 Example 6. Sudden contraction

The last example is a modification of the benchmark in [37]; also see [16, 15]. The purpose of this example is twofold: to show the ability of the central-upwind quadtree scheme to capture shocks and sharp waves in supercritical flows and to demonstrate the positivity preserving property of the proposed scheme.

We consider an open channel with a sudden contraction. The geometry of the channel is established on its contraction, where

$$y_b(x) = \begin{cases} 0.5, & x \le 1, \\ 0.4, & \text{otherwise.} \end{cases}$$

The computational domain is $[0,3] \times [0.5 - y_b(x), 0.5 + y_b(x)]$. Solid wall boundary conditions are imposed at all of the boundaries except for the left (inflow boundary with $u(0,y,t) \equiv 2$) and right (zero-order extrapolation) ones. The following initial conditions are prescribed:

$$w(x,y,0) \equiv 1, \quad u(x,y,0) \equiv 2, \quad v(x,y,0) \equiv 0.$$

In this example, we take $m = 8$ and $m = 9$ refinement levels of the quadtree grid and set $C_{\text{seed}} = 2$ in (3.3.28). This value of C_{seed} is greater than the ones used in Examples 1 and 2 since this numerical experiment focuses on capturing sharp waves and thus choosing small values of C_{seed} would have increased the computational cost as the local gradients are relatively large in most parts of the computational domain.

The solution is computed twice: first, the flat bottom topography $B(x,y) \equiv 0$ is used in order to demonstrate the ability of the scheme to capture hydraulic jumps and sharp waves, and second, we use the bottom topography given by

$$B(x,y) = 0.95\left[e^{-10(x-1.9)^2-50(y-0.7)^2} + e^{-20(x-2.2)^2-50(y-0.3)^2}\right]$$

and shown in Figure 3.13 together with the initial quadtree grid for $m = 9$ (notice that the grid is refined near the boundaries at the contraction to improve accuracy). In the nonflat bottom topography case, the water at the top of the humps is quite shallow (that is why this is a good example to test the positivity preserving property) and the Froude number there is initially about 2.

We compute the solution until the final time $t = 2$ in order to simulate a transient flow state. We plot the snapshots of w at times $t = 0.5$, 1, 1.5 and 2 in Figures 3.14 and 3.15 for the flat and nonflat bottom topographies, respectively. As one can see, the proposed central-upwind quadtree scheme preserves positivity of the computed water depth and is able to capture hydraulic jumps. Increasing m from 8 to 9 clearly improves the accuracy and resolution of the hydraulic jumps. Finally, in Table 3.2, we present the minimum and maximum number of cells during the time evolution for different quadtree levels and topographies.

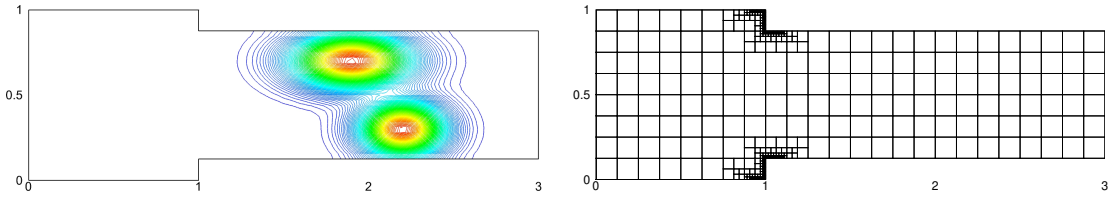

Figure 3.13: Example 6: Bottom topography (left) and initial quadtree grid with $m = 9$ (right).

Table 3.2: Example 6: Minimum and maximum number of cells for each of the four solutions.

Quadtree level	$m = 8$		$m = 9$	
	min	max	min	max
$B(x, y) \equiv 0$	298	3154	436	10954
$B(x, y) \neq 0$	298	5140	436	21340

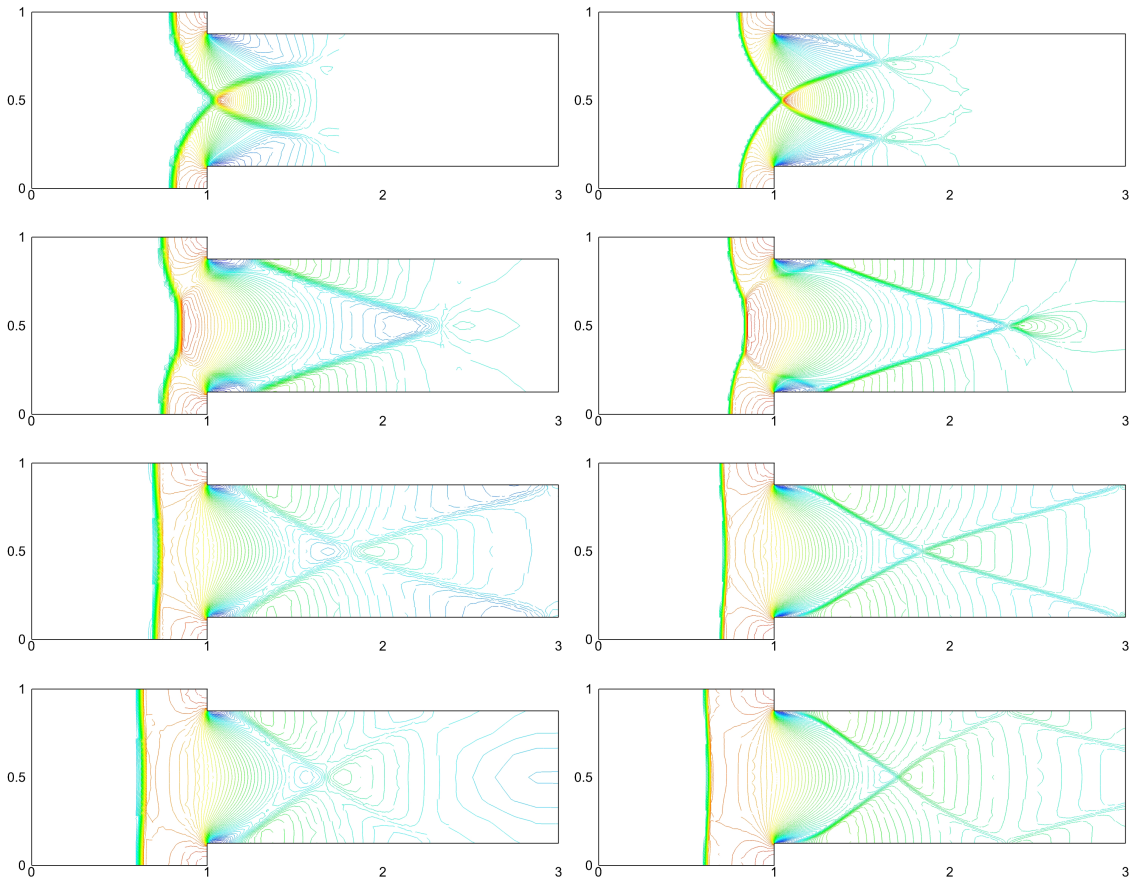

Figure 3.14: Example 6: Computed water surface $w(x, y, t)$ for $t = 0.5$, 1, 1.5 and 2 (from top to down) obtained using the flat bottom topography for $m = 8$ (left column) and $m = 9$ (right column).

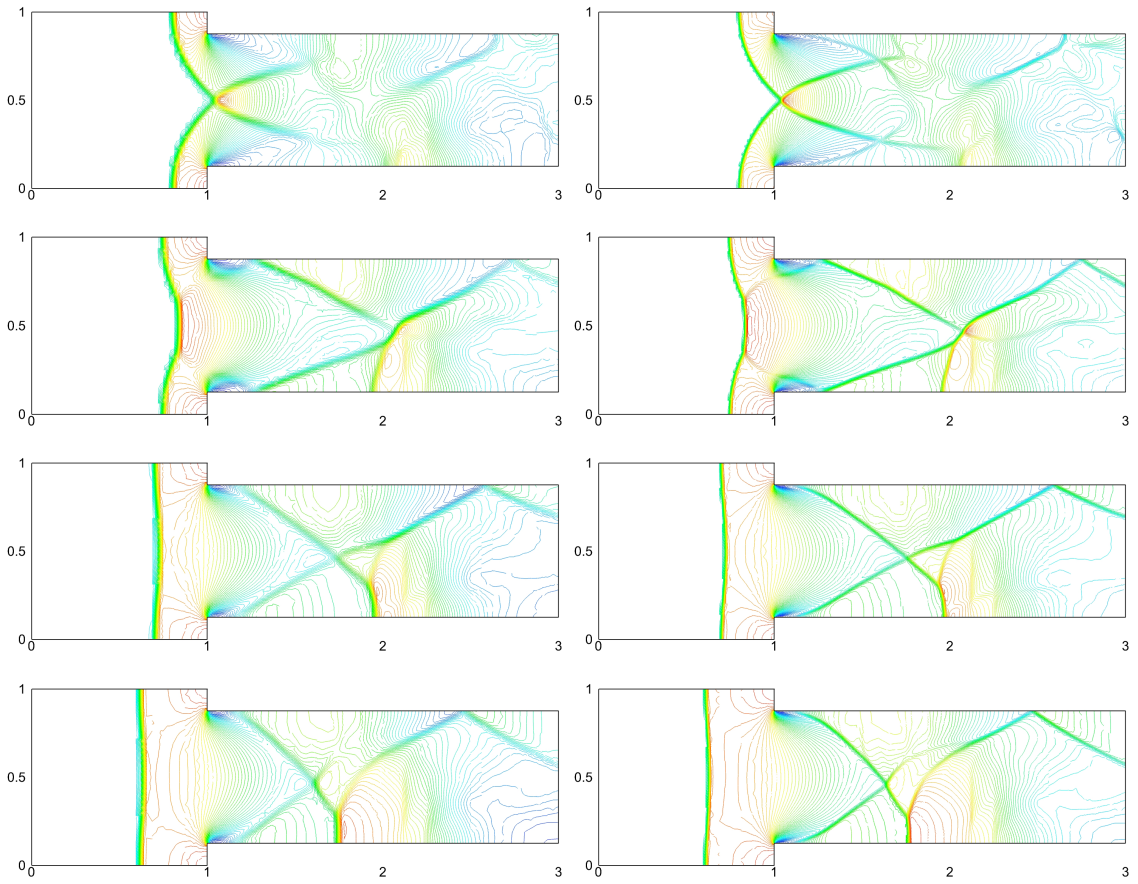

Figure 3.15: Example 6: Computed water surface $w(x, y, t)$ for $t = 0.5$, 1, 1.5 and 2 (from top to down) obtained using the nonflat bottom topography for $m = 8$ (left column) and $m = 9$ (right column).

Chapter 4

An adaptive well-balanced positivity preserving central-upwind scheme on quadtree grids for variable density shallow water equations [2]

4.1 Introduction

Quadtree grids are two-dimensional semi-structured Cartesian grids that are utilized in the field of computational hydrodynamics. The use of quadtree grids can be very accommodating in various problems. One of the advantages of quadtree grids over structured and unstructured grids is grid coarsening/refining. The accuracy is increased/maintained while the grid refines/coarsens wherever it is needed and thus, the computational cost is reduced. There are a number of studies on how to generate quadtree grids; see, e.g., [1, 14, 32, 69, 71, 80, 82].

Using quadtree grids has advantages; however, they are incapable of representing complex geometries adequately. In such situations, quadtree-cut-cell grids become useful; see, e.g., [2]. In this paper, we only focus on quadtree grids.

The main goal of this paper is to develop an adaptive well-balanced positivity preserving central-upwind scheme on quadtree grids for the coupled variable density

[2] M. A. Ghazizadeh and A. Mohammadian. An adaptive well-balanced positivity preserving central-upwind scheme on quadtree grids for variable density shallow water equations, *Numerische Mathematik*, under review, 2020.

Saint-Venant system of shallow water equations. The variable density SWE in 2-D can be written in terms of conservative variables w (water surface), hu and hv (the unit discharges), and $h\rho$:

$$\begin{cases} w_t + (hu)_x + (hv)_y = 0, \\ (hu)_t + \left(hu^2 + \dfrac{g}{2\rho_\circ} h^2\rho\right)_x + (huv)_y = -\dfrac{g}{\rho_\circ} h\rho B_x, \\ (hv)_t + (huv)_x + \left(hv^2 + \dfrac{g}{2\rho_\circ} h^2\rho\right)_y = -\dfrac{g}{\rho_\circ} h\rho B_y, \\ (h\rho)_t + (hu\rho)_x + (hv\rho)_y = 0, \end{cases} \tag{4.1.1}$$

where t is time, g is the gravitational constant, x and y are the directions in the 2-D Cartesian coordinate system, $u(x, y, t)$ and $v(x, y, t)$ are the water velocities in the x- and y-directions, respectively, $B(x, y)$ is the bottom topography, $h(x, y, t) = w(x, y, t) - B(x, y)$ is the water depth, ρ is the density, and $\rho_\circ$ is the reference density.

The system (4.1.1) admits "lake-at-rest" steady tate solutions,

$$\rho \equiv \text{Const}, \quad w \equiv \text{Const}, \quad B \equiv \text{Const}, \quad u = v \equiv 0, \tag{4.1.2}$$

which can be obtained from (4.1.1) [19]. The following quadtree scheme is capable of exactly preserving "lake-at-rest" steady states, which is called *well-balanced* property. Another important attribute of the following method is its ability to preserve non-negativity of h and ρ, which is called *positivity preserving* property (see [42] for an extensive review on these subjects).

A number of numerical schemes on quadtree grids for the SWE system have been introduced in recent years. For example, an adaptive well-balanced positivity preserving central-upwind high-order scheme on quadtree grids was proposed in [28]. In addition, a well-balanced scheme on quadtree-cut-cell grids was proposed in [2]. This scheme is based on the hydrostatic reconstruction from [4]. Furthermore, an adaptive second-order Roe-type scheme was proposed in [77]. An adaptive well-balanced Godunov-type scheme for the shallow water for the wet-dry over complex topography in [58] and an adaptive quadtree Roe-type scheme for a 2-D two-layer SWE in [52] were introduced, as well.

Besides the aforementioned numerical methods, several well-balanced positivity preserving schemes for the shallow water equations have been proposed in the past years; see, e.g., [3, 4, 5, 10, 11, 12, 15, 26, 43, 46, 62, 74, 85], but none of these methods has been extended to the coupled variable density SWE over quadtree grids.

In [38] the coupled variable density SWE was studied with a Godunov-type HLLC approximate Riemann solver. There are other studies that have been conducted on variable density SWE system and variable horizontal temperature SWE (which has mathematically similar properties) with different numerical schemes; see, e.g. [19, 35, 41, 54].

In this paper, we propose a central-upwind quadtree scheme which is based on the one from [28]. Central-upwind schemes are finite-volume methods that are Godunov-type Riemann-problem-solver-free [44, 45, 47, 48]. Central-upwind schemes were referred as "black-box" solvers for general multidimensional systems of hyperbolic systems of conservation laws and were extended to shallow water models [42]. The proposed scheme is the first well-balanced and positivity preserving central-upwind scheme for the variable density SWE over quadtree grids. This method is simple, efficient and robust.

The paper is organized as follows. In §4.2, we briefly describe a quadtree grid generation terminology. In §4.3, we construct a central-upwind quadtree scheme for the variable density SWE with the mentioned features and test it on four different numerical examples in §4.4.

4.2 Quadtree grids

Quadtree grids present a recursive spatial decomposition of the computational domain. For the sake of brevity we only mention the terminology on how to generate quadtree grids (see [28, 14, 32, 70]):

Seeding points: A set of points considering features of the problem, boundary conditions, flow characteristics, local gradients and governing equations.

Level of refinement: Level of quadtree, in which the size of the smallest cell is inversely proportional to the maximum level of m.

Regularized quadtree grid: In a regularized grid no cell can have both an adjacent neighbouring cell and a diagonally neighbouring cell with a refinement level difference greater than one (Figure 4.1). The proposed scheme is based on regularized quadtree grids to prevent complicated formulations and improve stability.

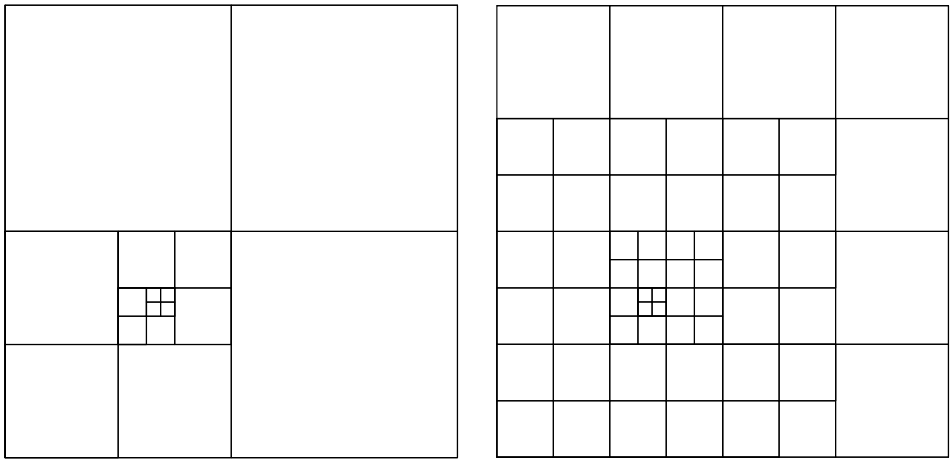

Figure 4.1: Examples of non-regularized (left) and regularized (right) quadtree grids.

4.3 Adaptive well-balanced semi-discrete central-upwind scheme

System (4.1.1) can be written in the following vector form:

$$\boldsymbol{U}_t + \boldsymbol{F}(\boldsymbol{U}, B)_x + \boldsymbol{G}(\boldsymbol{U}, B)_y = \boldsymbol{S}(\boldsymbol{U}, B), \tag{4.3.1}$$

where

$$\boldsymbol{U} := (w, hu, hv, h\rho)^\top,$$

and the fluxes and source term are:

$$\boldsymbol{F}(\boldsymbol{U}, B) = \left(hu, \frac{(hu)^2}{w-B} + \frac{g}{2\rho_\circ}\rho\,(w-B)^2, \frac{(hu)(hv)}{w-B}, hu\rho\right)^\top, \tag{4.3.2}$$

$$\boldsymbol{G}(\boldsymbol{U}, B) = \left(hv, \frac{(hu)(hv)}{w-B}, \frac{(hv)^2}{w-B} + \frac{g}{2\rho_\circ}\rho\,(w-B)^2, hv\rho\right)^\top, \tag{4.3.3}$$

$$\boldsymbol{S}(\boldsymbol{U},B)=\left(0,-\frac{g}{\rho_\circ}\rho\,(w-B)B_x,-\frac{g}{\rho_\circ}\rho\,(w-B)B_y,0\right)^\top. \tag{4.3.4}$$

In what follows, an adaptive well-balanced semi-discrete central-upwind scheme for (4.3.1) is presented. The central-upwind quadtree scheme will be designed according to the algorithm in [28]:

4.3.1 Finite-volume semi-discretization over quadtree grids

Let us represent each cell $C_{j,k}$ of size $\Delta x_{j,k}\times\Delta y_{j,k}$ centered at $(x_{j,k},y_{j,k})$ as a finite volume quadtree cell in the proposed scheme. The approximate averages of the cell read as:

$$\overline{\boldsymbol{U}}_{j,k}(t)\approx\frac{1}{\Delta x_{j,k}\Delta y_{j,k}}\int\limits_{x_{j-\frac{1}{2}}}^{x_{j+\frac{1}{2}}}\int\limits_{y_{k-\frac{1}{2}}}^{y_{k+\frac{1}{2}}}\boldsymbol{U}(x,y,t)\,\mathrm{d}y\,\mathrm{d}x, \tag{4.3.5}$$

where $x_{j\pm\frac{1}{2}}:=x_{j,k}\pm\Delta x_{j,k}/2$ and $y_{k\pm\frac{1}{2}}:=y_{j,k}\pm\Delta y_{j,k}/2$.

Let us consider only the right and left neighbouring cells of $C_{j,k}$. Eight different possible permutations of neighbouring cells in the x-direction exist [28]. This can also be extended for the neighbouring cells on the top and bottom in the y-direction. For the sake of brevity, the quadtree scheme is only presented for the permutation in Figure 4.2 (which is one of the 8+8 possible configurations in regularized quadtree grids). Note that the following scheme can be implemented to the other possible configurations.

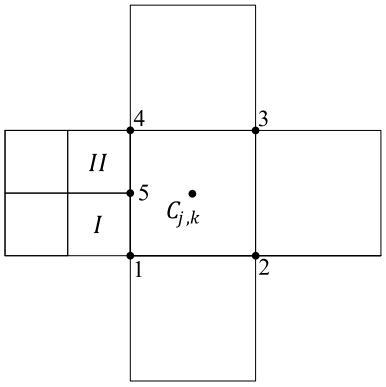

Figure 4.2: A possible configuration of neighbouring cells of $C_{j,k}$ in the x-direction in regularized quadtree grids.

The left-neighbouring cells of $C_{j,k}$ are denoted by I and II which are centered at $(x_{j,k} - 3\Delta x_{j,k}/4, y_{j,k} \pm \Delta y_{j,k}/4)$ with size of $\Delta x_{j,k}/2 \times \Delta y_{j,k}/2$.

The evolution of time-dependant cell averages $\overline{\boldsymbol{U}}_{j,k}$, which are obtained after the semi-discretization of the system (4.3.1)–(4.3.4), are computed by solving the following system of ODE:

$$\frac{\mathrm{d}}{\mathrm{d}t}\overline{\boldsymbol{U}}_{j,k} = -\frac{\boldsymbol{H}^x_{j+\frac{1}{2},k} - \dfrac{\boldsymbol{H}^x_{j-\frac{1}{2},k-\frac{1}{4}} + \boldsymbol{H}^x_{j-\frac{1}{2},k+\frac{1}{4}}}{2}}{\Delta x_{j,k}} - \frac{\boldsymbol{H}^y_{j,k+\frac{1}{2}} - \boldsymbol{H}^y_{j,k-\frac{1}{2}}}{\Delta y_{j,k}} + \overline{\boldsymbol{S}}_{j,k}. \quad (4.3.6)$$

In (4.3.6), $\boldsymbol{H}^x_{j+\frac{1}{2},k}$, $\boldsymbol{H}^x_{j-\frac{1}{2},k\pm\frac{1}{4}}$, $\boldsymbol{H}^y_{j,k+\frac{1}{2}}$ and $\boldsymbol{H}^y_{j,k-\frac{1}{2}}$ are the numerical fluxes, and $\overline{\boldsymbol{S}}_{j,k}$ is a cell average of the source term:

$$\overline{\boldsymbol{S}}_{j,k} \approx \frac{1}{\Delta x_{j,k}\Delta y_{j,k}} \int_{x_{j-\frac{1}{2}}}^{x_{j+\frac{1}{2}}} \int_{y_{k-\frac{1}{2}}}^{y_{k+\frac{1}{2}}} \boldsymbol{S}(\boldsymbol{U}, B)\,\mathrm{d}y\,\mathrm{d}x. \quad (4.3.7)$$

For the sake of brevity, in what follows, we omit all of the time-dependent indexed quantities in (4.3.6)–(4.3.7).

4.3.2 Piecewise bilinear reconstruction of B

Cells of different sizes $\Delta x \times \Delta y$, $\frac{\Delta x}{2} \times \frac{\Delta y}{2}, \ldots, \frac{\Delta x}{2^{m-1}} \times \frac{\Delta y}{2^{m-1}}$ exist in the quadtree grid. The set of cells of the corresponding size is indicated by $\mathscr{C}^{(\ell)}$, that is, $\mathscr{C}^{(\ell)} = \{C_{j,k} : |C_{j,k}| = \frac{\Delta x}{2^{\ell-1}} \times \frac{\Delta y}{2^{\ell-1}}\}$.

Based on [28], a continuous piecewise bilinear reconstruction of the continuous bottom topography $\widetilde{B}(x, y)$ is used according to the following algorithm.

Step 1. Set $\ell := 1$.

Step 2. Reconstruct bilinear pieces $\widetilde{B}$ for all (j, k) such that $C_{j,k} \in \mathscr{C}^{(\ell)}$.

Obtain the point values of B at the vertices of $C_{j,k}$. There are two possibilities if one of the places is on the edge of a larger neighbouring cell:

(i) the point value of B has already been calculated if this vertex coincides with a vertex of the neighbouring cell;

(ii) or the point value of B at this vertex is an average of the point values of B

at those two vertices of the neighbouring cell that lie on the same edge if this vertex is a midpoint of the edge of the neighbouring cell.

Otherwise, we continue and set

$$B_{j\pm\frac{1}{2},k\pm\frac{1}{2}} := \frac{1}{2}\Big(\max_{\xi^2+\eta^2=1} \lim_{\ell_x,\ell_y\to 0} B(x_{j\pm\frac{1}{2}} + \ell_x\xi, y_{k\pm\frac{1}{2}} + \ell_y\eta) + \min_{\xi^2+\eta^2=1} \lim_{\ell_x,\ell_y\to 0} B(x_{j\pm\frac{1}{2}} + \ell_x\xi, y_{k\pm\frac{1}{2}} + \ell_y\eta)\Big).$$

The following bilinear piece in cell $C_{j,k} \in \mathscr{C}^{(\ell)}$ can be constructed with the point values $B_{j\pm\frac{1}{2},k\pm\frac{1}{2}}$:

$$\begin{aligned}\widetilde{B}(x,y) = {} & B_{j-\frac{1}{2},k-\frac{1}{2}} + (B_{j+\frac{1}{2},k-\frac{1}{2}} - B_{j-\frac{1}{2},k-\frac{1}{2}}) \frac{x - x_{j-\frac{1}{2}}}{\Delta x/2^{\ell-1}} \\ & + (B_{j-\frac{1}{2},k+\frac{1}{2}} - B_{j-\frac{1}{2},k-\frac{1}{2}}) \frac{y - y_{k-\frac{1}{2}}}{\Delta y/2^{\ell-1}} \\ & + (B_{j+\frac{1}{2},k+\frac{1}{2}} - B_{j+\frac{1}{2},k-\frac{1}{2}} - B_{j-\frac{1}{2},k+\frac{1}{2}} + B_{j-\frac{1}{2},k-\frac{1}{2}}) \frac{x - x_{j-\frac{1}{2}}}{\Delta x/2^{\ell-1}} \cdot \frac{y - y_{k-\frac{1}{2}}}{\Delta y/2^{\ell-1}}, \\ & (x,y) \in C_{j,k}.\end{aligned}$$

Step 3. Set $\ell := \ell + 1$.

Step 4. If $\ell \le m$, then go to Step 2.

The cell average of $\widetilde{B}$ over the cell $C_{j,k}$ is equal to its value at the center, that is

$$\begin{aligned} B_{j,k} := \widetilde{B}(x_j, y_k) &= \frac{1}{\Delta x_{j,k}\Delta y_{j,k}} \iint\limits_{C_{j,k}} \widetilde{B}(x,y)\,\mathrm{d}x\,\mathrm{d}y \\ &= \frac{B_{j+\frac{1}{2},k} + B_{j-\frac{1}{2},k} + B_{j,k+\frac{1}{2}} + B_{j,k-\frac{1}{2}}}{4}, \end{aligned} \tag{4.3.8}$$

where

$$B_{j\pm\frac{1}{2},k} := \widetilde{B}(x_{j\pm\frac{1}{2}}, y_k) = \frac{1}{2}\left(B_{j\pm\frac{1}{2},k+\frac{1}{2}} + B_{j\pm\frac{1}{2},k-\frac{1}{2}}\right), \tag{4.3.9}$$

and

$$B_{j,k\pm\frac{1}{2}} := \widetilde{B}(x_j, y_{k\pm\frac{1}{2}}) = \frac{1}{2}\left(B_{j+\frac{1}{2},k\pm\frac{1}{2}} + B_{j-\frac{1}{2},k\pm\frac{1}{2}}\right). \tag{4.3.10}$$

4.3.3 Piecewise linear reconstructions

In this section, we construct a spatial second-order scheme, which employs a piecewise polynomial interpolation $\widetilde{\boldsymbol{U}}$, where

$$\widetilde{\boldsymbol{U}}(x,y) = (\boldsymbol{U}_x)_{j,k}[x - x_j] + (\boldsymbol{U}_y)_{j,k}[y - y_k], \quad (x,y) \in C_{j,k}. \tag{4.3.11}$$

Note that such a reconstruction makes it impossible to develop a non-oscillatory scheme. Thus, instead of reconstructing conservative variables in $\boldsymbol{U}$, we reform $\mathscr{U} := (w, hu, hv, \rho)^\top$ and then obtain the point values of $\mathscr{U}$ for the cell $C_{j,k}$ from Figure 4.2 which results in

$$\begin{aligned}
\mathscr{U}^+_{j+\frac{1}{2},k} &= \overline{\mathscr{U}}_{j+1,k} - \frac{\Delta x_{j+1,k}}{2}(\mathscr{U}_x)_{j+1,k}\,,\\
\mathscr{U}^-_{j+\frac{1}{2},k} &= \overline{\mathscr{U}}_{j,k} + \frac{\Delta x_{j,k}}{2}(\mathscr{U}_x)_{j,k}\,,\\
\mathscr{U}^+_{j-\frac{1}{2},k\pm\frac{1}{4}} &= \overline{\mathscr{U}}_{j,k} - \frac{\Delta x_{j,k}}{2}(\mathscr{U}_x)_{j,k} \pm \frac{\Delta y_{j,k}}{2}(\mathscr{U}_y)_{j,k}\,,\\
\mathscr{U}^-_{j-\frac{1}{2},k\pm\frac{1}{4}} &= \overline{\mathscr{U}}_{j-\frac{1}{4},k\pm\frac{1}{4}} + \frac{\Delta x_{j,k}}{4}(\mathscr{U}_x)_{j-\frac{1}{4},k\pm\frac{1}{4}},
\end{aligned} \tag{4.3.12}$$

where $\overline{\mathscr{U}}_{j-\frac{1}{4},k-\frac{1}{4}}$ and $\overline{\mathscr{U}}_{j-\frac{1}{4},k+\frac{1}{4}}$ denote the cell averages of $\mathscr{U}$ over the cells I and II, respectively.

Note that in (4.3.12) the density variable $\rho_{j,k}$ is computed as

$$\rho_{j,k} := \frac{\overline{(h\rho)}_{j,k}}{\overline{h}_{j,k}}, \qquad \overline{h}_{j,k} := \overline{w}_{j,k} - B_{j,k}, \tag{4.3.13}$$

and the point values of h and $h\rho$ read as

$$\begin{aligned}
&h^+_{j-\frac{1}{2},k\pm\frac{1}{4}} = w^+_{j-\frac{1}{2},k\pm\frac{1}{4}} - B_{j-\frac{1}{2},k\pm\frac{1}{4}}, \quad h^-_{j+\frac{1}{2},k} = w^-_{j+\frac{1}{2},k} - B_{j+\frac{1}{2},k},\\
&h^+_{j,k-\frac{1}{2}} = w^+_{j,k-\frac{1}{2}} - B_{j,k-\frac{1}{2}}, \quad \text{and} \quad h^-_{j,k+\frac{1}{2}} = w^-_{j,k+\frac{1}{2}} - B_{j,k+\frac{1}{2}},
\end{aligned}$$

and

$$\begin{aligned}
&(h\rho)^+_{j-\frac{1}{2},k\pm\frac{1}{4}} = h^+_{j-\frac{1}{2},k\pm\frac{1}{4}} \cdot \rho^+_{j-\frac{1}{2},k\pm\frac{1}{4}}, \quad (h\rho)^-_{j+\frac{1}{2},k} = h^-_{j+\frac{1}{2},k} \cdot \rho^-_{j+\frac{1}{2},k},\\
&(h\rho)^+_{j,k-\frac{1}{2}} = h^+_{j,k-\frac{1}{2}} \cdot \rho^+_{j,k-\frac{1}{2}}, \quad \text{and} \quad (h\rho)^-_{j,k+\frac{1}{2}} = h^-_{j,k+\frac{1}{2}} \cdot \rho^-_{j,k+\frac{1}{2}}.
\end{aligned}$$

We compute the slopes $(\mathscr{U}_x)$ and $(\mathscr{U}_y)$ using the minmod limiter to be able to minimize oscillations (see, e.g., [7, 50, 88]):

$$(\mathscr{U}_x)_{j,k} = \text{minmod}\left(\frac{\overline{\mathscr{U}}_{j,k} - \overline{\mathscr{U}}_{j-\frac{1}{4},k-\frac{1}{4}}}{3\Delta x_{j,k}/4}, \frac{\overline{\mathscr{U}}_{j,k} - \overline{\mathscr{U}}_{j-\frac{1}{4},k+\frac{1}{4}}}{3\Delta x_{j,k}/4}, \frac{\overline{\mathscr{U}}_{j+1,k} - \overline{\mathscr{U}}_{j,k}}{\Delta x_{j,k}}\right),$$
$$(\mathscr{U}_y)_{j,k} = \text{minmod}\left(\frac{\overline{\mathscr{U}}_{j,k} - \overline{\mathscr{U}}_{j,k-1}}{\Delta y_{j,k}}, \frac{\overline{\mathscr{U}}_{j,k+1} - \overline{\mathscr{U}}_{j,k}}{\Delta y_{j,k}}\right) \tag{4.3.14}$$

where the minmod function is defined by

$$min\{z_1, z_2, ...\} := \begin{cases} min_j\{z_j\}, & \text{if } z_j > 0 \quad \forall j, \\ max_j\{z_j\}, & \text{if } z_j < 0 \quad \forall j, \\ 0, & \text{otherwise.} \end{cases}$$

Note that employing the minmod limiter (4.3.14) guarantees positivity of the point values of ρ [19]. Therefore, we only address the positivity preserving correction of w in the following section.

4.3.3.1 Positivity preserving correction of w

The piecewise linear reconstruction (4.3.14) cannot guarantee the non-negativity of

$$\widetilde{h}(x,y) := \widetilde{w}(x,y) - \widetilde{B}(x,y).$$

The following inequalities must be satisfied specifically for the configuration in Figure 4.2 [28]:

$$h^+_{j-\frac{1}{2},k\pm\frac{1}{4}} = w^+_{j-\frac{1}{2},k\pm\frac{1}{4}} - B_{j-\frac{1}{2},k\pm\frac{1}{4}} \geq 0, \quad h^-_{j+\frac{1}{2},k} = w^-_{j+\frac{1}{2},k} - B_{j+\frac{1}{2},k} \geq 0,$$
$$h^+_{j,k-\frac{1}{2}} = w^+_{j,k-\frac{1}{2}} - B_{j,k-\frac{1}{2}} \geq 0, \quad \text{and} \quad h^-_{j,k+\frac{1}{2}} = w^-_{j,k+\frac{1}{2}} - B_{j,k+\frac{1}{2}} \geq 0.$$

$\widetilde{w}$ would need correction if at least one of these inequalities is not satisfied in the cell $C_{j,k}$. We denote the four corner point values of $\widetilde{w}$ over the cell $C_{j,k}$ by

$$w^{\text{NE}}_{j,k} := \widetilde{w}(x_{j+\frac{1}{2}} - 0, y_{k+\frac{1}{2}} - 0), \quad w^{\text{SE}}_{j,k} := \widetilde{w}(x_{j+\frac{1}{2}} - 0, y_{k-\frac{1}{2}} + 0),$$

$$w_{j,k}^{\mathrm{NW}} := \widetilde{w}(x_{j-\frac{1}{2}}+0, y_{k+\frac{1}{2}}-0), \quad w_{j,k}^{\mathrm{SW}} := \widetilde{w}(x_{j-\frac{1}{2}}+0, y_{k-\frac{1}{2}}+0).$$

If,

$$\begin{aligned} &w_{j,k}^{\mathrm{NE}} \geq B_{j+\frac{1}{2},k+\frac{1}{2}}, \quad w_{j,k}^{\mathrm{SE}} \geq B_{j+\frac{1}{2},k-\frac{1}{2}}, \\ &w_{j,k}^{\mathrm{NW}} \geq B_{j-\frac{1}{2},k+\frac{1}{2}} \quad \text{and} \quad w_{j,k}^{\mathrm{SW}} \geq B_{j-\frac{1}{2},k-\frac{1}{2}}, \end{aligned} \tag{4.3.15}$$

then we set

$$\begin{aligned} \mathring{w}(x,y) = &w_{j,k}^{\mathrm{SW}} + (w_{j,k}^{\mathrm{SE}} - w_{j,k}^{\mathrm{SW}}) \frac{x - x_{j-\frac{1}{2}}}{\Delta x_{j,k}} + (w_{j,k}^{\mathrm{NW}} - w_{j,k}^{\mathrm{SW}}) \frac{y - y_{k-\frac{1}{2}}}{\Delta y_{j,k}} \\ &+ (w_{j,k}^{\mathrm{NE}} - w_{j,k}^{\mathrm{SE}} - w_{j,k}^{\mathrm{NW}} + w_{j,k}^{\mathrm{SW}}) \frac{x - x_{j-\frac{1}{2}}}{\Delta x_{j,k}} \cdot \frac{y - y_{k-\frac{1}{2}}}{\Delta y_{j,k}}, \quad (x,y) \in C_{j,k}. \end{aligned} \tag{4.3.16}$$

If at least one of the inequalities in (4.3.15) is not satisfied, correction for the point values of w at the vertices of $C_{j,k}$ should be implemented. There are three different cases to be considered.

Case 1: only one of the inequalities in (4.3.15) *is not satisfied.* We assume that $w_{j,k}^{\mathrm{NE}} < B_{j+\frac{1}{2},k+\frac{1}{2}}$ and perform

$$\begin{aligned} &\mathring{w}_{j,k}^{\mathrm{NE}} = B_{j+\frac{1}{2},k+\frac{1}{2}}, \quad \mathring{w}_{j,k}^{\mathrm{SE}} = B_{j+\frac{1}{2},k-\frac{1}{2}} + \frac{4}{3}(\overline{w}_{j,k} - B_{j,k}), \\ &\mathring{w}_{j,k}^{\mathrm{NW}} = B_{j-\frac{1}{2},k+\frac{1}{2}} + \frac{4}{3}(\overline{w}_{j,k} - B_{j,k}), \quad \mathring{w}_{j,k}^{\mathrm{SW}} = B_{j-\frac{1}{2},k-\frac{1}{2}} + \frac{4}{3}(\overline{w}_{j,k} - B_{j,k}). \end{aligned}$$

Case 2: only two of the inequalities in (4.3.15) *are not satisfied.* We assume that $w_{j,k}^{\mathrm{NE}} < B_{j+\frac{1}{2},k+\frac{1}{2}}$ and $w_{j,k}^{\mathrm{SE}} < B_{j+\frac{1}{2},k-\frac{1}{2}}$ and perform

$$\begin{aligned} &\mathring{w}_{j,k}^{\mathrm{NE}} = B_{j+\frac{1}{2},k+\frac{1}{2}}, \quad \mathring{w}_{j,k}^{\mathrm{SE}} = B_{j+\frac{1}{2},k-\frac{1}{2}}, \\ &\mathring{w}_{j,k}^{\mathrm{NW}} = B_{j-\frac{1}{2},k+\frac{1}{2}} + 2(\overline{w}_{j,k} - B_{j,k}), \quad \mathring{w}_{j,k}^{\mathrm{SW}} = B_{j-\frac{1}{2},k-\frac{1}{2}} + 2(\overline{w}_{j,k} - B_{j,k}). \end{aligned}$$

Case 3: only three of the inequalities in (4.3.15) *are not satisfied.* We assume that $w_{j,k}^{\mathrm{NE}} < B_{j+\frac{1}{2},k+\frac{1}{2}}$, $w_{j,k}^{\mathrm{SE}} < B_{j+\frac{1}{2},k-\frac{1}{2}}$ and $w_{j,k}^{\mathrm{NW}} < B_{j-\frac{1}{2},k+\frac{1}{2}}$ and perform

$$\mathring{w}_{j,k}^{\mathrm{NE}} = B_{j+\frac{1}{2},k+\frac{1}{2}}, \quad \mathring{w}_{j,k}^{\mathrm{SE}} = B_{j+\frac{1}{2},k-\frac{1}{2}}, \quad \mathring{w}_{j,k}^{\mathrm{NW}} = B_{j-\frac{1}{2},k+\frac{1}{2}},$$

$$\mathring{w}^{\mathrm{SW}}_{j,k} = 4\,\overline{w}_{j,k} - B_{j+\frac{1}{2},k+\frac{1}{2}} - B_{j+\frac{1}{2},k-\frac{1}{2}} - B_{j-\frac{1}{2},k+\frac{1}{2}}.$$

We use the corrected point values $\mathring{w}^{\mathrm{NE}}_{j,k}$, $\mathring{w}^{\mathrm{SE}}_{j,k}$, $\mathring{w}^{\mathrm{NW}}_{j,k}$ and $\mathring{w}^{\mathrm{SW}}_{j,k}$ in the above three cases to construct the corrected bilinear approximant

$$\begin{aligned}\mathring{w}(x,y) = {} & \mathring{w}^{\mathrm{SW}}_{j,k} + (\mathring{w}^{\mathrm{SE}}_{j,k} - \mathring{w}^{\mathrm{SW}}_{j,k})\,\frac{x - x_{j-\frac{1}{2}}}{\Delta x_{j,k}} + (\mathring{w}^{\mathrm{NW}}_{j,k} - \mathring{w}^{\mathrm{SW}}_{j,k})\,\frac{y - y_{k-\frac{1}{2}}}{\Delta y_{j,k}} \\ & + (\mathring{w}^{\mathrm{NE}}_{j,k} - \mathring{w}^{\mathrm{SE}}_{j,k} - \mathring{w}^{\mathrm{NW}}_{j,k} + \mathring{w}^{\mathrm{SW}}_{j,k})\,\frac{x - x_{j-\frac{1}{2}}}{\Delta x_{j,k}} \cdot \frac{y - y_{k-\frac{1}{2}}}{\Delta y_{j,k}}, \quad (x,y) \in C_{j,k}.\end{aligned}$$

The constructed bilinear piece $\mathring{w}(x,y)$ is positivity preserving and conservative. The point values of w at the cell $C_{j,k}$ in Figure 4.2 are

$$\begin{aligned} w^{+}_{j-\frac{1}{2},k\pm\frac{1}{4}} &= \mathring{w}(x_{j-\frac{1}{2}} + 0, y_{k\pm\frac{1}{4}}), & w^{-}_{j+\frac{1}{2},k} &= \mathring{w}(x_{j+\frac{1}{2}} - 0, y_k), \\ w^{+}_{j,k-\frac{1}{2}} &= \mathring{w}(x_j, y_{k-\frac{1}{2}} + 0), & w^{-}_{j,k+\frac{1}{2}} &= \mathring{w}(x_j, y_{k+\frac{1}{2}} - 0) \end{aligned}$$

and therefore the corresponding corrected values of h,

$$\begin{aligned} h^{+}_{j-\frac{1}{2},k\pm\frac{1}{4}} &= w^{+}_{j-\frac{1}{2},k\pm\frac{1}{4}} - B_{j-\frac{1}{2},k\pm\frac{1}{4}}, & h^{-}_{j+\frac{1}{2},k} &= w^{-}_{j+\frac{1}{2},k} - B_{j+\frac{1}{2},k}, \\ h^{+}_{j,k-\frac{1}{2}} &= w^{+}_{j,k-\frac{1}{2}} - B_{j,k-\frac{1}{2}}, & h^{-}_{j,k+\frac{1}{2}} &= w^{-}_{j,k+\frac{1}{2}} - B_{j,k+\frac{1}{2}}, \end{aligned}$$

are nonnegative.

To prevent very small or even zero values of cell averages $\overline{h}$, h, $\overline{\rho}$, and ρ at the boundaries of cell $C_{j,k}$, the computation of the corresponding point values of u, v, and ρ is required as follows [19, 28, 46]:

$$u := \frac{\sqrt{2}\,h(hu)}{\sqrt{h^4 + \max\{h^4, \varepsilon\}}}, \quad v := \frac{\sqrt{2}\,h(hv)}{\sqrt{h^4 + \max\{h^4, \varepsilon\}}}, \quad \rho := \frac{\sqrt{2}\,h(h\rho)}{\sqrt{h^4 + \max\{h^4, \varepsilon\}}},$$

where we choose $\varepsilon = \max\{\min_{j,k}\{(\Delta x_{j,k})^4\}, \min_{j,k}\{(\Delta y_{j,k})^4\}\}$. The conservative variables recalculation is done by setting:

$$(hu) := h \cdot u, \qquad (hv) := h \cdot v, \qquad (h\rho) := h \cdot \rho.$$

Note that for the sake of brevity, in the above equations we have omitted all of the indices.

4.3.4 Local speeds

The one-sided local speeds of propagation, denoted at the corresponding cell interfaces by $a^{\pm}_{\alpha,\beta}$ and $b^{\pm}_{\gamma,\delta}$ can be estimated by

$$\begin{aligned}
a^{+}_{\alpha,\beta} &= \max\left\{u^{+}_{\alpha,\beta} + \sqrt{\frac{g}{\rho_\circ}\,h^{+}_{\alpha,\beta}\,\rho^{+}_{\alpha,\beta}},\; u^{-}_{\alpha,\beta} + \sqrt{\frac{g}{\rho_\circ}\,h^{-}_{\alpha,\beta}\,\rho^{-}_{\alpha,\beta}},\; 0\right\},\\
a^{-}_{\alpha,\beta} &= \min\left\{u^{+}_{\alpha,\beta} - \sqrt{\frac{g}{\rho_\circ}\,h^{+}_{\alpha,\beta}\,\rho^{+}_{\alpha,\beta}},\; u^{-}_{\alpha,\beta} - \sqrt{\frac{g}{\rho_\circ}\,h^{-}_{\alpha,\beta}\,\rho^{-}_{\alpha,\beta}},\; 0\right\},\\
b^{+}_{\gamma,\delta} &= \max\left\{v^{+}_{\gamma,\delta} + \sqrt{\frac{g}{\rho_\circ}\,h^{+}_{\gamma,\delta}\,\rho^{+}_{\gamma,\delta}},\; v^{-}_{\gamma,\delta} + \sqrt{\frac{g}{\rho_\circ}\,h^{-}_{\gamma,\delta}\,\rho^{-}_{\gamma,\delta}},\; 0\right\},\\
b^{-}_{\gamma,\delta} &= \min\left\{v^{+}_{\gamma,\delta} - \sqrt{\frac{g}{\rho_\circ}\,h^{+}_{\gamma,\delta}\,\rho^{+}_{\gamma,\delta}},\; v^{-}_{\gamma,\delta} - \sqrt{\frac{g}{\rho_\circ}\,h^{-}_{\gamma,\delta}\,\rho^{-}_{\gamma,\delta}},\; 0\right\},
\end{aligned} \tag{4.3.17}$$

where

$$(\alpha,\beta) \in \left\{(j-\frac{1}{2},k-\frac{1}{4}),(j-\frac{1}{2},k+\frac{1}{4}),(j+\frac{1}{2},k)\right\}$$

and

$$(\gamma,\delta) \in \left\{(j,k-\frac{1}{2}),(j,k+\frac{1}{2})\right\}$$

in the configuration considered in Figure 4.2.

4.3.5 Central-upwind numerical fluxes

We use the central-upwind fluxes from [46], originally derived in [49]:

$$\begin{aligned}
\boldsymbol{H}^{x}_{\alpha,\beta} = &\frac{a^{+}_{\alpha,\beta}\boldsymbol{F}(\boldsymbol{U}^{-}_{\alpha,\beta},B_{\alpha,\beta}) - a^{-}_{\alpha,\beta}\boldsymbol{F}(\boldsymbol{U}^{+}_{\alpha,\beta},B_{\alpha,\beta})}{a^{+}_{\alpha,\beta}-a^{-}_{\alpha,\beta}}\\
&+\frac{a^{+}_{\alpha,\beta}a^{-}_{\alpha,\beta}}{a^{+}_{\alpha,\beta}-a^{-}_{\alpha,\beta}}\left[\boldsymbol{U}^{+}_{\alpha,\beta}-\boldsymbol{U}^{-}_{\alpha,\beta}\right],
\end{aligned}$$

$$\boldsymbol{H}^{y}_{\gamma,\delta} = \frac{b^{+}_{\gamma,\delta}\boldsymbol{G}(\boldsymbol{U}^{-}_{\gamma,\delta},B_{\gamma,\delta}) - b^{-}_{\gamma,\delta}\boldsymbol{G}(\boldsymbol{U}^{+}_{\gamma,\delta},B_{\gamma,\delta})}{b^{+}_{\gamma,\delta}-b^{-}_{\gamma,\delta}}$$

$$+\frac{b^+_{\gamma,\delta}b^-_{\gamma,\delta}}{b^+_{\gamma,\delta}-b^-_{\gamma,\delta}}\left[\boldsymbol{U}^+_{\gamma,\delta}-\boldsymbol{U}^-_{\gamma,\delta}\right], \tag{4.3.18}$$

where (α,β) and (γ,δ) are same as before.

4.3.6 Well-balanced discretization of the source term

A numerical scheme is well-balanced when the discretized cell average of the source term, $\overline{\boldsymbol{S}}_{j,k}=\left(0,\overline{S}^{(2)}_{j,k},\overline{S}^{(3)}_{j,k},0\right)^\top$, exactly balances the numerical fluxes in equation (4.3.6) at the "lake-at-rest" steady state (4.1.2), that is, when the right-hand side of (4.3.6) vanishes as long as $\overline{\mathscr{W}}_{j,k}\equiv(\widehat{w},0,0,\widehat{\rho})^\top$ for all (j,k), where $\widehat{w}$ and $\widehat{\rho}$ are constants.

Notice that at the "lake-at-rest" all of the reconstructed point values are $w^\pm=\widetilde{w}$, $u^\pm=v^\pm=0$ and $\rho^\pm=\widetilde{\rho}$, and thus, $a^+_{\alpha,\beta}=-a^-_{\alpha,\beta}$, $\forall(\alpha,\beta)$, $b^+_{\gamma,\delta}=-b^-_{\gamma,\delta}\,\forall(\gamma,\delta)$, and the numerical fluxes (4.3.18) reduce to

$$\boldsymbol{H}^x_{\alpha,\beta}=\left(0,\frac{g}{2\rho_\circ}\widehat{\rho}\left(\widehat{w}-B_{\alpha,\beta}\right)^2,0,0\right)^\top,\boldsymbol{H}^y_{\gamma,\delta}=\left(0,0,\frac{g}{2\rho_\circ}\widehat{\rho}\left(\widehat{w}-B_{\gamma,\delta}\right)^2,0\right)^\top,$$

and the flux terms on the RHS of (4.3.6) then become

$$\begin{aligned}
&-\frac{\boldsymbol{H}^x_{j+\frac12,k}-\dfrac{\boldsymbol{H}^x_{j-\frac12,k-\frac14}+\boldsymbol{H}^x_{j-\frac12,k+\frac14}}{2}}{\Delta x_{j,k}}-\frac{\boldsymbol{H}^y_{j,k+\frac12}-\boldsymbol{H}^y_{j,k-\frac12}}{\Delta y_{j,k}}\\
&=-\frac{g}{2\rho_\circ}\widehat{\rho}\begin{pmatrix}0\\ \dfrac{\left(\widehat{w}-B_{j+\frac12,k}\right)^2}{\Delta x_{j,k}}-\dfrac{\left(\widehat{w}-B_{j-\frac12,k-\frac14}\right)^2}{2\Delta x_{j,k}}-\dfrac{\left(\widehat{w}-B_{j-\frac12,k+\frac14}\right)^2}{2\Delta x_{j,k}}\\ \dfrac{\left(\widehat{w}-B_{j,k+\frac12}\right)^2}{\Delta y_{j,k}}-\dfrac{\left(\widehat{w}-B_{j,k-\frac12}\right)^2}{\Delta y_{j,k}}\end{pmatrix}.
\end{aligned}\tag{4.3.19}$$

By applying the Green's theorem, the source term in 4.3.6 can be approximated by

$$\begin{aligned}
-\frac{g}{2\rho_\circ}\rho\left(w-B\right)B_x&=\frac{g}{2\rho_\circ}\left[\rho\left(w-B\right)^2\right]_x-\frac{g}{\rho_\circ}\rho\left(w-B\right)w_x,\\
-\frac{g}{2\rho_\circ}\rho\left(w-B\right)B_y&=\frac{g}{2\rho_\circ}\left[\rho\left(w-B\right)^2\right]_y-\frac{g}{\rho_\circ}\rho\left(w-B\right)w_y.
\end{aligned}$$

We now rewrite the cell averages of the second and third components of the integral in (4.3.7)

$$\frac{g}{2\rho_\circ}\int_{y_{k-\frac{1}{2}}}^{y_{k+\frac{1}{2}}}\left[\rho\,(w-B)^2\Big|_{x=x_{j+\frac{1}{2}}}-\rho\,(w-B)^2\Big|_{x=x_{j-\frac{1}{2}}}\right]\mathrm{d}y$$
$$-\frac{g}{\rho_\circ}\int_{x_{j-\frac{1}{2}}}^{x_{j+\frac{1}{2}}}\int_{y_{k-\frac{1}{2}}}^{y_{k+\frac{1}{2}}}\rho\,(w-B)w_x\,\mathrm{d}y\,\mathrm{d}x, \tag{4.3.20}$$

and

$$\frac{g}{2\rho_\circ}\int_{x_{j-\frac{1}{2}}}^{x_{j+\frac{1}{2}}}\left[\rho\,(w-B)^2\Big|_{y=y_{k+\frac{1}{2}}}-\rho\,(w-B)^2\Big|_{y=y_{k-\frac{1}{2}}}\right]\mathrm{d}x$$
$$-\frac{g}{\rho_\circ}\int_{x_{j-\frac{1}{2}}}^{x_{j+\frac{1}{2}}}\int_{y_{k-\frac{1}{2}}}^{y_{k+\frac{1}{2}}}\rho\,(w-B)w_y\,\mathrm{d}y\,\mathrm{d}x, \tag{4.3.21}$$

We then approximate the integrals in (4.3.20) and (4.3.21), which results in the following quadrature for the second and third components of the source term [28]:

$$\begin{aligned}\overline{S}^{(2)}_{j,k}\approx\frac{g}{2\rho_\circ\Delta x_{j,k}}\Bigg[&\rho^-_{j+\frac{1}{2},k}\left(w^-_{j+\frac{1}{2},k}-B_{j+\frac{1}{2},k}\right)^2\\&-\frac{\rho^+_{j-\frac{1}{2},k-\frac{1}{4}}\left(w^+_{j-\frac{1}{2},k-\frac{1}{4}}-B_{j-\frac{1}{2},k-\frac{1}{4}}\right)^2}{2}\\&-\frac{\rho^+_{j-\frac{1}{2},k+\frac{1}{4}}\left(w^+_{j-\frac{1}{2},k+\frac{1}{4}}-B_{j-\frac{1}{2},k+\frac{1}{4}}\right)^2}{2}\Bigg]\\&-\frac{g}{\rho_\circ}\rho_{j,k}(w_x)_{j,k}\left(\overline{w}_{j,k}-B_{j,k}\right),\\\overline{S}^{(3)}_{j,k}\approx\frac{g}{2\rho_\circ\Delta y_{j,k}}\Bigg[&\rho^-_{j,k+\frac{1}{2}}\left(w^-_{j,k+\frac{1}{2}}-B_{j,k+\frac{1}{2}}\right)^2\\&-\rho^+_{j,k-\frac{1}{2}}\left(w^+_{j,k-\frac{1}{2}}-B_{j,k-\frac{1}{2}}\right)^2\Bigg]\end{aligned}$$

$$- \frac{g}{\rho_\circ}\rho_{j,k}(w_y)_{j,k}\left(\overline{w}_{j,k} - B_{j,k}\right). \tag{4.3.22}$$

We finally note that the scheme now preserves the solution at "lake-at-rest" where, $(w_x)_{j,k} = (w_y)_{j,k} \equiv 0$, $\forall(j,k)$ and thus (4.3.19) and (4.3.22) express that the RHS of (4.3.6) vanishes and therefore, the scheme is well-balanced.

4.3.7 Positivity preserving property and time discretization

The central-upwind scheme is able to preserve the positivity of h and ρ; see [28, 42, 46]. In this section, we extend the positivity proof from [28] to implement on the coupled variable density system. To this end, we integrate equation (4.3.6) in time using a forward Euler method. For the first component, this results in

$$\begin{aligned}\overline{w}_{j,k}^{n+1} =& \overline{w}_{j,k}^{n} - \lambda_{j,k}^{n}\left(H^{x,(1)}_{j+\frac{1}{2},k} - \frac{H^{x,(1)}_{j-\frac{1}{2},k-\frac{1}{4}} + H^{x,(1)}_{j-\frac{1}{2},k+\frac{1}{4}}}{2}\right)\\ &- \mu_{j,k}^{n}\left(H^{y,(1)}_{j,k+\frac{1}{2}} - H^{y,(1)}_{j,k-\frac{1}{2}}\right),\end{aligned} \tag{4.3.23}$$

$$\begin{aligned}\overline{(h\rho)}_{j,k}^{n+1} =& \overline{(h\rho)}_{j,k}^{n} - \lambda_{j,k}^{n}\left(H^{x,(4)}_{j+\frac{1}{2},k} - \frac{H^{x,(4)}_{j-\frac{1}{2},k-\frac{1}{4}} + H^{x,(4)}_{j-\frac{1}{2},k+\frac{1}{4}}}{2}\right)\\ &- \mu_{j,k}^{n}\left(H^{y,(4)}_{j,k+\frac{1}{2}} - H^{y,(4)}_{j,k-\frac{1}{2}}\right),\end{aligned} \tag{4.3.24}$$

where $\overline{w}_{j,k}^{n} := \overline{w}_{j,k}(t^n)$, $\overline{w}_{j,k}^{n+1} := \overline{w}_{j,k}(t^{n+1})$, $\overline{(h\rho)}_{j,k}^{n} := \overline{(h\rho)}_{j,k}(t^n)$, and $\overline{(h\rho)}_{j,k}^{n+1} := \overline{(h\rho)}_{j,k}(t^{n+1})$ with $t^{n+1} = t^n + \Delta t^n$, $\lambda_{j,k}^{n} := \Delta t^n/\Delta x_{j,k}$, $\mu_{j,k}^{n} := \Delta t^n/\Delta y_{j,k}$, and the numerical fluxes on the RHS are evaluated at time level $t = t^n$ using (4.3.18):

$$\begin{aligned}H^{x,(1)}_{\alpha,\beta} &= \frac{a^+_{\alpha,\beta}(hu)^-_{\alpha,\beta} - a^-_{\alpha,\beta}(hu)^+_{\alpha,\beta}}{a^+_{\alpha,\beta} - a^-_{\alpha,\beta}} + \frac{a^+_{\alpha,\beta}a^-_{\alpha,\beta}}{a^+_{\alpha,\beta} - a^-_{\alpha,\beta}}\left[w^+_{\alpha,\beta} - w^-_{\alpha,\beta}\right],\\ H^{y,(1)}_{\gamma,\delta} &= \frac{b^+_{\gamma,\delta}(hv)^-_{\gamma,\delta} - b^-_{\gamma,\delta}(hv)^+_{\gamma,\delta}}{b^+_{\gamma,\delta} - b^-_{\gamma,\delta}} + \frac{b^+_{\gamma,\delta}b^-_{\gamma,\delta}}{b^+_{\gamma,\delta} - b^-_{\gamma,\delta}}\left[w^+_{\gamma,\delta} - w^-_{\gamma,\delta}\right],\end{aligned} \tag{4.3.25}$$

and

$$
\begin{aligned}
H^{x,(4)}_{\alpha,\beta} =& \frac{a^+_{\alpha,\beta}\,\rho^-_{\alpha,\beta}(hu)^-_{\alpha,\beta} - a^-_{\alpha,\beta}\,\rho^+_{\alpha,\beta}(hu)^+_{\alpha,\beta}}{a^+_{\alpha,\beta} - a^-_{\alpha,\beta}} \\
&+ \frac{a^+_{\alpha,\beta}a^-_{\alpha,\beta}}{a^+_{\alpha,\beta} - a^-_{\alpha,\beta}}\left[(h\rho)^+_{\alpha,\beta} - (h\rho)^-_{\alpha,\beta}\right], \\
H^{y,(4)}_{\gamma,\delta} =& \frac{b^+_{\gamma,\delta}\,\rho^-_{\gamma,\delta}(hv)^-_{\gamma,\delta} - b^-_{\gamma,\delta}\,\rho^+_{\gamma,\delta}(hv)^+_{\gamma,\delta}}{b^+_{\gamma,\delta} - b^-_{\gamma,\delta}} \\
&+ \frac{b^+_{\gamma,\delta}b^-_{\gamma,\delta}}{b^+_{\gamma,\delta} - b^-_{\gamma,\delta}}\left[(h\rho)^+_{\gamma,\delta} - (h\rho)^-_{\gamma,\delta}\right],
\end{aligned}
\tag{4.3.26}
$$

where $(h\rho)^{\pm}_{\alpha,\beta} = h^{\pm}_{\alpha,\beta}\cdot\rho^{\pm}_{\alpha,\beta}$ and $(h\rho)^{\pm}_{\gamma,\delta} = h^{\pm}_{\gamma,\delta}\cdot\rho^{\pm}_{\gamma,\delta}$, and

$$
(\alpha,\beta) \in \left\{(j-\frac{1}{2},k-\frac{1}{4}),(j-\frac{1}{2},k+\frac{1}{4}),(j+\frac{1}{2},k)\right\}
$$

and

$$
(\gamma,\delta) \in \left\{(j,k-\frac{1}{2}),(j,k+\frac{1}{2})\right\}
$$

for the configuration considered in Figure 4.2.

If $\overline{h}^n_{j,k} \geq 0$ for all (j,k), then the point values of h computed using piecewise linear/bilinear reconstructions of w and B presented in §4.3.2 and §4.3.3, are non-negative. Moreover, using (4.3.8)–(4.3.10) and the similar relationships for the reconstructed point values of w, we have

$$
\overline{h}^n_{j,k} = \frac{1}{4}\left(\frac{h^+_{j-\frac{1}{2},k-\frac{1}{4}} + h^+_{j-\frac{1}{2},k+\frac{1}{4}}}{2} + h^-_{j+\frac{1}{2},k} + h^+_{j,k-\frac{1}{2}} + h^-_{j,k+\frac{1}{2}}\right) \tag{4.3.27}
$$

for the configuration considered in Figure 4.2.

We now subtract $B_{j,k}$ from both sides of (4.3.23) and use (4.3.25) and (4.3.27) to rewrite (4.3.23) as follows:

$$
\begin{aligned}
\overline{h}^{n+1}_{j,k} =& -\lambda^n_{j,k}a^-_{j+\frac{1}{2},k}\cdot\frac{a^+_{j+\frac{1}{2},k} - u^+_{j+\frac{1}{2},k}}{a^+_{j+\frac{1}{2},k} - a^-_{j+\frac{1}{2},k}}\cdot h^+_{j+\frac{1}{2},k} \\
&+ \left[\frac{1}{4} - \lambda^n_{j,k}a^+_{j+\frac{1}{2},k}\cdot\frac{u^-_{j+\frac{1}{2},k} - a^-_{j+\frac{1}{2},k}}{a^+_{j+\frac{1}{2},k} - a^-_{j+\frac{1}{2},k}}\right] h^-_{j+\frac{1}{2},k}
\end{aligned}
$$

$$
\begin{aligned}
&+ \frac{\lambda^n_{j,k} a^+_{j-\frac{1}{2},k-\frac{1}{4}}}{2} \cdot \frac{u^-_{j-\frac{1}{2},k-\frac{1}{4}} - a^-_{j-\frac{1}{2},k-\frac{1}{4}}}{a^+_{j-\frac{1}{2},k-\frac{1}{4}} - a^-_{j-\frac{1}{2},k-\frac{1}{4}}} \cdot h^+_{j-\frac{1}{2},k-\frac{1}{4}} \\
&+ \frac{1}{2}\left[\frac{1}{4} - \lambda^n_{j,k} a^-_{j-\frac{1}{2},k-\frac{1}{4}} \cdot \frac{a^+_{j-\frac{1}{2},k-\frac{1}{4}} - u^+_{j-\frac{1}{2},k-\frac{1}{4}}}{a^+_{j-\frac{1}{2},k-\frac{1}{4}} - a^-_{j-\frac{1}{2},k-\frac{1}{4}}}\right] h^+_{j-\frac{1}{2},k-\frac{1}{4}} \\
&+ \frac{\lambda^n_{j,k} a^+_{j-\frac{1}{2},k+\frac{1}{4}}}{2} \cdot \frac{u^-_{j-\frac{1}{2},k+\frac{1}{4}} - a^-_{j-\frac{1}{2},k+\frac{1}{4}}}{a^+_{j-\frac{1}{2},k+\frac{1}{4}} - a^-_{j-\frac{1}{2},k+\frac{1}{4}}} \cdot h^+_{j-\frac{1}{2},k+\frac{1}{4}} \\
&+ \frac{1}{2}\left[\frac{1}{4} - \lambda^n_{j,k} a^-_{j-\frac{1}{2},k+\frac{1}{4}} \cdot \frac{a^+_{j-\frac{1}{2},k+\frac{1}{4}} - u^+_{j-\frac{1}{2},k+\frac{1}{4}}}{a^+_{j-\frac{1}{2},k+\frac{1}{4}} - a^-_{j-\frac{1}{2},k+\frac{1}{4}}}\right] h^+_{j-\frac{1}{2},k+\frac{1}{4}} \\
&- \mu^n_{j,k} b^-_{j,k+\frac{1}{2}} \cdot \frac{b^+_{j,k+\frac{1}{2}} - v^+_{j,k+\frac{1}{2}}}{b^+_{j,k+\frac{1}{2}} - b^-_{j,k+\frac{1}{2}}} \cdot h^+_{j,k+\frac{1}{2}} \\
&+ \left[\frac{1}{4} - \mu^n_{j,k} b^+_{j,k+\frac{1}{2}} \cdot \frac{v^-_{j,k+\frac{1}{2}} - b^-_{j,k+\frac{1}{2}}}{b^+_{j,k+\frac{1}{2}} - b^-_{j,k+\frac{1}{2}}}\right] h^-_{j,k+\frac{1}{2}} \\
&+ \mu^n_{j,k} b^+_{j,k-\frac{1}{2}} \cdot \frac{v^-_{j,k-\frac{1}{2}} - b^-_{j,k-\frac{1}{2}}}{b^+_{j,k-\frac{1}{2}} - b^-_{j,k-\frac{1}{2}}} \cdot h^-_{j,k-\frac{1}{2}} \\
&+ \left[\frac{1}{4} + \mu^n_{j,k} b^-_{j,k-\frac{1}{2}} \cdot \frac{b^+_{j,k-\frac{1}{2}} - v^+_{j,k-\frac{1}{2}}}{b^+_{j,k-\frac{1}{2}} - b^-_{j,k-\frac{1}{2}}}\right] h^+_{j,k-\frac{1}{2}}. \qquad (4.3.28)
\end{aligned}
$$

This shows that the cell averages of h are linear combinations of the reconstructed nonnegative point values of h. Thus, $\overline{h}^{n+1}_{j,k} \geq 0$ provided all of the coefficients in this linear combination are nonnegative.

One can obtain a similar proof for positivity of $\overline{(h\rho)}^{n+1}_{j,k}$ by using the following statements [19],

$$
\begin{aligned}
\overline{h}_{j,k} &= \frac{h^-_{j+\frac{1}{2},k} + \dfrac{h^+_{j-\frac{1}{2},k-\frac{1}{4}} + h^+_{j-\frac{1}{2},k+\frac{1}{4}}}{2}}{2}, \\
\rho_{j,k} &= \frac{\rho^-_{j+\frac{1}{2},k} + \dfrac{\rho^+_{j-\frac{1}{2},k-\frac{1}{4}} + \rho^+_{j-\frac{1}{2},k+\frac{1}{4}}}{2}}{2}, \qquad (4.3.29)
\end{aligned}
$$

and therefore, utilizing (4.3.13), one obtains

$$\begin{aligned}\overline{(h\rho)}^n_{j,k} = &\frac{1}{4}\left[h^-_{j+\frac{1}{2},k}\,\rho^-_{j+\frac{1}{2},k} + \frac{h^+_{j-\frac{1}{2},k-\frac{1}{4}}\,\rho^+_{j-\frac{1}{2},k-\frac{1}{4}} + h^+_{j-\frac{1}{2},k+\frac{1}{4}}\,\rho^+_{j-\frac{1}{2},k+\frac{1}{4}}}{2}\right]\\ &+\frac{1}{4}\left[\frac{h^-_{j+\frac{1}{2},k}\,\rho^+_{j-\frac{1}{2},k-\frac{1}{4}} + h^-_{j+\frac{1}{2},k}\,\rho^+_{j-\frac{1}{2},k+\frac{1}{4}}}{2}\right]\\ &+\frac{1}{4}\left[\frac{h^+_{j-\frac{1}{2},k-\frac{1}{4}}\,\rho^-_{j+\frac{1}{2},k} + h^+_{j-\frac{1}{2},k+\frac{1}{4}}\,\rho^-_{j+\frac{1}{2},k}}{2}\right]\\ &+\frac{1}{4}\left[\frac{h^+_{j-\frac{1}{2},k-\frac{1}{4}}\,\rho^+_{j-\frac{1}{2},k+\frac{1}{4}} + h^+_{j-\frac{1}{2},k+\frac{1}{4}}\,\rho^+_{j-\frac{1}{2},k-\frac{1}{4}}}{4}\right].\end{aligned} \tag{4.3.30}$$

Similarly, it can be shown that

$$\begin{aligned}\overline{(h\rho)}^n_{j,k} = &\frac{1}{4}\left[h^-_{j,k+\frac{1}{2}}\,\rho^-_{j,k+\frac{1}{2}} + h^+_{j,k-\frac{1}{2}}\,\rho^+_{j,k-\frac{1}{2}}\right]\\ &+\frac{1}{4}\left[h^-_{j,k+\frac{1}{2}}\,\rho^+_{j,k-\frac{1}{2}} + h^+_{j,k-\frac{1}{2}}\,\rho^-_{j,k+\frac{1}{2}}\right].\end{aligned} \tag{4.3.31}$$

Finally, from (4.3.30) and (4.3.31) we have

$$\begin{aligned}\overline{(h\rho)}^n_{j,k} = &\frac{1}{8}\left[h^-_{j+\frac{1}{2},k}\,\rho^-_{j+\frac{1}{2},k} + h^-_{j,k+\frac{1}{2}}\,\rho^-_{j,k+\frac{1}{2}} + h^+_{j,k-\frac{1}{2}}\,\rho^+_{j,k-\frac{1}{2}}\right]\\ &+\frac{1}{8}\left[\frac{h^+_{j-\frac{1}{2},k-\frac{1}{4}}\,\rho^+_{j-\frac{1}{2},k-\frac{1}{4}} + h^+_{j-\frac{1}{2},k+\frac{1}{4}}\,\rho^+_{j-\frac{1}{2},k+\frac{1}{4}}}{2}\right]\\ &+\frac{1}{8}\left[\frac{h^-_{j+\frac{1}{2},k}\,\rho^+_{j-\frac{1}{2},k-\frac{1}{4}} + h^-_{j+\frac{1}{2},k}\,\rho^+_{j-\frac{1}{2},k+\frac{1}{4}}}{2}\right]\\ &+\frac{1}{8}\left[\frac{h^+_{j-\frac{1}{2},k-\frac{1}{4}}\,\rho^-_{j+\frac{1}{2},k} + h^+_{j-\frac{1}{2},k+\frac{1}{4}}\,\rho^-_{j+\frac{1}{2},k}}{2}\right]\\ &+\frac{1}{8}\left[\frac{h^+_{j-\frac{1}{2},k-\frac{1}{4}}\,\rho^+_{j-\frac{1}{2},k+\frac{1}{4}} + h^+_{j-\frac{1}{2},k+\frac{1}{4}}\,\rho^+_{j-\frac{1}{2},k-\frac{1}{4}}}{4}\right].\end{aligned} \tag{4.3.32}$$

We rewrite (4.3.24) as follows:

$$
\begin{aligned}
\overline{(h\rho)}_{j,k}^{n+1} = &- \lambda_{j,k}^{n} a_{j+\frac{1}{2},k}^{-} \cdot \frac{a_{j+\frac{1}{2},k}^{+} - u_{j+\frac{1}{2},k}^{+}}{a_{j+\frac{1}{2},k}^{+} - a_{j+\frac{1}{2},k}^{-}} \cdot h_{j+\frac{1}{2},k}^{+} \rho_{j+\frac{1}{2},k}^{+} \\
&+ \left[\frac{1}{8} - \lambda_{j,k}^{n} a_{j+\frac{1}{2},k}^{+} \cdot \frac{u_{j+\frac{1}{2},k}^{-} - a_{j+\frac{1}{2},k}^{-}}{a_{j+\frac{1}{2},k}^{+} - a_{j+\frac{1}{2},k}^{-}} \right] h_{j+\frac{1}{2},k}^{-} \rho_{j+\frac{1}{2},k}^{-} \\
&+ \frac{\lambda_{j,k}^{n} a_{j-\frac{1}{2},k-\frac{1}{4}}^{+}}{2} \cdot \frac{u_{j-\frac{1}{2},k-\frac{1}{4}}^{-} - a_{j-\frac{1}{2},k-\frac{1}{4}}^{-}}{a_{j-\frac{1}{2},k-\frac{1}{4}}^{+} - a_{j-\frac{1}{2},k-\frac{1}{4}}^{-}} \cdot h_{j-\frac{1}{2},k-\frac{1}{4}}^{+} \rho_{j-\frac{1}{2},k-\frac{1}{4}}^{+} \\
&+ \frac{1}{2} \left[\frac{1}{8} - \lambda_{j,k}^{n} a_{j-\frac{1}{2},k-\frac{1}{4}}^{-} \cdot \frac{a_{j-\frac{1}{2},k-\frac{1}{4}}^{+} - u_{j-\frac{1}{2},k-\frac{1}{4}}^{+}}{a_{j-\frac{1}{2},k-\frac{1}{4}}^{+} - a_{j-\frac{1}{2},k-\frac{1}{4}}^{-}} \right] h_{j-\frac{1}{2},k-\frac{1}{4}}^{+} \rho_{j-\frac{1}{2},k-\frac{1}{4}}^{+} \\
&+ \frac{\lambda_{j,k}^{n} a_{j-\frac{1}{2},k+\frac{1}{4}}^{+}}{2} \cdot \frac{u_{j-\frac{1}{2},k+\frac{1}{4}}^{-} - a_{j-\frac{1}{2},k+\frac{1}{4}}^{-}}{a_{j-\frac{1}{2},k+\frac{1}{4}}^{+} - a_{j-\frac{1}{2},k+\frac{1}{4}}^{-}} \cdot h_{j-\frac{1}{2},k+\frac{1}{4}}^{+} \rho_{j-\frac{1}{2},k+\frac{1}{4}}^{+} \\
&+ \frac{1}{2} \left[\frac{1}{8} - \lambda_{j,k}^{n} a_{j-\frac{1}{2},k+\frac{1}{4}}^{-} \cdot \frac{a_{j-\frac{1}{2},k+\frac{1}{4}}^{+} - u_{j-\frac{1}{2},k+\frac{1}{4}}^{+}}{a_{j-\frac{1}{2},k+\frac{1}{4}}^{+} - a_{j-\frac{1}{2},k+\frac{1}{4}}^{-}} \right] h_{j-\frac{1}{2},k+\frac{1}{4}}^{+} \rho_{j-\frac{1}{2},k+\frac{1}{4}}^{+} \\
&- \mu_{j,k}^{n} b_{j,k+\frac{1}{2}}^{-} \cdot \frac{b_{j,k+\frac{1}{2}}^{+} - v_{j,k+\frac{1}{2}}^{+}}{b_{j,k+\frac{1}{2}}^{+} - b_{j,k+\frac{1}{2}}^{-}} \cdot h_{j,k+\frac{1}{2}}^{+} \rho_{j,k+\frac{1}{2}}^{+} \\
&+ \left[\frac{1}{8} - \mu_{j,k}^{n} b_{j,k+\frac{1}{2}}^{+} \cdot \frac{v_{j,k+\frac{1}{2}}^{-} - b_{j,k+\frac{1}{2}}^{-}}{b_{j,k+\frac{1}{2}}^{+} - b_{j,k+\frac{1}{2}}^{-}} \right] h_{j,k+\frac{1}{2}}^{-} \rho_{j,k+\frac{1}{2}}^{-} \\
&+ \mu_{j,k}^{n} b_{j,k-\frac{1}{2}}^{+} \cdot \frac{v_{j,k-\frac{1}{2}}^{-} - b_{j,k-\frac{1}{2}}^{-}}{b_{j,k-\frac{1}{2}}^{+} - b_{j,k-\frac{1}{2}}^{-}} \cdot h_{j,k-\frac{1}{2}}^{-} \rho_{j,k-\frac{1}{2}}^{-} \\
&+ \left[\frac{1}{8} + \mu_{j,k}^{n} b_{j,k-\frac{1}{2}}^{-} \cdot \frac{b_{j,k-\frac{1}{2}}^{+} - v_{j,k-\frac{1}{2}}^{+}}{b_{j,k-\frac{1}{2}}^{+} - b_{j,k-\frac{1}{2}}^{-}} \right] h_{j,k-\frac{1}{2}}^{+} \rho_{j,k-\frac{1}{2}}^{+} \\
&+ \frac{1}{8} \left[\frac{h_{j+\frac{1}{2},k}^{-} \rho_{j-\frac{1}{2},k-\frac{1}{4}}^{+} + h_{j+\frac{1}{2},k}^{-} \rho_{j-\frac{1}{2},k+\frac{1}{4}}^{+}}{2} \right] \\
&+ \frac{1}{8} \left[\frac{h_{j-\frac{1}{2},k-\frac{1}{4}}^{+} \rho_{j+\frac{1}{2},k}^{-} + h_{j-\frac{1}{2},k+\frac{1}{4}}^{+} \rho_{j+\frac{1}{2},k}^{-}}{2} \right] \\
&+ \frac{1}{8} \left[\frac{h_{j-\frac{1}{2},k-\frac{1}{4}}^{+} \rho_{j-\frac{1}{2},k+\frac{1}{4}}^{+} + h_{j-\frac{1}{2},k+\frac{1}{4}}^{+} \rho_{j-\frac{1}{2},k-\frac{1}{4}}^{+}}{4} \right]. \qquad (4.3.33)
\end{aligned}
$$

From (4.3.12) and §4.3.3.1 which guarantee the positivity of the reconstructed point values of h and ρ at the boundaries, the last two terms in (4.3.33) are nonnegative. The other terms are also nonnegative similar to those in (4.3.28). Since both $h_{j,k}^{n+1}$ and $\overline{(h\rho)}_{j,k}^{n+1}$ are nonnegative, thus $\rho_{j,k}^{n+1} = \overline{(h\rho)}_{j,k}^{n+1}/h_{j,k}^{n+1}$ is nonnegative as well.

We use the definition of the local speeds of propagation in (4.3.17), to satisfy the following CFL-type condition:

$$\Delta t \leq \frac{1}{8}\min\left[\min_{j,k}\left\{\frac{\Delta x_{j,k}}{\max\limits_{(\alpha,\beta)}\left[\max\left\{a^+_{\alpha,\beta},-a^-_{\alpha,\beta}\right\}\right]}\right\},\ \min_{j,k}\left\{\frac{\Delta y_{j,k}}{\max\limits_{(\gamma,\delta)}\left[\max\left\{b^+_{\gamma,\delta},-b^-_{\gamma,\delta}\right\}\right]}\right\}\right],$$

where

$$(\alpha,\beta)\in\left\{(j-\frac{1}{2},k-\frac{1}{4}),(j-\frac{1}{2},k+\frac{1}{4}),(j+\frac{1}{2},k)\right\}$$

and

$$(\gamma,\delta)\in\left\{(j,k-\frac{1}{2}),(j,k+\frac{1}{2})\right\}$$

for the configuration considered in Figure 4.2.

In all of our numerical experiments, we have used the three-stage third-order SSP Runge-Kutta solver. Note that the above positivity preserving proof is valid not only for the forward Euler time discretization, but for any strong stability preserving ODE solver (see, e.g., [30, 31]) as well.

4.3.8 Quadtree grid adaptivity

At the new time level $t = t^{n+1}$ the quadtree grid should be locally either refined or coarsened for the next timestep. To this end, we first compute the slopes $\{(w_x)_{j,k}^{n+1}\}$ and $\{(w_y)_{j,k}^{n+1}\}$, and $\{(\rho_x)_{j,k}^{n+1}\}$ and $\{(\rho_y)_{j,k}^{n+1}\}$ on the old grid (which we denote by $\{C_{j,k}^{\text{old}}\}$) according to §4.3.3 and then select the centers of those cells $C_{j,k}^{\text{old}}$, at which (see [28]),

$$(w_x)_{j,k}^{n+1}\geq C_{w,\,\text{seed}}\quad\text{or}\quad(w_y)_{j,k}^{n+1}\geq C_{w,\,\text{seed}},\tag{4.3.34}$$

and

$$(\rho_x)_{j,k}^{n+1}\geq C_{\rho,\,\text{seed}}\quad\text{or}\quad(\rho_y)_{j,k}^{n+1}\geq C_{\rho,\,\text{seed}}.\tag{4.3.35}$$

We denote the required seeding points to generate the new grid by $\{C^{\text{new}}_{j,k}\}$. In (4.3.34) and (4.3.35), $C_{w,\,\text{seed}}$ and $C_{\rho,\,\text{seed}}$ are constants that depend on the problem at hand, that is, on such factors as the maximum level of quadtree, Froude number, bottom topography function and/or boundary conditions.

When the mesh is locally refined or coarsened, the solution realized at the end of the evolution step in terms of the computed cell averages $\left\{\left(\overline{\mathscr{U}}^{\,n+1}_{j,k}\right)_{\text{old}}\right\}$ over the grid $\{C^{\text{old}}_{j,k}\}$, should be projected onto the new grid $\{C^{\text{new}}_{j,k}\}$ in a conservative manner according to the following three possible cases.

Case 1: If $C^{\text{new}}_{j,k} = C^{\text{old}}_{j',k'}$ for some (j',k'), that is, if the cell $C^{\text{old}}_{j',k'}$ does not need to be refined/coarsened, then

$$\left(\overline{\mathscr{U}}^{\,n+1}_{j,k}\right)_{\text{new}} = \left(\overline{\mathscr{U}}^{\,n+1}_{j',k'}\right)_{\text{old}}.$$

Case 2: If $C^{\text{new}}_{j,k} \in \mathscr{C}^{\ell+p}$ is a "child" cell of $C^{\text{old}}_{j',k'} \in \mathscr{C}^{\ell}$ for some j', k' and $p>0$ (that is, if the cell $C^{\text{old}}_{j',k'}$ was refined and $C^{\text{new}}_{j,k} \subset C^{\text{old}}_{j',k'}$), then

$$\left(\overline{\mathscr{U}}^{\,n+1}_{j,k}\right)_{\text{new}} = \left(\overline{\mathscr{U}}^{\,n+1}_{j',k'}\right)_{\text{old}} + \left((\mathscr{U}_x)^{n+1}_{j',k'}\right)_{\text{old}}\left[x^{\text{new}}_{j} - x^{\text{old}}_{j'}\right] + \left((\mathscr{U}_y)^{n+1}_{j',k'}\right)_{\text{old}}\left[y^{\text{new}}_{k} - y^{\text{old}}_{k'}\right].$$

Case 3: If $C^{\text{new}}_{j,k} \in \mathscr{C}^{\ell-p}$ is a "parent" cell of $C^{\text{old}}_{j',k'} \in \mathscr{C}^{\ell}$ for some j', k' and $p>0$ (that is, if the cell $C^{\text{old}}_{j',k'}$ was coarsened and $C^{\text{new}}_{j,k} \supset C^{\text{old}}_{j',k'}$), then

$$\left(\overline{\mathscr{U}}^{\,n+1}_{j,k}\right)_{\text{new}} = \frac{1}{4^p}\sum_{j'',k'':\,C^{\text{old}}_{j'',k''}\subset C^{\text{new}}_{j,k}}\sum \left(\overline{\mathscr{U}}^{\,n+1}_{j'',k''}\right)_{\text{old}}.$$

4.4 Numerical experiments

In this section, we present four numerical examples in which the proposed scheme is tested. In all of the examples, we take $g = 1$ and $\rho_\circ = 997$.

4.4.1 Example 1. Circular dam break with constant density

In this example, we demonstrate the ability of the proposed central-upwind quadtree scheme to generate adaptive grids at each timestep and maintain symmetry. A circular water column collapses on a horizontal flat bottom topography 40×40

dimensions plane [24, 38], where,

$$w(x,y,0) = \begin{cases} 2.5, & (x-20)^2 + (y-20)^2 < 2.5^2, \\ 0.5, & \text{otherwise}, \end{cases}$$
$$u(x,y,0) = v(x,y,0) \equiv 0, \quad \rho(x,y,0) \equiv \rho_\circ.$$

Furthermore, we take $m = 9$ refinement levels of the quadtree grid and set $C_{w,\,\text{seed}} = 5 \times 10^{-4}$ in (4.3.34). The solution runs until the final time $t \approx 1.5$. We compare the water surface elevations at $t \approx 0.4$ and $t \approx 0.7$ with the computed solution from [24] in Figure 4.3. Water surface contours and the respective quadtree grids are illustrated in Figure 4.4. The quadtree grid starts with 2134 cells and ends with 42604 cells at $t \approx 1.5$. The results in Figure 4.4 show that the solution follows the same evolution in comparison with the obtained ones in [24, 38].

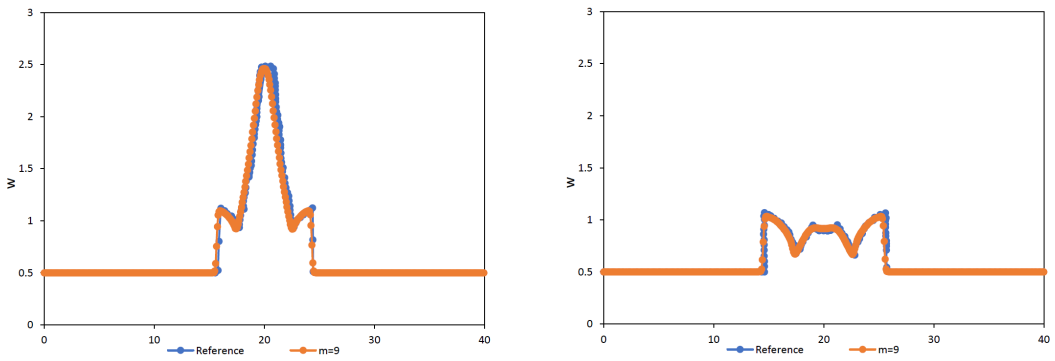

Figure 4.3: Example 1: Computed water surface $w(x,y,t)$ at $t \approx 0.4$ (left) and $t \approx 0.7$ (right) and comparison with the solution from [24].

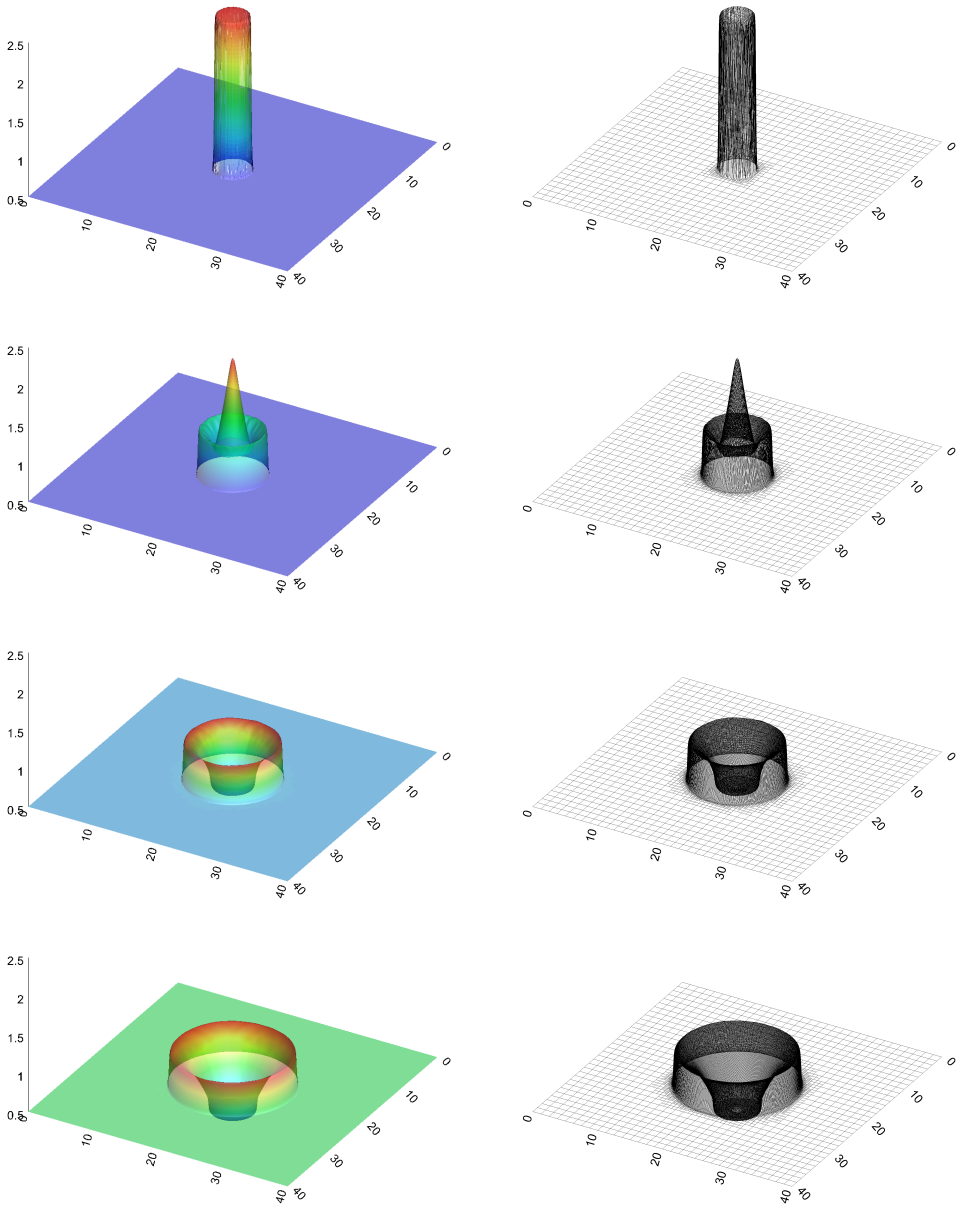

Figure 4.4: Example 1: Initial and computed water surface $w(x, y, t)$ (left column) and the corresponding quadtree grids (right column) for $t = 0$, and $t \approx 0.5$, 1 and 1.5 (from top to down) obtained using the well-balanced central-upwind quadtree scheme.

4.4.2 Example 2. Dam break with density discontinuity over a hump

This example is similar to the benchmark in [17, 38]. We show the capability of the central-upwind quadtree scheme to maintain the well-balanced property, symmetry, and to generate adaptive grids. We consider the computational domain to be $[0,2]\times[0,1]$ with the following initial conditions:

$$\rho(x,y,0)=\begin{cases}997, & x<1,\\ 1200, & x\geq 1,\end{cases}\qquad u(x,y,0)=v(x,y,0)\equiv 0,\quad w(x,y,0)\equiv 1,$$

and the given bottom topography

$$B(x,y)=0.8e^{-5(x-0.9)^2-50(y-0.5)^2}.$$

We set $C_{w,\,\text{seed}}=10^{-2}$ and $C_{\rho,\,\text{seed}}=10$ in (4.3.34) and (4.3.35), and $m=8$. A solid wall boundary condition is used at the top and bottom boundaries. For the sake of simplicity, we set the left and the right boundaries to Dirichlet boundary conditions. We run the solution up to the final time $t\approx 0.8$ with the non-well-balanced and well-balanced schemes. For the non-well-balanced scheme, the source approximations read as:

$$\overline{S}^{(2)}_{j,k}=-\frac{\overline{g(h\rho)}_{j,k}}{\rho_\circ\,\Delta x_{j,k}}\left[\frac{B_{j+\frac12,k+\frac12}+B_{j+\frac12,k-\frac12}}{2}-\frac{B_{j-\frac12,k+\frac12}+B_{j-\frac12,k-\frac12}}{2}\right],$$
$$\overline{S}^{(3)}_{j,k}=-\frac{\overline{g(h\rho)}_{j,k}}{\rho_\circ\,\Delta x_{j,k}}\left[\frac{B_{j+\frac12,k+\frac12}+B_{j+\frac12,k-\frac12}}{2}-\frac{B_{j-\frac12,k+\frac12}+B_{j-\frac12,k-\frac12}}{2}\right].$$

Water surface contours and the respective quadtree grids of the solution of the non-well-balanced scheme are demonstrated in Figure 4.5. The quadtree grid starts with 1184 cells and ends with 27749 cells at $t\approx 0.8$. The well-balanced solution is presented in Figure 4.6 where the quadtree has a minimum of 1184 and a maximum of 18497 cells. Utilizing the well-balanced scheme reduces the number of cells in the quadtree grid; therefore, the computational cost is reduced and the nonphysical oscillations are eliminated.

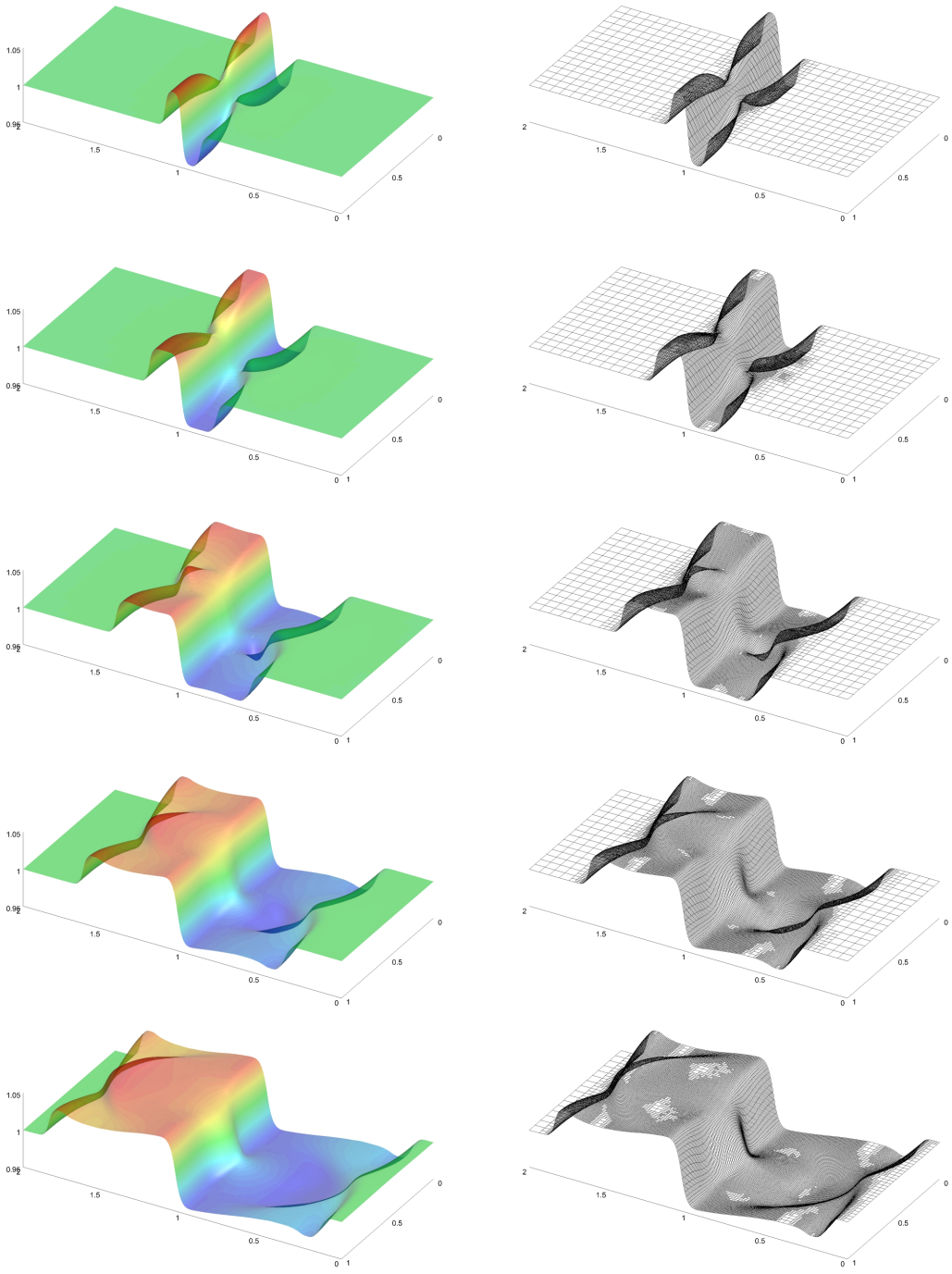

Figure 4.5: Example 2: Computed water surface $w(x, y, t)$ (left column) and the corresponding quadtree grids (right column) for $t \approx 0.1$, 0.2, 0.4, 0.6 and 0.8 (from top to down) obtained using the non-well-balanced central-upwind quadtree scheme.

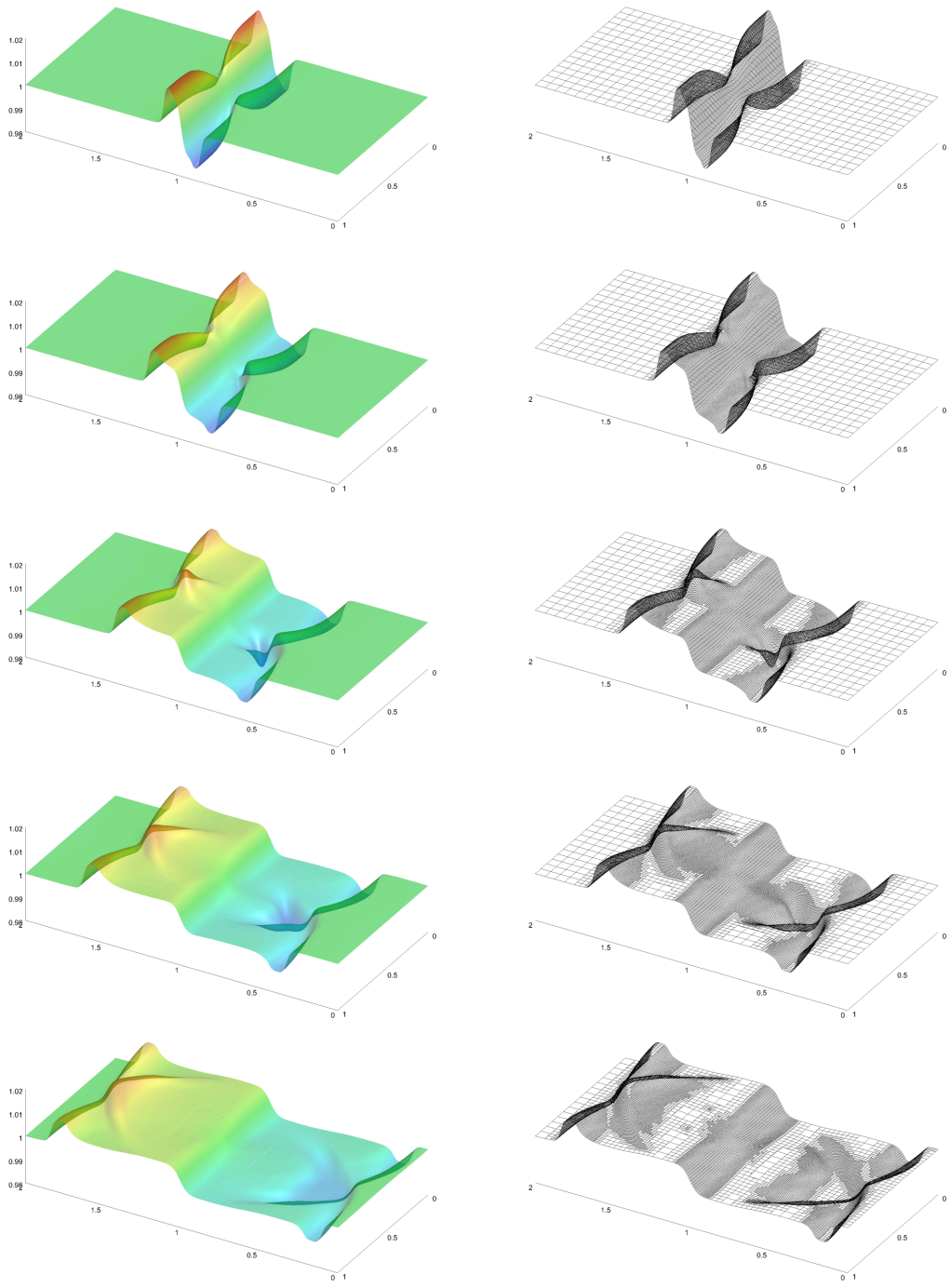

Figure 4.6: Example 2: Computed water surface $w(x, y, t)$ (left column) and the corresponding quadtree grids (right column) for $t \approx 0.1$, 0.2, 0.4, 0.6 and 0.8 (from top to down) obtained using the well-balanced central-upwind quadtree scheme.

4.4.3 Example 3. Small perturbations of a stationary steady state solution

This numerical example tests the capability of the proposed scheme to capture small perturbations of a steady state solution [15, 16, 28, 43, 55, 63]. We choose a computational domain $[-2,2]\times[0,1]$ to prevent complicated boundary conditions. The initial conditions are

$$w(x,y,0)=\begin{cases}1.01, & 0.05<x<0.15,\\ 1, & \text{otherwise},\end{cases}\qquad u(x,y,0)=v(x,y,0)\equiv 0,$$

$$\rho(x,y,0)=\begin{cases}1007, & 0.05<x<0.15,\\ \rho_\circ, & \text{otherwise},\end{cases}$$

and the given bottom topography in Example 2.

We set similar boundary conditions of Example 2 for this test. $m=9$ is taken and we set $C_{w,\,\text{seed}}=10^{-2}$ and $C_{\rho,\,\text{seed}}=10$ in (4.3.34) and (4.3.35). The non-well-balanced solution is computed until the final time $t=1.8$ and plot the snapshots of w (left) and the quadtree grids (right) at times $t=0.6$, 0.9, 1.2, 1.5 and 1.8 in the domain of $[0,2]\times[0,1]$ in Figure 4.7. The quadtree grid starts with 2530 cells and reaches a maximum number of 13804 cells during the time evolution. The-well-balanced solution is illustrated in Figure 4.8, respectively. In this solution the number of cells reaches the maximum of 10222. Figure 4.8 demonstrates that the proposed well-balanced central-upwind quadtree scheme accurately captures a small perturbation of the "lake-at-rest" steady state and that the symmetry of the solution is preserved (see Figure B.6 for the computed solution of $\rho(x,y,t)$).

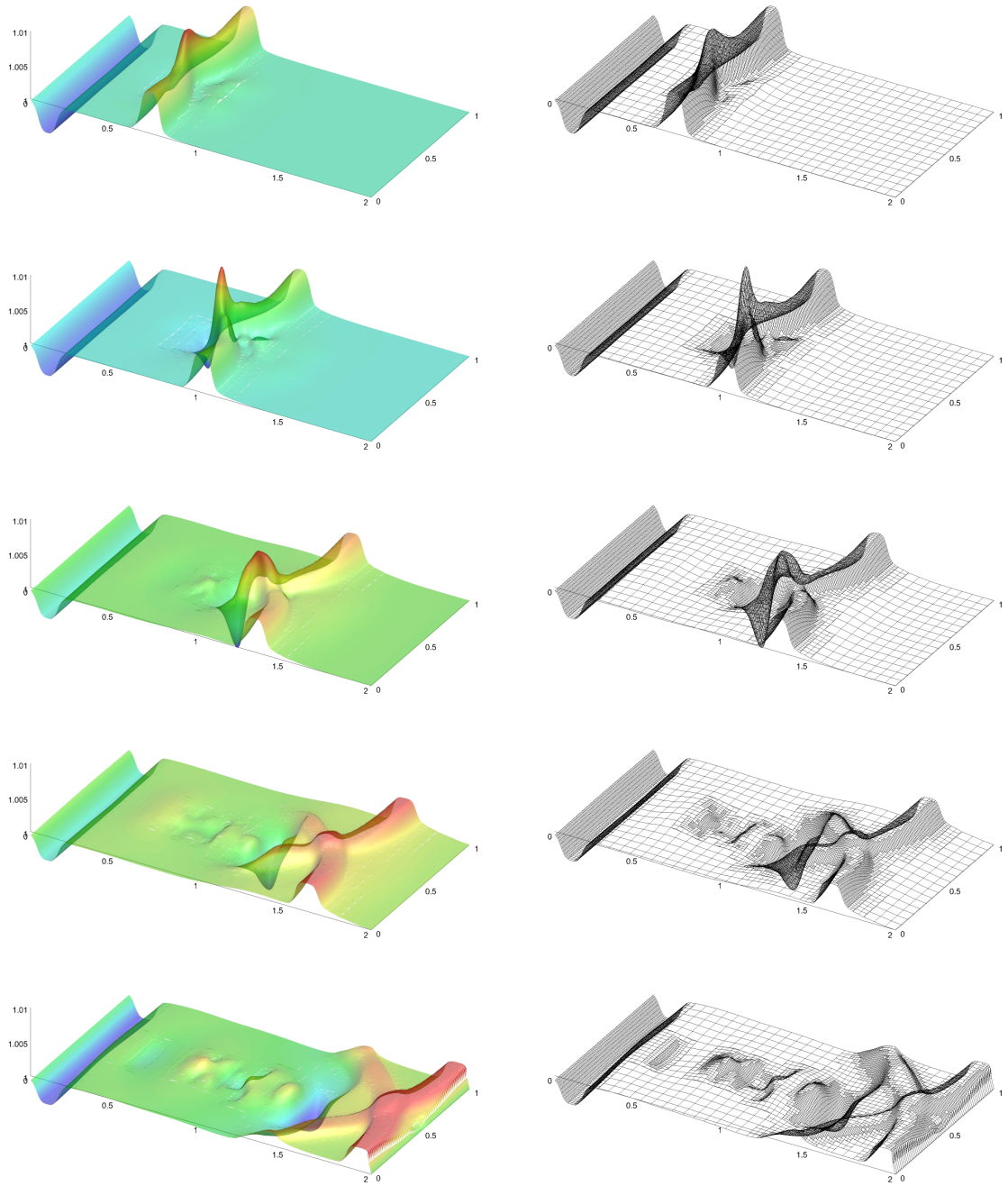

Figure 4.7: Example 3: Computed water surface $w(x, y, t)$ (left column) and the corresponding quadtree grids (right column) for $t = 0.6$, 0.9, 1.2, 1.5 and 1.8 (from top to down) obtained using the non-well-balanced central-upwind quadtree scheme.

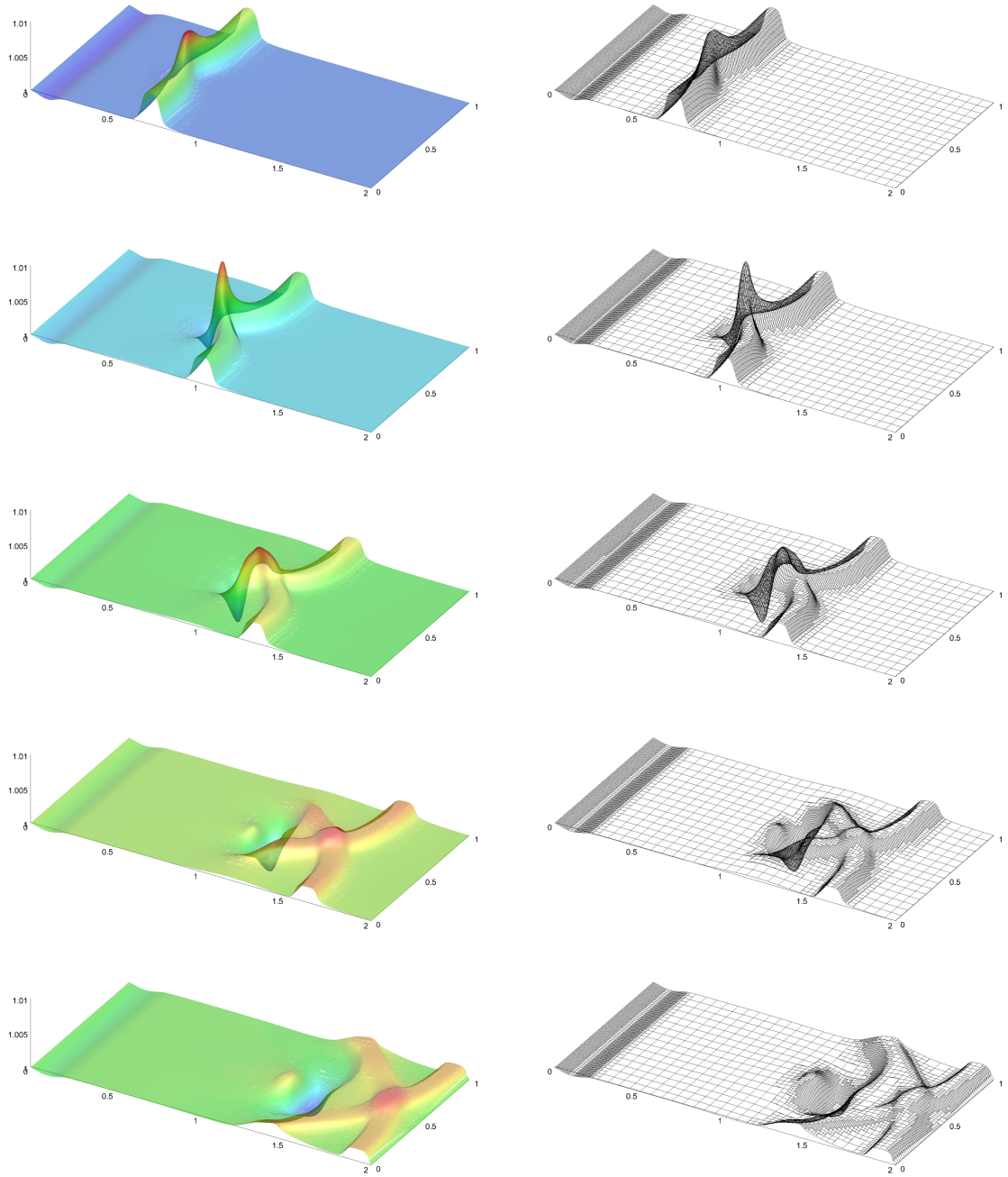

Figure 4.8: Example 3: Computed water surface $w(x, y, t)$ (left column) and the corresponding quadtree grids (right column) for $t = 0.6$, 0.9, 1.2, 1.5 and 1.8 (from top to down) obtained using the well-balanced central-upwind quadtree scheme.

4.4.4 Example 4. Sudden contraction with variable density inflow

The last example is a modification of the benchmark in [28, 37]; also see [16, 15]. The purpose of this example is to demonstrate the positivity preserving property of the proposed scheme.

We consider an open channel with a sudden contraction. The geometry of the channel is established on its contraction, where

$$y_b(x) = \begin{cases} 0.5, & x \le 1, \\ 0.4, & \text{otherwise.} \end{cases}$$

The computational domain is $[0,3] \times [0.5 - y_b(x), 0.5 + y_b(x)]$. Solid wall boundary conditions are imposed at all of the boundaries except for part of the left inflow boundary with $u(0, y_i, t) \equiv 2$ and $\rho(0, y_i, t) \equiv 1007$, where $y_i \in [0.4, 0.6]$. In addition the right boundary is a zero-order extrapolation one. The following initial conditions are prescribed:

$$w(x, y, 0) \equiv 1, \quad u(x, y, 0) = v(x, y, 0) \equiv 0, \quad \rho(x, y, 0) \equiv \rho_\circ.$$

In this example, we take $m = 8$ refinement levels of the quadtree grid and set $C_{w,\,\text{seed}} = 2$ and $C_{\rho,\,\text{seed}} = 20$ in (4.3.34) and (4.3.35). We compute the solution with the bottom topography given in the Example 2, where the water height at the top of the humps is quite shallow which makes it a good example to test the positivity preserving property.

We compute the solution until the final time $t = 1.9$ and plot the evolution of w and ρ at times $t \approx 0.4$, 0.8, 1.2, 1.6 and 1.9 in Figures 4.9. The quadtree grid in this solution starts with a minimum of $m = 298$ and reaches a maximum of 9928 cells. As one can see, the proposed central-upwind quadtree scheme preserves positivity of the computed water depth and density.

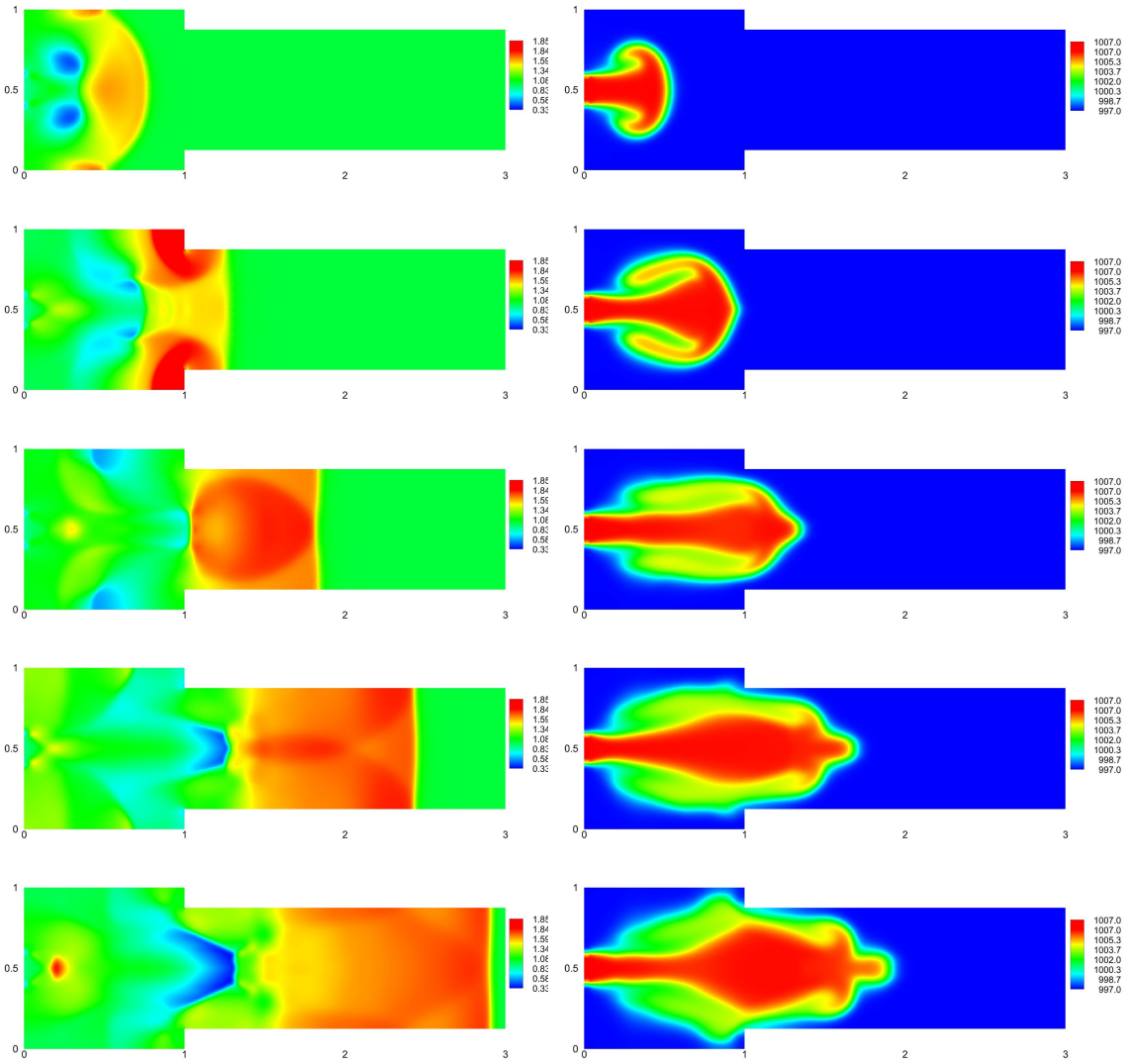

Figure 4.9: Example 4: Evolution of water surface $w(x, y, t)$ (left column) and density (right column) for $t \approx 0.4$, 0.8, 1.2, 1.6 and 1.9 (from top to down) obtained using the well-balanced central-upwind quadtree scheme.

Chapter 5

Summary and conclusion

The shallow water system is one of the most important systems of equations in the field of hydrodynamics. In this study, a robust and efficient central-upwind scheme over quadtree grids that balances the fluxes and the source terms has been constructed. The advantage of the proposed well-balanced scheme is its capability to reduce the computational cost. Furthermore, the proposed scheme is positivity preserving, capable of solving the shallow water equation on an irregular bottom topography.

In this thesis, the level of refinement was chosen separately for each benchmark test. The computational cost was increased where m was increased. The minimum level of quadtree can also be chosen based on the desired accuracy and computational cost. The constants $C_{w,\,\text{seed}}$ and $C_{\rho,\,\text{seed}}$ were found from trial and error. Although for the case of $C_{w,\,\text{seed}}$, the ratio of wave heights and smallest cell length can be utilized to find the best constant value.

In Chapter 3, an adaptive, well-balanced, positivity preserving central-upwind scheme over quadtree grids for the shallow water equations over irregular bottom topography has been presented. Six numerical experiments have been performed in order to verify the accuracy and robustness of the proposed scheme. The first numerical benchmark test has addressed the accuracy of the scheme. The second numerical example has focused on the positivity and symmetry preserving as well as adaptability of the scheme. The third and fourth numerical examples have demonstrated the well-balanced property, symmetry preserving and adaptability features of the proposed method. The fifth test has focused on the capability of the scheme

to model flows over a discontinuous bottom topography. The last numerical example has demonstrated the positivity preserving and shock-capturing features of the method. The obtained results show that the proposed central-upwind quadtree scheme can improve the performance and efficiency of calculations compared with regular Cartesian grids.

In Chapter 4, we extend the proposed scheme, where an adaptive, well-balanced, positivity preserving central-upwind scheme for variable density shallow water equations over quadtree grids and irregular bottom topography has been presented. We study different aspects of the scheme with regards to the water surface and the water depth, the velocities, and the density. In addition, the scheme is able to eliminate nonphysical oscillations that arise from one of the conservative variables. Four numerical examples have been performed in order to verify the robustness and accuracy of the proposed scheme. The benchmarks show symmetry preserving, well-balanced property, positivity preserving, adaptability of the coupled system as well as the capability of the scheme to capture small perturbations. Similar to Chapter 3, the obtained results show that the proposed central-upwind quadtree scheme can improve the performance and efficiency of calculations in comparison to non-well-balanced schemes and regular Cartesian grids.

5.1 Suggestions for future works

Several future works can be suggested based on this work. In order to improve the proposed scheme and address the inability of quadtree grids to properly model curvilinear boundaries, this work can be extended to enhanced quadtree grids with cut-cell boundary control volumes. Moreover, the system can be coupled to other equations such as sediment transport equations. Other source terms such as friction can be added to the current source terms in order to increase the applications of the proposed scheme. Furthermore, other properties such as dry and wet/dry properties can also be added to the proposed scheme.

Bibliography

[1] K. Aizawa, K. Motomura, S. Kimura, R. Kadowaki, and J. Fan. Constant time neighbor finding in quadtrees: An experimental result. In *3rd International Symposium on Communications, Control and Signal Processing, 2008. ISCCSP 2008.*, pages 505–510. IEEE, 2008.

[2] H. An and S. Yu. Well-balanced shallow water flow simulation on quadtree cut cell grids. *Adv. Water Resour.*, 39:60–70, 2012.

[3] E. Audusse, F. Bouchut, M.-O. Bristeau, R. Klein, and B. Perthame. A fast and stable well-balanced scheme with hydrostatic reconstruction for shallow water flows. *SIAM J. Sci. Comput.*, 25:2050–2065, 2004.

[4] E. Audusse and M.-O. Bristeau. A well-balanced positivity preserving "second-order" scheme for shallow water flows on unstructured meshes. *J. Comput. Phys.*, 206(1):311–333, 2005.

[5] A. Beljadid, A. Mohammadian, and A. Kurganov. Well-balanced positivity preserving cell-vertex central-upwind scheme for shallow water flows. *Comput. & Fluids*, 136:193–206, 2016.

[6] M. Ben-Artzi and J. Falcovitz. A second-order godunov-type scheme for compressible fluid dynamics. *Journal of Computational Physics*, 55(1):1 – 32, 1984.

[7] M. Berger, M. Aftosmis, and S. Muman. Analysis of slope limiters on irregular grids. In *43rd AIAA Aerospace Sciences Meeting and Exhibit*, pages 1–22, 2005.

[8] M. Bern, D. Eppstein, and S.-H. Teng. Parallel construction of quadtrees and quality triangulations. *Internat. J. Comput. Geom. Appl.*, 9(6):517–532, 1999.

[9] Andrew Bernstein, Alina Chertock, and Alexander Kurganov. Central-upwind scheme for shallow water equations with discontinuous bottom topography. *Bulletin of the Brazilian Mathematical Society*, 47(1):91–103, 2016.

[10] C. Berthon and F. Marche. A positive preserving high order VFRoe scheme for shallow water equations: a class of relaxation schemes. *SIAM J. Sci. Comput.*, 30(5):2587–2612, 2008.

[11] A. Bollermann, G. Chen, A. Kurganov, and S. Noelle. A well-balanced reconstruction of wet/dry fronts for the shallow water equations. *J. Sci. Comput.*, 56(2):267–290, 2013.

[12] A. Bollermann, S. Noelle, and M. Lukáčová-Medviďová. Finite volume evolution Galerkin methods for the shallow water equations with dry beds. *Commun. Comput. Phys.*, 10(2):371–404, 2011.

[13] a. G. L. Borthwick, S. Cruz Leon, and J. Jozsa. Adaptive quadtree model of shallow-flow hydrodynamics. *Journal of Hydraulic Research*, 39(4):413–424, 2001.

[14] A. G. L. Borthwick, R. D. Marchant, and G. J. M. Copeland. Adaptive hierarchical grid model of water-borne pollutant dispersion. *Adv. Water Resour.*, 23(8):849–865, 2000.

[15] S. Bryson, Y. Epshteyn, A. Kurganov, and G. Petrova. Well-balanced positivity preserving central-upwind scheme on triangular grids for the Saint-Venant system. *M2AN Math. Model. Numer. Anal.*, 45(3):423–446, 2011.

[16] S. Bryson and D. Levy. Balanced central schemes for the shallow water equations on unstructured grids. *SIAM J. Sci. Comput.*, 27:532–552, 2005.

[17] J. Burguete, P. García-Navarro, and J. Murillo. Preserving bounded and conservative solutions of transport in one-dimensional shallow-water flow with upwind numerical schemes: Application to fertigation and solute transport in rivers.

International Journal for Numerical Methods in Fluids, 56(9):1731–1764, mar 2008.

[18] Manuel J. Castro, Alberto Pardo Milanés, and Carlos Parés. Well-balanced numerical schemes based on a generalized hydrostatic reconstruction technique. *Mathematical Models and Methods in Applied Sciences*, 17(12):2055–2113, 2007.

[19] Alina Chertock, Alexander Kurganov, and Yu Liu. Central-upwind schemes for the system of shallow water equations with horizontal temperature gradients. *Numerische Mathematik*, 127(4):595–639, aug 2014.

[20] A. J. C. de Saint-Venant. Thèorie du mouvement non-permanent des eaux, avec application aux crues des rivière at à l'introduction des marèes dans leur lit. *C.R. Acad. Sci. Paris*, 73:147–154, 237–240, 1871.

[21] C.P. Dullemond. Advection algorithms II. Flux conservation, subgrid models and flux limiters. In *Numerical Fluid Dynamics*, pages 59–72. 2008.

[22] Michael Dumbser and Vincenzo Casulli. A staggered semi-implicit spectral discontinuous galerkin scheme for the shallow water equations. *Applied Mathematics and Computation*, 219(15):8057 – 8077, 2013.

[23] Toro E.F., Millington R.C., and Nejad L.A.M. Towards Very High Order Godunov Schemes. In *Godunov Methods*. Springer, 2001.

[24] Eleuterio F Toro. *Shock-capturing methods for free-surface shallow fluids*. Wiley and Sons Ltd, 2001.

[25] K. O. Friedrichs. Symmetric hyperbolic linear differential equations. *Communications on Pure and Applied Mathematics*, 7(2):345–392, 1954.

[26] J. M. Gallardo, C. Parés, and M. Castro. On a well-balanced high-order finite volume scheme for shallow water equations with topography and dry areas. *J. Comput. Phys.*, 227(1):574–601, 2007.

[27] Thierry Gallouët, Jean Marc Hérard, and Nicolas Seguin. Some approximate godunov schemes to compute shallow-water equations with topography. *Computers and Fluids*, 32(4):479–513, 2003.

[28] M. A. Ghazizadeh, A. Mohammadian, and A. Kurganov. An adaptive well-balanced positivity preserving central-upwind scheme on quadtree grids for shallow water equations. *Preprint January 2020, Ready for publication*, 2020.

[29] S. K. Godunov. A difference method for numerical calculation of discontinuous solutions of the equations of hydrodynamics. *Mat. Sb. (N.S.)*, 47(89):271–306, 1959.

[30] S. Gottlieb, D. Ketcheson, and C.-W. Shu. *Strong stability preserving Runge-Kutta and multistep time discretizations*. World Scientific Publishing Co. Pte. Ltd., Hackensack, NJ, 2011.

[31] S. Gottlieb, C.-W. Shu, and E. Tadmor. Strong stability-preserving high-order time discretization methods. *SIAM Rev.*, 43(1):89–112, 2001.

[32] D. M. Greaves and A. G. L. Borthwick. On the use of adaptive hierarchical meshes for numerical simulation of separated flows. *Internat. J. Numer. Methods Fluids*, 26(3):303–322, 1998.

[33] Deborah Greaves. A quadtree adaptive method for simulating fluid flows with moving interfaces. *Journal of Computational Physics*, 194(1):35–56, 2004.

[34] J. M. Greenberg and A. Y. Leroux. A well-balanced scheme for the numerical processing of source terms in hyperbolic equations. *SIAM Journal on Numerical Analysis*, 33(1):1–16, 1996.

[35] Jian Guo and Alistair G L Borthwick. Fluids Lattice Boltzmann method for variable density shallow water equations. *Computers and Fluids*, 49(1):146–149, 2011.

[36] Charles Hirsch. General Properties and High-Resolution Numerical Schemes. In *Numerical Computation of Internal and External Flows*, pages 337–409. Elsevier, 2007.

[37] M. E. Hubbard. On the accuracy of one-dimensional models of steady converging/diverging open channel flows. *Internat. J. Numer. Methods Fluids*, 35:785–808, 2001.

[38] Long Jiang, Alistair G.L. Borthwick, Tamás Krámer, and János Józsa. Variable density bore interaction with block obstacles. *International Journal of Computational Fluid Dynamics*, 25(4):223–237, apr 2011.

[39] Shi Jin. A Steady-State Capturing Method for Hyperbolic Systems with Geometrical Source Terms. *Mathematical Modelling and Numerical Analysis*, 35(4):631–645, 2001.

[40] Georges Kesserwani and Qiuhua Liang. Dynamically adaptive grid based discontinuous Galerkin shallow water model. *Advances in Water Resources*, 37:23–39, 2012.

[41] Sepideh Khorshid, Abdolmajid Mohammadian, and Ioan Nistor. Extension of a well-balanced central upwind scheme for variable density shallow water flow equations on triangular grids. *Computers and Fluids*, 156:441–448, 2017.

[42] A. Kurganov. Finite-volume schemes for shallow-water equations. *Acta Numer.*, 27:289–351, 2018.

[43] A. Kurganov and D. Levy. Central-upwind schemes for the Saint-Venant system. *M2AN Math. Model. Numer. Anal.*, 36(3):397–425, 2002.

[44] A. Kurganov and C.-T. Lin. On the reduction of numerical dissipation in central-upwind schemes. *Commun. Comput. Phys.*, 2(1):141–163, 2007.

[45] A. Kurganov, S. Noelle, and G. Petrova. Semidiscrete central-upwind schemes for hyperbolic conservation laws and Hamilton-Jacobi equations. *SIAM J. Sci. Comput.*, 23(3):707–740, 2001.

[46] A. Kurganov and G. Petrova. A second-order well-balanced positivity preserving central-upwind scheme for the Saint-Venant system. *Commun. Math. Sci.*, 5(1):133–160, 2007.

[47] A. Kurganov, M. Prugger, and T. Wu. Second-order fully discrete central-upwind scheme for two-dimensional hyperbolic systems of conservation laws. *SIAM J. Sci. Comput.*, 39(3):A947–A965, 2017.

[48] A. Kurganov and E. Tadmor. New high-resolution central schemes for nonlinear conservation laws and convection-diffusion equations. *J. Comput. Phys.*, 160(1):241–282, 2000.

[49] A. Kurganov and E. Tadmor. Solution of two-dimensional riemann problems for gas dynamics without Riemann problem solvers. *Numer. Methods Partial Differential Equations*, 18:584–608, 2002.

[50] D. Kuzmin. On the design of general-purpose flux limiters for finite element schemes. I. Scalar convection. *J. Comput. Phys.*, 219(2):513–531, 2006.

[51] Peter D. Lax. Weak solutions of nonlinear hyperbolic equations and their numerical computation. *Communications on Pure and Applied Mathematics*, 7(1):159–193, 1954.

[52] W.-K. Lee, A. G. L. Borthwick, and P. H. Taylor. A fast adaptive quadtree scheme for a two-layer shallow water model. *J. Comput. Phys.*, 230(12):4848–4870, 2011.

[53] Philippe G. LeFloch and Mai Duc Thanh. A godunov-type method for the shallow water equations with discontinuous topography in the resonant regime. *Journal of Computational Physics*, 230(20):7631 – 7660, 2011.

[54] Feifei Zhang Leighton, Alistair G L Borthwick, and Paul H Taylor. 1-D numerical modelling of shallow flows with variable horizontal density. *International Journal for Numerical Methods in Fluids*, (April 2009):n/a–n/a, 2009.

[55] R. J. LeVeque. Balancing source terms and flux gradients in high-resolution Godunov methods: the quasi-steady wave-propagation algorithm. *J. Comput. Phys.*, 146(1):346–365, 1998.

[56] Jiequan Li and Guoxian Chen. The generalized riemann problem method for the shallow water equations with bottom topography. *International Journal for Numerical Methods in Engineering*, 65(6):834–862, 2006.

[57] Q Liang, A G L Borthwick, and G Stelling. Simulation of dam- and dyke-break hydrodynamics on dynamically adaptive quadtree grids. *International Journal for Numerical Methods in Fluids*, 46(September):127–162, 2004.

[58] Qiuhua Liang and Alistair G.L. Borthwick. Adaptive quadtree simulation of shallow flows with wet–dry fronts over complex topography. *Computers & Fluids*, 38(2):221–234, feb 2009.

[59] Qiuhua Liang, Jingming Hou, and Xilin Xia. Contradiction between the C-property and mass conservation in adaptive grid based shallow flow models : cause and solution. *International Journal for Numerical Methods in Fluids*, 78(February):17–36, 2015.

[60] Knut-andreas Lie and Sebastian Noelle. On the artificial compression method for second-order nonoscillatory central difference schemes for systems of conservation laws. *Society*, 24(4):1157–1174, 2003.

[61] G.-F. Lin, J.-S. Lai, and W.-D. Guo. Finite-volume component-wise TVD schemes for 2D shallow water equations. *Adv. Water Resour.*, 26(8):861–873, 2003.

[62] X. Liu, J. Albright, Y. Epshteyn, and A. Kurganov. Well-balanced positivity preserving central-upwind scheme with a novel wet/dry reconstruction on triangular grids for the Saint-Venant system. *J. Comput. Phys.*, 374:213–236, 2018.

[63] X. Liu, A. Mohammadian, A. Kurganov, and J. A. Infante Sedano. Well-balanced central-upwind scheme for a fully coupled shallow water system modeling flows over erodible bed. *J. Comput. Phys.*, 300:202–218, 2015.

[64] M. Lukáčová-Medvid'ová, S. Noelle, and M. Kraft. Well-balanced finite volume evolution galerkin methods for the shallow water equations. *Journal of Computational Physics*, 221(1):122 – 147, 2007.

[65] Victor Michel-dansac, Christophe Berthon, and Stéphane Clain. A well-balanced scheme for the shallow-water equations with topography. *Computers and Mathematics with Applications*, 72(3):568–593, 2016.

[66] D. Moore. The cost of balancing generalized quadtrees. In *Proceedings of the third ACM symposium on Solid modeling and applications*, pages 305–312, New York, New York, USA, 1995. ACM Press.

[67] Sebastian Noelle, Normann Pankratz, Gabriella Puppo, and Jostein R. Natvig. Well-balanced finite volume schemes of arbitrary order of accuracy for shallow water flows. *Journal of Computational Physics*, 213(2):474 – 499, 2006.

[68] Carlos. Parés. Numerical methods for nonconservative hyperbolic systems: a theoretical framework. *SIAM Journal on Numerical Analysis*, 44(1):300–321, 2006.

[69] F. Pascal and J. L. Marechal. Fast adaptive quadtree mesh generation. In *7th International Meshing Roundtable*, pages 211–224. Citeseer, 1998.

[70] S. Popinet. Gerris: a tree-based adaptive solver for the incompressible Euler equations in complex geometries. *J. Comput. Phys.*, 190(2):572–600, 2003.

[71] S. Popinet, R. M. Gorman, G. J. Rickard, and H. L. Tolman. A quadtree-adaptive spectral wave model. *Ocean Model.*, 34(1-2):36–49, 2010.

[72] Stéphane Popinet. Quadtree-adaptive tsunami modelling. *Ocean Dynamics*, 61(9):1261–1285, 2011.

[73] Stéphane Popinet and Graham Rickard. A tree-based solver for adaptive ocean modelling. *Ocean Modelling*, 16(3-4):224–249, 2007.

[74] M. Ricchiuto. An explicit residual based approach for shallow water flows. *J. Comput. Phys.*, 280:306–344, 2015.

[75] M. Rodriguez-Paz and J. Bonet. A corrected smooth particle hydrodynamics formulation of the shallow-water equations. *Comput. & Structures*, 83(17-18):1396–1410, 2005.

[76] Roe P. L. Approximate Riemann Solvers, Parameter Vectors, and Difference Schemes. *Journal of Computational Physics*, 43:357–372, 1981.

[77] B. Rogers, M. Fujihara, and A. G. L. Borthwick. Adaptive Q-tree Godunov-type scheme for shallow water equations. *Internat. J. Numer. Methods Fluids*, 35(3):247–280, 2001.

[78] Giovanni Russo. Central schemes for conservation laws with application to shallow water equations. In Salvatore Rionero and Giovanni Romano, editors, *Trends and Applications of Mathematics to Mechanics*, pages 225–246, Milano, 2005. Springer Milan.

[79] H. Samet. Neighbor finding techniques for images represented by quadtrees. *Comput. Vision Graph.*, 18(1):37–57, 1982.

[80] H. Samet. Algorithms for the conversion of quadtrees to rasters. *Comput. Vision Graph.*, 26(1):1–16, 1984.

[81] H. Samet. The quadtree and related hierarchical data structures. *Comput. Surveys*, 16(2):187–260, 1984.

[82] H. Samet. *Foundations of Multidimensional and Metric Data Structures*. Morgan Kaufmann, first edition, 2006.

[83] H. Samet and C. A Shaffer. A model for the analysis of neighbor finding in pointer-based quadtrees. *IEEE T. Pattern Anal.*, PAMI-7(6):717–720, 1985.

[84] J. Sankaranarayanan, H. Samet, and A. Varshney. A fast all nearest neighbor algorithm for applications involving large point-clouds. *Comput. Graph.*, 31(2):157–174, 2007.

[85] H. Shirkhani, A. Mohammadian, O. Seidou, and A. Kurganov. A well-balanced positivity-preserving central-upwind scheme for shallow water equations on unstructured quadrilateral grids. *Comput. & Fluids*, 126:25–40, 2016.

[86] Eitan Tadmor Sigal Gottlieb, Chi-Wang Shu. Strong Stability-Preserving High-Order Time Discretization Methods. *Society for Industrial and Applied Mathematics*, 43(1):89–112, 2001.

[87] Chi-Wang Shu Sigal Gottlieb, David I. Ketcheson. *Strong stability preserving Runge-Kutta and multistep time discretizations*. World Scientific, Singapore, 2011.

[88] P. K. Sweby. High resolution schemes using flux limiters for hyperbolic conservation laws. *SIAM J. Numer. Anal.*, 21(5):995–1011, 1984.

[89] Eleuterio F. Toro and Pilar Garcia-Navarro. Godunov-type methods for free-surface shallow flows: A review. *Journal of Hydraulic Research*, 45(6):736–751, 2007.

[90] P. M. Vaidya. An $O(n \log n)$ algorithm for the all-nearest-neighbors problem. *Discrete Comput. Geom.*, 4(2):101–115, 1989.

[91] Bram van Leer. Towards the ultimate conservative difference scheme. v. a second-order sequel to godunov's method. *Journal of Computational Physics*, 32(1):101 – 136, 1979.

[92] K. F. C. Yiu, D. M. Greaves, S. Cruz, A. Saalehi, and A. G. L. Borthwick. Quadtree grid generation: Information handling, boundary fitting and CFD applications. *Comput. & Fluids*, 25(8):759–769, 1996.

Appendix A

Finding neighbours in quadtree grids

In order to regularize a non-regularized quadtree grid we need to find those cells that have adjacent cells with a level difference of greater than one to cell C. The algorithm below shows how to find the adjacent neighbouring cells of C (x and y are the central coordinate of cell C):

Step 1. Find cell C with the level of $l_c = m$ (maximum level in the quadtree).

Step 2. Create a set of cells (called **S**) without cell C. Remove cells from **S** that $l_s \geq l_c - 1$.

Step 3. To find the northern neighbour,

- ⋆ Remove the cells from **S** with $y < y_c$.
- ⋆ Remove the cells from **S** with $x < x_c - \frac{1}{2^{l_s+1}}$ or $x < x_c + \frac{1}{2^{l_s+1}}$.

Step 4. To find the eastern neighbour,

- ⋆ Remove the cells from **S** (from **Step 2**) with $x < x_c$.
- ⋆ Remove the cells from **S** (from **Step 2**) with $y > y_c - \frac{1}{2^{l_s+1}}$ or $y < y_c + \frac{1}{2^{l_s+1}}$.

Step 5. To find the southern neighbour,

- ⋆ Remove the cells from **S** (from **Step 2**) with $y > y_c$.
- ⋆ Remove the cells from **S** (from **Step 2**) with $x < x_c - \frac{1}{2^{l_s+1}}$ or $x > x_c + \frac{1}{2^{l_s+1}}$.

Step 6. To find the western neighbour,

- ⋆ Remove the cells from **S** (from **Step 2**) with $x > x_c$.
- ⋆ Remove the cells from **S** (from **Step 2**) with $y > y_c - \frac{1}{2^{l_s+1}}$ or $y < y_c + \frac{1}{2^{l_s+1}}$.

Step 7. Repeat all the steps with quadtree level of $l_c - 1$.

A similar algorithm is employed to find the diagonally neighbouring cells. We need to mention that this algorithm may not be the best and the most efficient way to find the neighbouring cells. The algorithm was chosen as it was the fastest and easiest one to implement. The focus of this thesis is not how to efficiently generate quadtree grids.

Appendix B

Extra benchmark tests and figures

In this appendix an extra benchmark test and some figures from other studies are presented.

Example 1. Flows in a converging-diverging channel

This example is based on the benchmark in [37]. The purpose of this example is to show the ability of the adaptive quadtree scheme to capture the shocks in supercritical flows (see [16, 15]). We apply the proposed scheme in a converging-diverging open channel. The geometry of the channel is established on its breadth where

$$w(x,y,0) = \begin{cases} 0.5 - 0.5(1-d)\cos^2(\pi(x-1.5)), & |x-1.5| \leq 0.5, \\ 0.5, & \text{otherwise}, \end{cases}$$

and $d = 0.9$, which is the minimum channel breadth. The computational domain is $[0,3] \times [-y_b(x) + 0.5, y_b(x) + 0.5]$. We utilize the following initial condition

$$w(x,y,0) = 1, \qquad u(x,y,0) = 2, \qquad v(x,y,0) = 0.$$

Both the top and the bottom boundaries are solid walls and the left x-boundary is an inflow boundary with $u(0,y,t) = 2$, and the right boundary is a zero-order outflow one. We compute the solution with a flat topography up to $t = 2$ where the flow almost reaches to steady-state. Figure B.1 shows the initial quadtree grid. The

grid is refined on the breadth to properly represent the boundaries. We choose the level of the quadtree to be $m = 9$. The grid starts with 1044 cells. In addition, we consider $|(w_x)_{j,k}| \geq 0.1$ and $|(w_y)_{j,k}| \geq 0.1$. Figure B.2 (left) shows the computed solution for water surface $w(x, y, t)$ and quadtree grid (right) at $t = 0.5, 1, 1.5$ and 2 for a flat bottom topography.

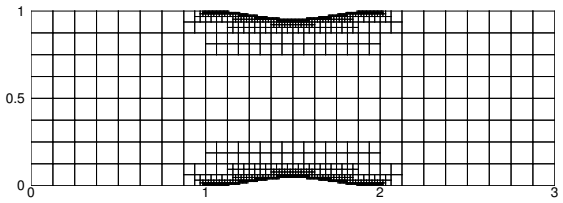

Figure B.1: Example 1: Initial quadtree grid for $m = 9$.

Quadtree grids, and in general, Cartesian grids are not the best grids to solve numerical schemes over domains with curved or complex boundaries; especially when the flow is supercritical. This can lead to some oscillations and spikes near boundaries, which can be seen in Figure B.2.

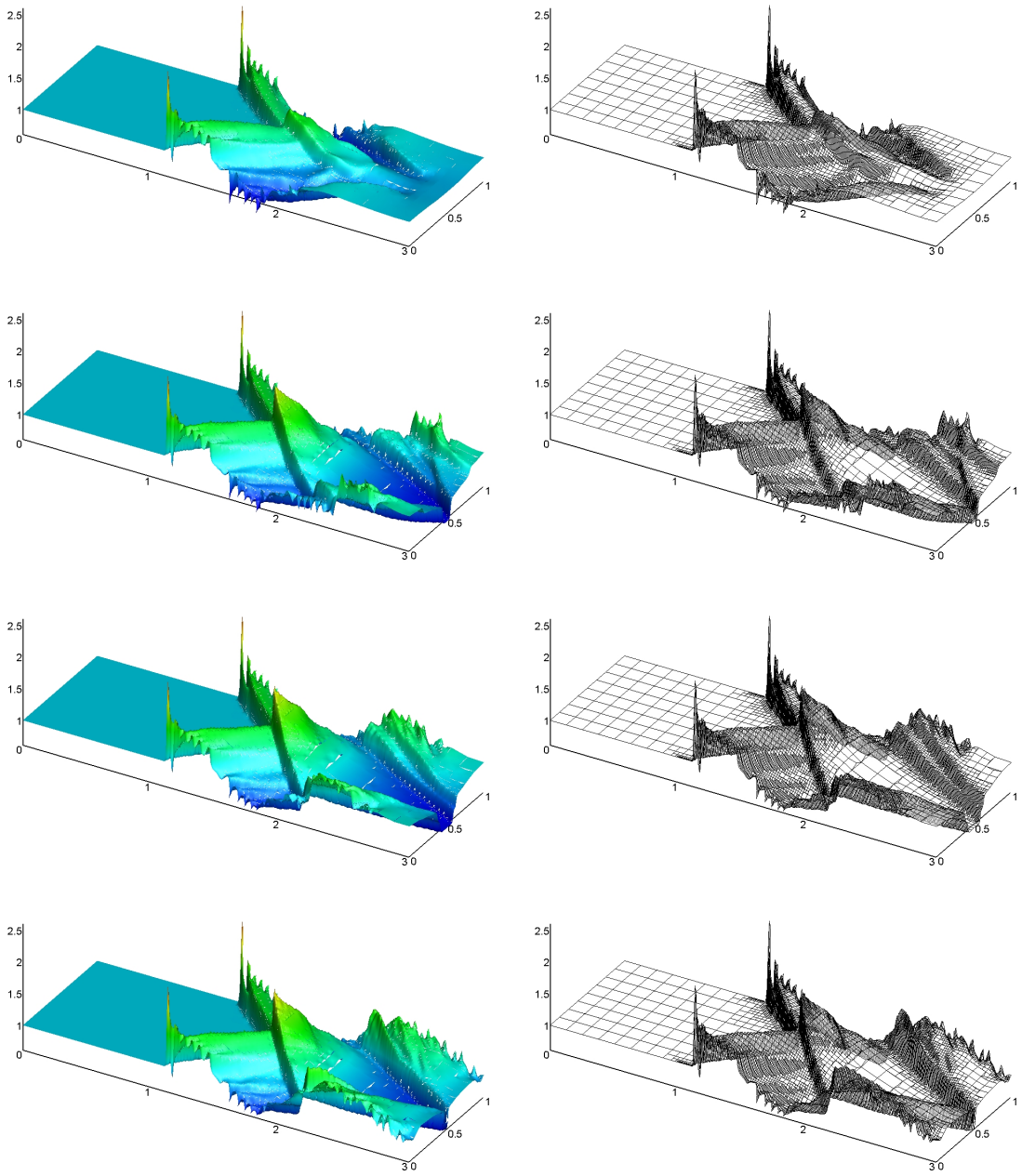

Figure B.2: Example 1: Computed water surface $w(x, y, t)$ for $t = 0.5$, 1, 1.5 and 2 (from top to down) obtained using the flat bottom topography for $m = 9$ (left column) and corresponding quadtree grid (right column).

Example 2. Riemann problem with discontinuous bottom topography

In this example, we demonstrate the capability of the proposed scheme to to solve problems with discontinuous bottom topography. From [9], we consider the following Riemann problem for system (3.1.1)

$$B(x,y) = \begin{cases} 1.1, & x \le 0.5, \\ 1, & x > 0.5, \end{cases} \qquad h(x,y,0) = \begin{cases} 1, & x \le 0.5, \\ 0.8, & x > 0.5, \end{cases}$$

$$u(x,y,0) = \begin{cases} 2, & x \le 0.5, \\ 4, & x > 0.5, \end{cases} \qquad v(x,y,0) \equiv 0.$$

We first, take $g = 9.8$ and obtain the point values of B at the vertices of $C_{j,k}$ using the bottom topography function with $\ell = 6$. A fine Cartesian grid with $m = 11$ is used for the reference solution and solve the Riemann problem with the proposed scheme for $m = 8$ and 9 until $t = 0.03$. Figure B.3 shows the convergence of h and u towards the reference solution, which agrees well with the exact solution from [53].

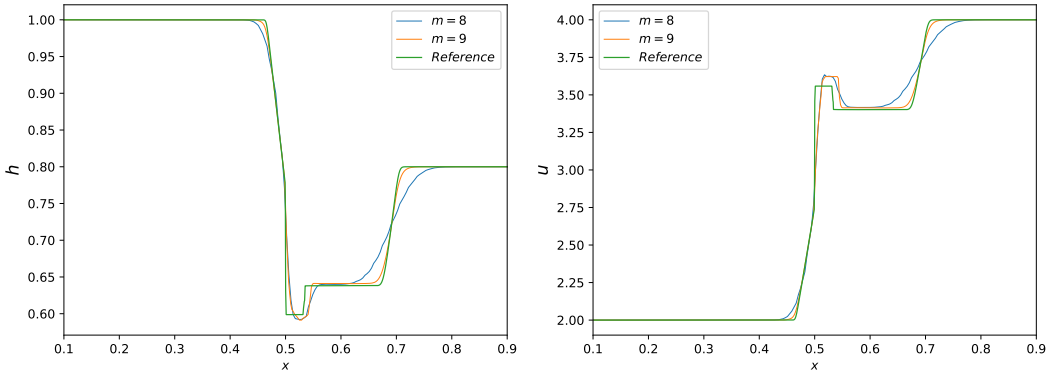

Figure B.3: Example 2: Solution (h on the left and u on the right) computed using $m = 8$ and 9 and compared with the reference solution.

Extra figures for §3.4.3 (Example 3)

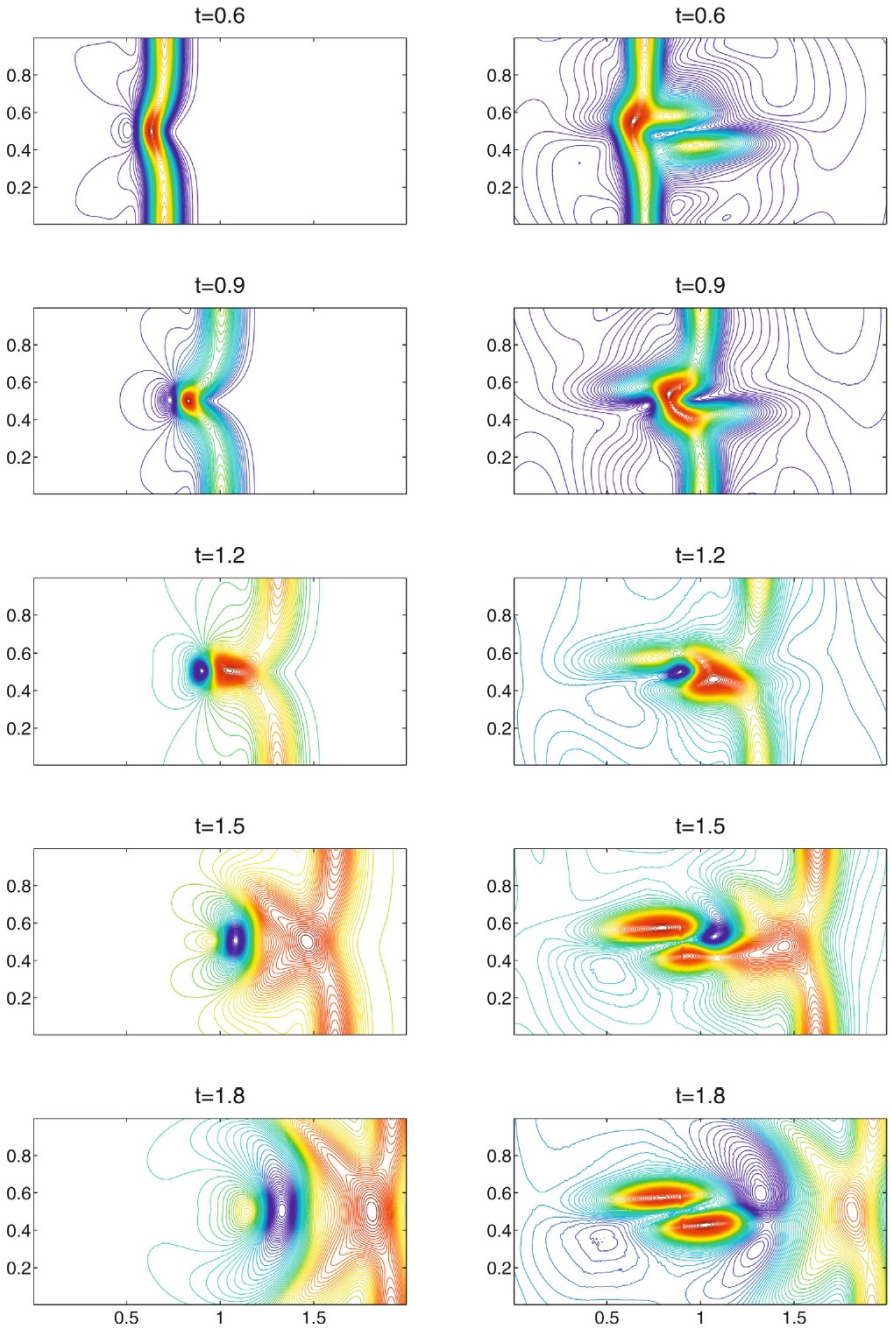

Figure B.4: w component of the solution computed by the well-balanced (left column) and non well-balanced (right column) central-upwind schemes on triangular grid [15].

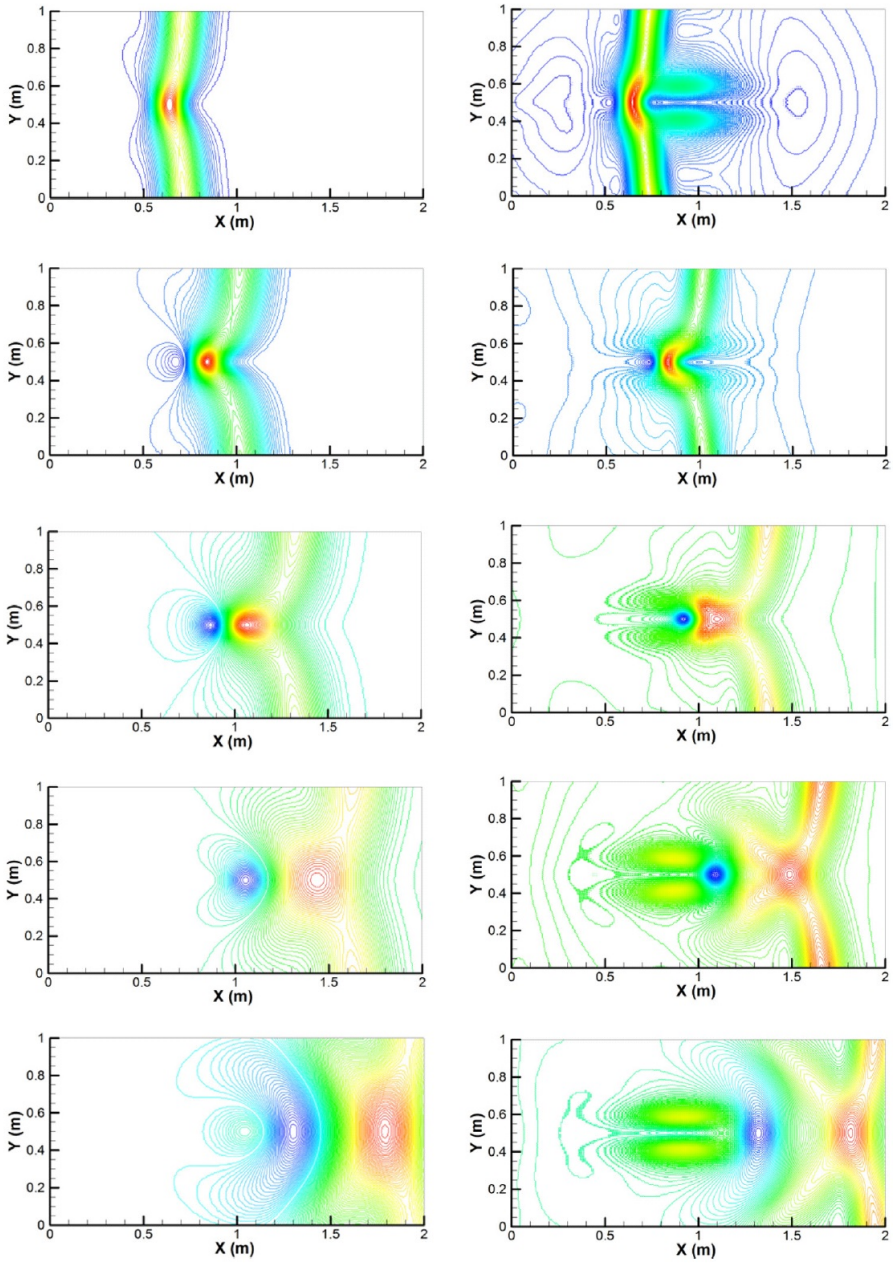

Figure B.5: w component of the solution computed by the well-balanced (left column) and non well-balanced (right column) central-upwind schemes on unstructured quadrilateral grid [85].

Extra figures for §4.4.3 (Example 3)

Figure B.6 shows the density field and the corresponding quadtree grid in 2-D. The initial condition of this benchmark test starts with no velocity. Therefore, the part of the flow with higher density mixes very slowly with the lower density water. It can also be seen from Figure 4.8 that where the flow has higher density it has slightly lower water surface compared to the other parts of the computational domain (this is a similar phenomena that causes a dam break with density discontinuity).

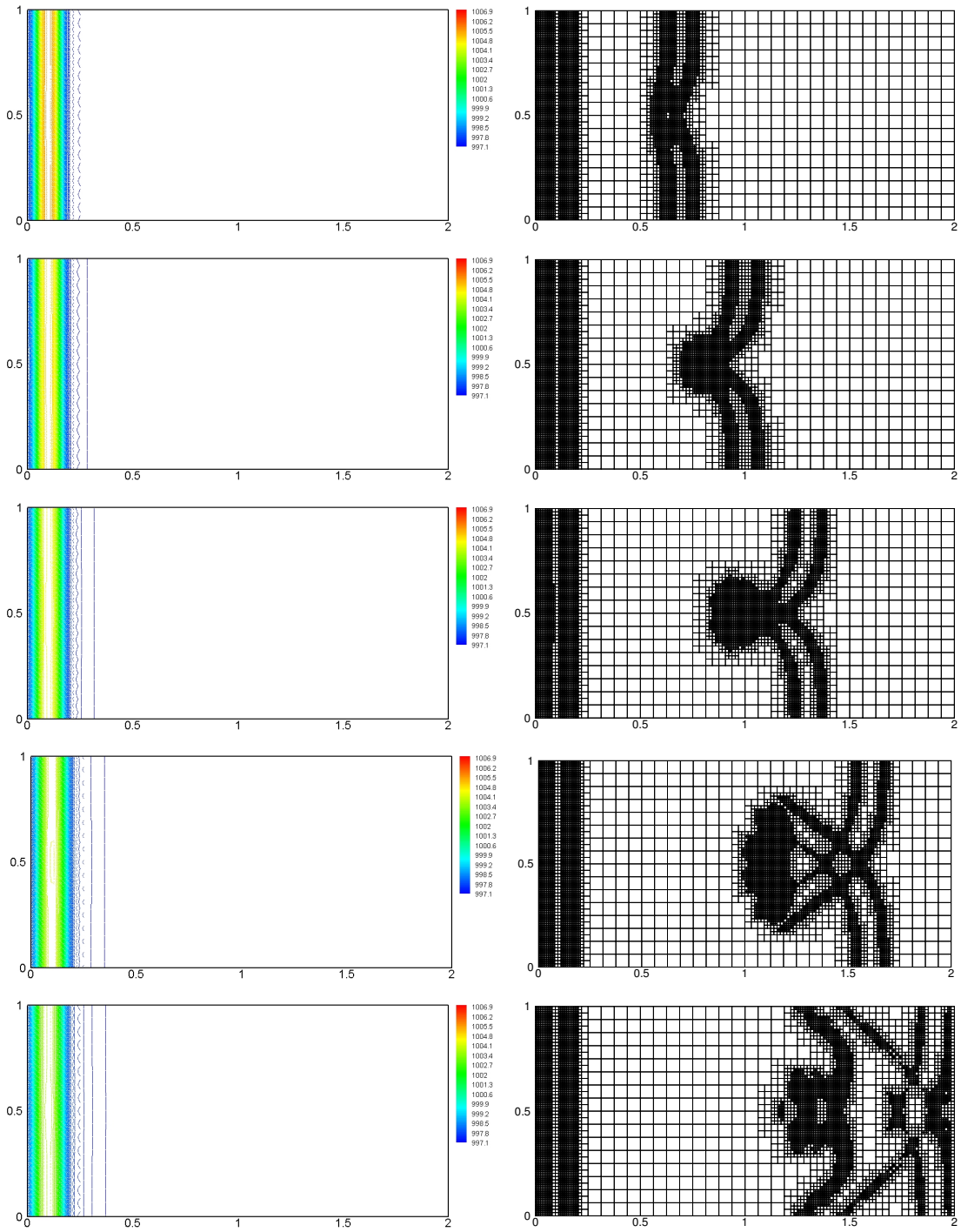

Figure B.6: Example 3: Computed density $\rho(x, y, t)$ (left column) and the corresponding quadtree grids (right column) for $t = 0.6$, 0.9, 1.2, 1.5 and 1.8 (from top to down) obtained using the well-balanced central-upwind quadtree scheme.